Spring 1-1-2013

Modeling Uplift and Fluid Flow in Fractures to Determine the Failure Probability of Concrete Gravity Dams

Erik Jensen
University of Colorado at Boulder, jensen.erik.w@gmail.com

Modeling Uplift and Fluid Flow in Fractures to Determine the Failure Probability of Concrete Gravity Dams

by

Erik Jensen

B.A., University of Massachusetts Amherst

A thesis submitted to the

Faculty of the Graduate School of the

University of Colorado in partial fulfillment

of the requirements for the degree of

Master's of Science

Department of Civil, Environmental, and Architectural Engineering

2013

This thesis entitled:
Modeling Uplift and Fluid Flow in Fractures to Determine the Failure Probability of Concrete Gravity Dams
written by Erik Jensen
has been approved for the Department of Civil, Environmental, and Architectural Engineering

Assoc. Prof. Richard Regueiro

Prof. Bernard Amadei

Prof. Ronald Pak

Date

The final copy of this thesis has been examined by the signatories, and we find that both the content and the form meet acceptable presentation standards of scholarly work in the above mentioned discipline.

Jensen, Erik (M.S. in Geotechnical Engineering and Geomechanics)

Modeling Uplift and Fluid Flow in Fractures to Determine the Failure Probability of Concrete Gravity Dams

Thesis directed by Assoc. Prof. Richard Regueiro

The United States Army Corps of Engineers (USACE) currently operates many large concrete gravity dams that outright fail or narrowly meet design criteria. This is particularly true when elevated reservoir levels cause tensile stresses along a dam's upstream face resulting in cracks along the dam-foundation contact, within the dam or within the dam's foundation. Water pressures are then able to develop within these cracks increasing the uplift pressure on the dam potentially further destabilizing the system. Certain crack locations and orientations can also render drainage systems within the dam ineffective further increasing water pressures. To study the effects of fractures and uplift pressures on concrete gravity dams, a series of finite element models were developed to couple dam and foundation deformations to water flow through a dam, its foundation, or any fractures within the system. The finite element models were verified by providing similar factors of safety to the classical gravity dam design methods. Also, a blueprint for implementing the finite element models inside a probabilistic framework in order to determine a dam's failure probability was outlined. Ultimately, the goal of this research was to provide the USACE an arsenal of tools and analyses to study the stability of their existing concrete gravity dams, while accounting for flow through fractures or jointed rock foundations. These analyses offer engineers methods to study numerous different fracture geometries, material properties, or drain locations while accounting for water flow through the entire dam system.

Dedication

To my fiancé, Jillian, for graciously agreeing to leave behind family, friends, and lifelong home to follow me to Colorado. These last two and half years have been the best of my life, because you've been here with me. Thank you, and I love you.

Acknowledgements

Funding for this research was provided by the U.S. Army Corps of Engineers through contract W912P8-08-D-0002 under the direction of Mr. Gregg Scott. This funding is gratefully acknowledged, and we wish to thank Mr. Scott for helping the research with his technical expertise.

Contents

Chapter

Tables

Table

Figures

Figure

Chapter 1

Introduction

1.1 Problem Description

In the United States, concrete gravity dams are currently designed using guidelines and methodologies most notably outlined in two documents, Design of Small Dams and Gravity Dam Design, published by the Bureau of Reclamation (1987) and U.S. Army Corps of Engineers (1995) respectively. These documents outline a design method based on rigid body statics and mechanics of materials referred to as the gravity or classical design method. Major assumptions of the methodology include all plane sections remain plane and any concrete is impermeable. If flow is allowed through a dam's foundation, pore water causes uplift pressures, which are assumed to be linearly distributed along the base of the dam with the full upstream reservoir head acting at the heel and the downstream reservoir head acting at the toe. For dams that include drainage systems, the head acting at the drain is assumed to be equal to the downstream head plus one-third of the upstream reservoir head minus the downstream head, as specified in Design of Small Dams, or some variant of this equation causing the uplift pressure profile to be a bilinear distribution.

$$h_{drain} = h_{downstream} + \frac{1}{3}(h_{upstream} - h_{downstream}) \tag{1.1}$$

Under certain loading conditions, a designer might calculate a small section of tensile stresses along the dam-foundation contact near the dam's heel caused by large hydrostatic pressures against the upstream face. The concrete in such locations is often assumed to be cracked allowing for water pressures to develop in the fracture. The uplift pressure distribution is considered to be the full

upstream reservoir head, or some large fraction of the full reservoir head depending on the design manual, acting over the entire length of the section.

Although the classical design method is old and relies on a number of simplifying assumptions, the relative infrequency of concrete gravity dam failures and its straightforward implementation makes it an economically attractive option drawing recent arguments for its continued acceptance, such as Watermeyer (2006). However, dam systems with complicated geometries, rock foundations with prominent jointing, fractures that compromise drainage systems, upstream reservoir flood conditions, or other circumstances that violate assumptions made under the classical design method, can force engineers to overdesign dams to account for the uncertainties. The primary goal of this research was to assess the feasibility of using the finite element method and modern computational mechanics software to account for uplift pressures and fluid flow through cracks along the upstream face of a dam, along the dam-foundation contact, or within the dam's foundation with fully coupled solid skeleton deformations and porous media flow through the dam and its foundation. To further account for uncertainties, some of the developed finite element models were implemented inside a Monte Carlo iteration allowing certain parameters, such as the system's permeability or the aperture of a crack, to be varied. By aggregating the results of each iteration, the dam system's failure probability was determined instead of its deterministic factor of safety. Using the methods developed by this project, dam engineers will be able to determine a dam's failure probability while accounting for uplift pressures in fractures and porous media flow in order to more economically design, maintain, and rebuild concrete gravity dams.

The finite element software suite ABAQUS, developed by the Dassault Systèmes Simulia Corporation, was used to develop a series of concrete gravity dam models to verify the feasibility of using the method to account for uplift pressures in fractures and porous media flow in concrete gravity dams. This report describes the development and implementation of the sequence of models. With each successive model, a new, more complicated aspect of a gravity dam system was analyzed. A list of the finite element models analyzed follows.

(1) A two-dimensional concrete gravity dam was set on a rigid foundation with the upstream reservoir pressure and any uplift pressure along the dam-foundation contact applied to the dam as boundary conditions.

(2) The rigid foundation from the first model was replaced with a deformable foundation. Water pressures were applied to the dam and foundation as boundary conditions.

(3) Porous media flow was then allowed through the concrete dam and deformable foundation. Uplift pressures along the dam-foundation contact were allowed to develop from the porous flow and not from an applied traction like in (1) and (2), but the upstream and downstream reservoir pressures were still applied to the dam and foundation as traction boundary conditions.

(4) The dam-foundation contact was replaced with a poromechanical cohesive surface element to model nucleation and propagation of a fracture as well as the development of water pressures in the crack, while allowing for solid skeletal deformations and porous media flow in the dam and foundation.

Results from the finite element modeling were then directly compared to factor of safety calculations using the classical design method in order to verify the numerical models. Also included in this report are the beginnings of a fluid-structure interaction model developed using ABAQUS, coupling the software's computational fluid dynamics capabilities to the aforementioned finite element models, and a discussion on the implementation of a Monte Carlo probabilistic methodology to calculate a gravity dam's failure probability using the discussed models. This research was funded by the United States Army Corps of Engineers and was intended to build on work completed at the University of Colorado Boulder during the late 1980s and early 1990s on the behalf of the Electric Power Research Institute (EPRI).

1.2 Statement of Work

The following section contains the contract's statement of work as well as a brief discussion of the completed tasks and work left to be accomplished.

1.2.1 Original Document

Analysis of Drain Effectiveness and Implications for Failure Probability for Concrete Gravity Dams

Statement of Work

Richard Regueiro (PI), Bernard Amadei (Co-PI), Ronald Pak (Co-PI)

Department of Civil, Environmental, and Architectural Engineering

University of Colorado at Boulder

22 April 2011

Introduction

The U.S. Army Corps of Engineers (USACE) has many large concrete gravity structures associated with dams and related works. Some fail to meet or marginally meet design guidelines. This is particularly true when tensile stress is calculated on the upstream face for elevated reservoir levels and the "cracked base" analysis is invoked where the drains are assumed to be ineffective. While appropriate for new structures, design criteria may not be appropriate for evaluating existing structures. It is important to evaluate actual failure probabilities in a reasonable fashion so that limited resources can be targeted to the structures that pose the largest risk. Therefore, the realistic probability of cracking, the effectiveness of a drainage curtain following cracking, and the limit state after cracking propagates must all be taken into account. The specific goal of this research is to evaluate the probability of failure for concrete gravity dam structures including the effects of potential cracking and drainage.

The main questions we will attempt to answer in this project are:

- What is the most appropriate method to estimate the probability of cracking on the up-

stream face of a concrete gravity dam?

- What are the differences in crack propagation below the dam-foundation contact, at the dam-foundation contact, and above the dam-foundation contact (considering relative permeability between the dam and foundation)?
- What is the best way to include the crack and pore pressures in the calculations?
- What happens if a crack propagates all the way through the section?
- How can the problem be approached in a probabilistic manner?

Professor Bernard Amadei at the University of Colorado, Boulder directed and performed research in the early 1990's evaluating the effects of cracking on the effectiveness of drains in concrete gravity dams. This will be an effort to further develop and implement that research to address more realistically the mechanics and overall probability of instability of concrete gravity dam structures in the presence of drains and cracks under hydraulic conditions. We will incorporate the previous research by Professor Amadei as a starting point to this research project. Professor Amadei will serve primarily an advisory and review role, and Professors Pak and Regueiro will be primarily responsible for achieving the research tasks listed below, in conjunction with one graduate student.

Scope of Work

The work effort will be comprised of the following tasks:

- The first task will be to incorporate previous research results of uplift in cracked, drained concrete dams into a stability analysis, and clarify the role of water pressure in cracks or rock joints at critical locations in the foundation.
- The second task will be to extend the analysis to examine the propagation of cracking and global stability, using classical limit equilibrium approaches and modern nonlinear finite element analysis that accounts for the coupling of pore fluid flow and solid skeleton deformation in the jointed/cracked rock foundation and cracked concrete dam itself. Preferential

flow in cracks with certain aperture within the concrete and rock foundation will be accounted for. The crack apertures can be made a function of the deformation of the solid skeleton of the concrete and foundation rock. Coupled pore fluid flow and solid skeleton deformation of foundation soil will likely be account for in the analysis.

- The third task will be to extend the analysis into a probabilistic framework.
- The final task will be to submit a final report that will document all the results from the tasks above.

Schedule

The tasks noted above will be carried out within a period of twelve (12) months, following receipt of a Notice to Proceed (NTP).

Budget

The funding required to complete the work described here is estimated at $88,405.

1.2.2 Discussion

The following list describes the work completed on each of the four tasks outlined in the scope of work.

(1) Using the reports written for EPRI as a guide, an extensive literature review was developed focusing on the history of uplift pressure models, fracture mechanics as related to seepage in gravity dam systems, and recent developments in modeling cracks and uplift pressures in concrete dams. A full review of the EPRI reports was also completed highlighting the important experimental work, case studies and bevy of programs developed to analyze uplift pressures in gravity dams. The full literature review can be found in Chapter 2.

(2) As discussed in 1.1, a series of incrementally more complex finite element models was developed, and the results of those analyses can be found in Chapters 3 to Chapter 8.

For consistency and simplicity when verifying the results, the models primarily focused on the effects of a crack along the dam-foundation contact, although the analyses could be extended to fractures in jointed rock or the concrete dam. The overall stability of the systems were then assessed by calculating factors of safety using the classical gravity dam design method (Watermeyer, 2006) and resultant forces from the finite element analyses to compare the methodologies. Throughout the series, flow through porous media and preferential flow through cracks were also addressed. Then, analyzing the effects of crack aperture and fracture propagation was begun. More work needs to be completed on the subjects, but thoughts and information on the likely directions of the research can be found in Chapter 8.

(3) Similar to the discussion of crack propagation and aperture dependence, work was started but not completed on implementing the finite element models into a probabilistic framework. An example from EPRI Report 2 (Amadei and Illangasekare, 1990b) was reprogrammed into MatLab to understand the general methodology required for a Monte Carlo iteration, but an iteration around the finite element models was not developed. Further thoughts and discussion on how such a framework would be implemented can be found in Chapter 8.

(4) In addition to this report, a DVD containing all ABAQUS .cae and .inp files, MatLab code, and Microsoft Excel files used during the analysis as well as a document briefly documenting and describing the files and PDF versions of the EPRI reports is attached.

Chapter 2

Literature Review

2.1 Pre-EPRI

2.1.1 History of Uplift Pressure Models and Seepage through Dam Foundations

It was common practice through the early 1900s to not include uplift in the design of gravity dams. Rock was considered impervious preventing seepage under the structure, and it wasn't until some failures were specifically attributed to uplift that engineers began to look at seepage through dam foundations (Riegel et al., 1952). Early work on seepage through foundations composed of soil, gravel or boulders was conducted by Bligh (1910). He believed that the seepage was contained to the dam-foundation contact and could be modeled like flow through a pipe. Through his work, he developed an empirical relationship relating the head difference from the dam heel to toe and a soil fineness or coarseness factor to a percolation distance, the dam width required for overall stability. One major outcome of his work was the assumption that uplift along the dam-foundation contact varies linearly from the full dam head on the upstream face to the head along the downstream face. This assumption has been regularly used in dam design ever since (Bureau of Reclamation, 1987), although Bligh's empirical relationship for flow through a porous dam foundation was replaced by flow nets by the 1940s, most notably through the work of Terzaghi (1929), and more recently by modern finite element methods.

More formal study on uplift under dams founded on rock began in the late 1940s when the American Society of Civil Engineers (ASCE) formed a subcommittee focusing on the problem.

Riegel et al. (1952) analyzed the available literature and came to a series of conclusions. For one, they concluded that unless the dam was floating, uplift pressures would only act along a percentage of the dam foundation varying from 85-100 % of the dam-foundation contact (it should be noted that this recommendation was not unanimous). Also, they were unwilling to make a formal recommendation regarding whether or not the full head at the upstream of the dam should be assumed in the start of the crack at the heel of a dam. Experimental results showed the uplift varied significantly with the geology of the foundation. Lastly, they favored grout curtains as a better method to control uplift over drainage, because drains required regular inspection to insure their optimal operation. This assertion was later challenged by Casagrande (1961), where he determined drains were more effective than grout curtains so long as the drains were installed deep enough to fully penetrate the pervious zone of the foundation. Casagrande's recommendation was later confirmed by Cedergren (1977) and case studies were analyzed by Strassburger (1988) for EPRI.

An analytical solution used to describe uplift pressure in a finite crack along a dam-foundation contact that includes drainage was established by Goodman et al. (1983). The solution assumes laminar and steady flow, constant crack permeability and aperture, and that the crack does not intersect any rock joints or other areas of high permeability (other than drains). They concluded that drains were effective at reducing uplift pressures on the base of the dam, and that it is incorrect to assume that the full reservoir head acts over the entirety of the crack. Their solution found that the head dropped in an approximately linear fashion from the heel of the dam to the line of drains with a slight head increase after to the tip of the crack, which were similar to the results achieved by Casagrande (1961).

As pointed out by the aforementioned ASCE committee (Riegel et al., 1952), one major consideration when modeling seepage through a dam founded on rock is the geology of the area. The topic was first formally discussed by Terzaghi (1929). In his paper, Terzaghi showed a simple theoretical example of how the location of a major joint in a rock mass could significantly change the uplift pressure profile under a gravity dam. Casagrande (1961) conducted a similar thought

experiment concluding that even with the inclusion of drains, the location of major rock joints can significantly change the uplift pressure distribution. Stuart (1963) conducted case studies of gravity dams founded on different types of rock (i.e. fractured sandstone, massive granite, fractured and jointed limestone, etc.) and found that generally uplift pressures were below design levels. However, he also found that where high pressures did exist, the rock was always massive, meaning poorly connected joints preventing drainage of pore pressures. Lastly, Serafim and del Campo (1965) analytically showed that in a crack with an aperture decreasing in the same direction as flow, the head at any point along the crack is greater than a similar crack with constant aperture. These results were experimentally verified by Strassburger (1988).

Research on developing seepage models through jointed rock foundations was first conducted by Casagrande (1961). He initially modeled his work after Brahtz (1936) whose work attempted to model drains in rock foundations. Brahtz assumed that the rock was a semi-infinite porous medium, and Casagrande determined that results from his model did not correlate well with experimental results. Casagrande decided to instead model the foundation as a thin layer of permeable rock at the dam-foundation contact surface underlaid by impermeable rock, and he justified this assumption by arguing that deeper joints would be under higher compressive stresses restricting the flow of water. He also assumed that due to the tensile stresses on the upstream edge of the dam-foundation contact that help open the crack at the heel of the dam, the full reservoir head could be applied at this location in the crack. Using a solution formulated by Muskat (1937), Casagrande developed an analytical solution for the head at any point in the dam-foundation system (including drainage) given the above described assumptions.

Since the work completed by Casagrande, two general classes of seepage through jointed rock models have been developed: (1) network or discrete joint models, and (2) equivalent porous medium models. Essentially, network models assume that flow only occurs through the series of joints in a given rock formation, because the permeability of joints are orders of magnitude greater than the permeability of intact rock. For equivalent porous medium models, jointed rocks are replaced by a medium with a volume averaged permeability.

The majority of network models are based on the assumption that flow through joints can be idealized as flow between two parallel plates (Louis, 1969). Known as the cubic flow law, the relationship states that the volumetric flow rate (q) is related to the hydraulic gradient (i) by the following equation:

$$q = \frac{gb^3}{12\nu} i \tag{2.1}$$

where g is the acceleration due to gravity, b is the constant aperture between the two plates, and ν is the kinematic viscosity of water. This relationship was verified through laboratory experiments with fractures of different apertures and varying wall roughnesses by Louis (1969). Louis also developed two-dimensional graphical and analytical solutions for the uplift pressure distribution on a gravity dam. Discrete joint models were then built into finite element programs in order to analyze more complicated joint networks. Initial work on implementing these models into the finite element method was conducted by Long (1983), Samaniego (1985), Robinson (1984) and Cundall (1983). Notably, Cundall's universal distinct element code (UDEC) is still in use today and is capable of coupling stress and flow through fractured foundations, as shown in Utili et al. (2008).

As previously stated, equivalent porous medium models idealize a jointed rock mass as a medium with an equivalent permeability. Serafim and del Campo (1965), assuming the joints in a rock mass were mutually orthogonal, spaced at regular intervals, and the flow through them was defined by the cubic flow law, derived the principal permeabilities for an equivalent porous medium. This theory was put more generally a few years later by Snow (1969). He derived the two-dimensional equivalent permeability tensor (k_{ij}) for a joint set to be described by the following equation:

$$k_{ij} = \frac{g}{12\nu} \sum_{\alpha} \frac{b^3}{|n_k^{\alpha} D_k^{\alpha}|} (\delta_{ij} - n_i n_j) \tag{2.2}$$

where b is the average constant aperture of the joints, δ_{ij} is the kroneker delta and n_i is the unit normal vector to the joint plane. The equation is summed over multiple sampling lines (α) that

represent boreholes drilled into a rock mass. The more sampling lines considered, the more accurate the equivalent permeability tensor. D_k^α is a vector representing the direction and average spacing of joints along a given sampling line. The absolute value of the inner product between D_k^α and n_k^α is essentially a weighting factor. The smaller the average spacing of joints, the higher the equivalent permeability of the joint set. One major disadvantage to these models was that the joints were assumed to be infinite in length; therefore, the calculated permeability tensors were constant over the medium.

One issue with equivalent porous medium models is whether or not a rock foundation is representative of the larger rock mass. Long (1983) defined the representative elementary volume (REV) as the smallest unit of rock for which the permeability does not vary with the size of the sample tested. He said that an REV must be:

- large enough to be representative of the rock as a whole.
- small enough to be subjected to a uniform hydraulic gradient in the field, because permeability is measured by subjecting a specimen to a uniform hydraulic gradient in a laboratory setting.

In addition to the two types of seepage models previously described, a number of hybrid models have also been developed, many of which have focused on coupling stress and flow. For example, Oda (1986) created a coupled stress/flow model by idealizing a jointed rock foundation as an anisotropic elastic porous medium. Asgian (1988) similarly developed a coupled stress/flow model, but instead of assigning an equivalent porous medium, he allowed individual joints to slip and expand with changes in stress. Shapiro and Andersson (1983) developed a model to couple flow through joints as well as a surrounding porous rock.

2.1.2 Fracture Mechanics as Related to Seepage through a Gravity Dam or Its Foundation

Fracture mechanics is essentially the study of the nucleation and propagation of cracks under different loading and displacement conditions in materials. In regards to assessing the stability of concrete gravity dams, understanding how cracks nucleate and propagate through concrete is an important issue. A number of mathematical models have been proposed to study fractures in various materials, and they fall into two general categories: linear elastic fracture mechanics (LEFM) and non-linear fracture mechanics (NLFM). Both have applications to fractures in concrete structures and will be briefly summarized below.

Kaplan (1961) was the first to apply LEFM principles to describe the behavior of concrete. In his work, he performed 3 and 4 point bending tests on concrete specimens with varying dimensions and crack lengths in an effort to determine the values of concrete's material properties related to LEFM. In LEFM, materials are assumed to be linear, isotropic elastic with no yield stress, resulting in infinite stress at the crack tip. Because this is an unreasonable assumption that results in overly conservative stress estimates, many LEFM models use stress intensity factors to limit the stress concentration at the crack tip. Stress intensity factors can be determined from the linear elastic material properties of a given medium, as described by Irwin (1957). Kaplan's data set was too small to definitively conclude that such materials properties exist, although his work sparked other research in the field. Carpinteri (1982a) found large differences between results even on experiments with concrete specimens of the same geometry and make-up. These discrepancies were attributed to a number of possible explanations including slow crack growth, notch sensitivity, and size effects.

Other researchers decided that these discrepancies showed that LEFM was not applicable to laboratory sized concrete structural components and that NLFM might be more applicable. These researchers defined parameters called characteristic lengths or brittleness numbers as a measure of the effects the size of the specimen, and used these parameters to determine whether LEFM or NLFM could be used to model cracks in the concrete (Carpinteri, 1982b) (Hillerborg, 1983)

(Bazant, 1984). At the tip of a crack, materials exhibit a zone of nonlinearity, and for concrete, this zone can be large when compared to the size of the specimen. When the zone of nonlinearity, also known as the fracture process zone (FPZ), is large, LEFM will overestimate the stresses at the crack tip suggesting that NLFM models should be implemented instead (Bazant, 1984).

One of the first NLFM models developed was called the fictitious crack model (FCM) (Hillerborg et al., 1976), which described mode I fractures (fractures caused by stresses normal to the propagation direction) in the FPZ. In the FCM, the strength of the concrete is modeled by a softening constitutive relationship, where the initial strength of the concrete is the uniaxial tensile strength and the final strength is zero at what is known as a critical crack width. In between no crack and the critical crack width is the FPZ, where the strength of concrete degrades from the initial strength to zero. The shape of the softening relationship theoretically depends on the post peak response of a uniaxial tension test (Hillerborg, 1983), but due to the difficulty in obtaining such information, has been modeled using a variety of different functions (although these functions are usually assumed linear or bilinear).

Both LEFM and NLFM have been applied to concrete dam applications, although LEFM has been more widely used. Cracks are generally assumed to occur and propagate along the dam-foundation contact, because the strength of the concrete and rock connection is likely weaker than the tensile strength of rock or concrete. Along with cracks, joints in the rock foundation could also be modeled, especially if a joint might cause a deviation of the crack from the dam-foundation contact. With regards to non-linear fracture mechanics in concrete, smeared crack and discrete crack models, two finite element implementations of the fictitious crack model, are widely used (Saouma et al., 1989). As mentioned in the previous section, special care must be taken when dealing with concrete dams, because of the uplift pressure exerted on these potential cracks.

2.2 EPRI Reports

The following subsections summarize the work performed at the University of Colorado Boulder for the Electric Power Research Institute (EPRI) during the late 1980s and early 1990s. The

final submittal for the project contained an eight volume report (Amadei and Illangasekare (1990a), Amadei and Illangasekare (1990b), Illangasekare et al. (1990), Chinnaswamy et al. (1990), Amadei et al. (1990), Grenoble et al. (1990), Amadei (1990), and Amadei and Illangasekare (1990c)) and users manuals documenting two finite element programs that were developed (Grenoble et al. (1988) and Reich (1993)).

2.2.1 Volume 1: An Analytical Solution for Uplift in Cracks in Concrete Dams: Programs WELL, UPLIFT & WELLD

Volume 1 of the EPRI reports continues on work conducted by Goodman et al. (1983) in which the authors presented an analytical solution for the uplift in a crack along a dam-foundation contact. This report generalizes the solution to include cracks within the dam itself, while keeping the other original assumptions intact (i.e. steady, laminar flow, and constant crack permeability and aperture). Also, the report provides information regarding to three computer programs that implement the analytical solution: WELL, UPLIFT, and WELLD. WELL and WELLD similarly calculate head, velocity, and Reynold's number distributions within the crack as well as calculate uplift force, overturning moments, drain effectiveness and the location of the center of pressure. WELLD, however, takes into account head losses in the drain pipes. The program UPLIFT calculates uplift force and moments for varying drain locations and can be used to optimize drainage given the dimensions of a crack. The report provides users manuals for all three programs that were developed.

2.2.2 Volume 2: Uplift Pressures in Cracks in Dams; A Probabilistic Approach Using Monte Carlo Simulation Program MCWELL

This report outlines the implementation of the Monte Carlo simulation method on an analytical solution for uplift pressure in a crack with drains prepared by Amadei et al. (1989). The program MCWELL allows users to input probability density functions (PDF) for otherwise deterministic variables (crack aperture, roughness, length, etc.) and then outputs PDFs and cumulative

density functions (CDF) for the uplift force and overturning moments. This allows engineers to develop a safety margin (a comparison of the total resisting force to the uplift PDF) as opposed to a traditional deterministic factor of safety, providing more information from which to base decisions.

2.2.3 Volume 3: A Model to Estimate Uplift in a Crack with a Box Drain: Users Manual for Program INTRA1

INTRA1 is a program similar to WELL, UPLIFT, and WELLD in that it calculates the uplift pressure distribution along a crack in a dam. However, the program implements an integral transform technique to solve the flow equation for a crack intersected by a box drain. This formulation is the basis for the more general finite element model CRFLOOD.

2.2.4 CRFLOW: Finite Element Seepage Analysis for flow Through a Crack in a Concrete Dam

Version 1.0 of CRFLOW is a finite element program designed to model flow of water through a crack in a concrete dam. It was developed because of the limitations of the analytical solutions proposed by Goodman et al. (1983). It models seepage through an arbitrary crack, provided its plane is horizontal, accounting for prescribed head and flow boundary conditions. It assumes that flow through the crack is steady and laminar, Darcy's law is valid, and the hydraulic conductivity within each crack element is isotropic and constant (i.e. doesn't vary with pressure and the crack does not deform). Flow through the crack is assumed to be governed by a variant of the cubic flow law (2.1) where the aperture term is replaced by a smaller effective aperture to account for the deviations within the crack from the two parallel plates assumption used to derive the law. This modified flow law was proposed by Long (1983). Also, the program allows for the inclusion of drainage by fixing either the head or flow rate at nodes containing drain pipes. Once provided with the input parameters, CRFLOW calculates the total head and water pressure at each node; the Reynold's number, water velocity, uplift force, and overturning moment at each element's centroid; and the total uplift force and overturning moment of the structure. The program was found to be

in agreement with the aforementioned analytical solutions providing it verification.

2.2.5 Volume 4: CRFLOOD: A Numerical Model to Estimate Uplift in Cracks in Gravity Dams

CRFLOOD is a descendant of CRFLOW designed to handle laminar and turbulent as well as steady-state and transient flow conditions; CRFLOW could only handle laminar and steady-state flow. Also, CRFLOOD has the capability to accurately model the geometry of a drain-crack connection, whereas CRFLOW idealized this geometry as only a prescribed nodal head or flow rate value. The program was validated by a series of laboratory experiments that showed good agreement between actual and numerical uplift results. The report then describes a parametric study conducted with CRFLOOD to determine significant parameters affecting uplift pressure distributions within a given crack and the effectiveness of drainage within a dam. It was found that drain effectiveness increases with drain diameter (to a certain limit), the optimal drain location is a balance between high head gradients (causing turbulent flow that lowers the transmissivity of the crack) when the drain is placed near the upstream edge and higher total uplift force when the drain is placed near the downstream edge, closer drain spacing results in higher drain effectiveness, and increasing the upstream reservoir head to model a flood event could result in a transition from laminar to turbulent flow reducing drain effectiveness.

2.2.6 Volume 5: Uplift in Cracks in Concrete Dams: Field Study

The primary goal of this study was to develop a methodology for calibrating the finite element program CRFLOW by measuring or estimating input parameter values from dam case studies. It is difficult to determine these parameters, because access to a crack for measurement is nearly impossible and often limited to a single borehole. Assumptions must be made regarding the crack geometry, boundary conditions, and how to model the flow (i.e. the revised cubic flow law). The report outlines equipment, test procedure, and calibration technique used to create an accurate model of a crack in a specific dam. It was found that CRFLOW could accurately replicate the

experimental findings, although due to the difficulties in determining the input parameters, much intuition was required to generate such a model.

2.2.7 Volume 6: Influence of Rock Discontinuities on Seepage and Uplift in Concrete Gravity Dam Foundations: A Numerical Approach

This report summarizes the development of a finite element program used to model uplift on gravity dams founded on jointed rock. The program generates a joint network based on joint set characteristics gathered for a given foundation rock. This network is then input into the two-dimensional finite element program JOINTFLO, developed by Grenoble (1989), that models seepage through the joints and calculates water pressure at each intersection as well as the velocity of the water in the network. The program was validated through a series of comparisons to analytical solutions and a laboratory experiment and then used to complete a sensitivity study to determine the effect of various parameters on the uplift distribution. It should be noted that no attempt was made to couple stress and flow. Major findings of the study include: the assumptions generally made regarding uplift pressure distributions (Bureau of Reclamation, 1987) are generally good, some rock joint locations do produce much larger and much smaller uplift pressure distributions, large faults near the base of the dam (not necessarily in contact with the base, however) can significantly increase the uplift force, the uplift force increases as a drain is moved further downstream (in general), and deeper drains are more effective at reducing uplift pressures.

2.2.8 Volume 7: Three Dimensional Modeling of Dams with Cracks Using the Boundary Element Method: Programs BEDAM & BEDAMC

This report provides information on two three-dimensional boundary element programs, BEDAM and BEDAMC, used to predict the deformations of cracked concrete dams. These boundary element programs were used to model monolithic concrete gravity dams and cracks in the system were modeled using CRFLOOD. Using uplift pressure information obtained from CRFLOOD, uplift tractions were applied to the three-dimensional concrete dam models and used to determine

their deformations, effectively creating one coupled hydromechanical model. The boundary element method was used for computational efficiency, although has the disadvantage that it required the concrete to be modeled as a linear elastic, isotropic, and homogeneous material. BEDAM analyzes the stability of a dam on a rigid foundation with a simple quadrilateral crack along the dam-foundation contact. BEDAMC analyzes the stability of a dam containing two different media with different elastic properties split by a crack (i.e., a crack within a dam or at a concrete-rock interface along the dam-foundation contact). A number of examples were provided within the report describing the usefulness of conducting a three-dimensional, boundary element method dam stability analysis.

2.2.9 Volume 8: Uplift Pressures in Cracks in Concrete Gravity Dams: Experimental Study

Flow through cracks is often idealized to follow the cubic flow law for flow between two smooth, parallel plates. Obviously, actual cracks in concrete or along joints in rock do not necessary fit the required assumptions. As a result, numerous empirical corrections have been applied to the cubic flow law to more accurately model flow through cracks and joints. This report presents the results of experiments designed to characterize and test the applicability of the existing empirical corrections to flow through concrete cracks.

2.2.10 On the Marriage of Fracture Mechanics and Mixed Finite Element Methods: An Application to Concrete Dams

This thesis documents the creation of the finite element program MERLIN, developed by Reich (1993), that models the propagation of cracks using linear and nonlinear fracture mechanics including the addition of simple uplift models, steady-state and transient heat transfer, and steady-state and transient seepage. It focuses heavily on the mathematical formulation and finite element implementation of these models.

2.3 Post-EPRI

2.3.1 Current Gravity Dam Design and Stability Analysis Methods

Modern concrete gravity dam designs and stability analyses are generally conducted using traditional methods derived from rigid body statics called classical or gravity methods depending on the source. These methods are outlined in full detail in a number of documents, but most notably Design of Small Dams by the Bureau of Reclamation (1987), Gravity Dam Design by the U.S. Army Corps of Engineers (1994), and a design manual written by Federal Energy Regulatory Commission (2002). In these documents, plane sections are assumed to remain plane and concrete is assumed to be impermeable. Gravity dams work by using their self-weight to resist the other forces attempting to cause sliding or over-turning, such as the normal force of the foundation pushing upwards and the pressure from the upstream reservoir acting horizontally on the dam face. As for specifications relating to the force due to uplift pressure acting on the dam-foundation contact, all offer a variation on the assumption that uplift is a linear pressure distribution and acts as an external stress. In Design of Small Dams, the uplift is assumed to be equal to the full upstream reservoir head at the heel of the dam and the full tailwater head at the toe of the dam, varying linearly between these two values and acting on the full area of the dam-foundation contact. If the dam includes drains, the pressure acting at the line of drains is assumed to be the tailwater pressure plus one-third the differential between tailwater and headwater pressures creating a bi-linear pressure distribution. Also, if the dam has or is assumed to have a crack (which is often assumed in the tension region along the dam-foundation contact), the full upstream reservoir head is assumed to act along the entire length of the crack. The classical method continues to be the simplest and most widely used gravity dam design and stability analysis tool and continues to draw arguments for its acceptance, such as Watermeyer (2006).

Gravity design methods typically employ factor of safety driven stability analyses. A factor of safety is defined as the ratio of the forces or moments resisting failure to the forces or moments causing failure. Factors of safety greater than 1.0 signify a stable system where the resisting forces

are greater than the forces causing failure, while factors of safety less than or equal to 1.0 describe an unstable system. The primary modes of failure for gravity dams are overturning and sliding.

2.3.1.1 Factor of Safety Against Sliding

In the classical gravity dam design method, factors of safety against sliding are defined by (2.3), or some variant of (2.3) accounting for unusual loading conditions, other sliding reinforcement, or other easily accountable situations.

$$FS_{sliding} = \frac{CA_b + W\tan(\phi)}{P} \tag{2.3}$$

Equation (2.3) is a variant of a Mohr-Coulomb failure envelope where $FS_{sliding}$ is the factor of safety against sliding, C is any cohesion between the dam and foundation (kPa), A_b is the area of the dam base in contact with the foundation (m^2), W is the downward vertical force acting on the foundation primarily caused by the self weight of dam (kN), ϕ is the internal angle of friction at the interface of the foundation material, and P is the total horizontal (shear) force pushing the dam downstream (kN). The downward forces and cohesion both work to prevent the dam from sliding acting against the horizontal forces primarily caused by hydrostatic upstream reservoir pressures. With the addition of uplift pressures acting along the base of a dam, the total vertical force (W) is reduced by the total uplift force (U) resulting in an effective vertical force (T) (Equation (2.4)) decreasing the overall factor of safety against sliding (Equation (2.5)).

$$T = W - U \tag{2.4}$$

$$FS'_{sliding} = \frac{C'A_b + T\tan(\phi')}{P} \tag{2.5}$$

C' and ϕ' are the effective cohesion and friction angle, respectively (Watermeyer, 2006).

2.3.1.2 Factor of Safety Against Overturning

The factor of safety against overturning is calculated as the ratio of the moments about the dam toe acting to overturn a dam to the moments resisting overturning. Overturning moments are caused by, but not limited to, the force of the reservoir acting on the upstream face of a dam (P) and the total uplift force acting on the base of a dam (U). As is implied by the name, overturning in concrete gravity dams is primarily resisted by the self weight of the concrete (W). All three forces are then multiplied by their respective moment arms about the toe of the dam (E_p, E_u, and E_w), and input into Equation (2.6) to calculated the factor of safety against overturning (Watermeyer, 2006).

$$FS_{overturning} = \frac{WE_w}{UE_u + PE_p} \tag{2.6}$$

2.3.2 Developments in Modeling Cracks and Uplift Pressures in Concrete Gravity Dams

Since the early 1990s, work related to modeling cracks and uplift pressures in concrete gravity dams has focused on three main topics: researching the effect of uplift pressures on cracks including how to represent uplift in finite element models, describing the origin of cracks in concrete, and creating newer and more elaborate numerical models of gravity dams. The following section will outline the work done in each of these three sections.

2.3.2.1 Uplift Pressure on Cracks in Concrete Gravity Dams

Dewey et al. (1994) published a paper reviewing classical and finite element uplift pressure models on a crack at the dam/foundation contact of a concrete gravity dam. They implemented a series of finite element models that applied uplift pressure along just the crack, along the entire base using the pressure distribution assumptions of the classical method described in the previous section, and along just the crack but including the uplift pressure distribution caused from seepage under the dam (assuming the foundation was pervious). To compare these different models, they

used the finite element code MERLIN implementing a LEFM model to calculate the stress intensity factor at the tip of the crack. It was discovered that the stress intensity factor was sensitive to the uplift model chosen, and it was the authors' conclusion that the seepage model provided the most "satisfactory" results.

Experimental work by Bruhwiler and Saouma (1995) determined that the uplift pressure distribution should not be assumed to be the full reservoir head over the entire length of a crack. Instead, they discovered that the distribution is constant at the full reservoir head until the crack reaches what they called a critical crack opening. At this aperture, the uplift begins to decrease reaching zero at the crack tip. Plizzari (1998) took this information and developed a methodology to empirically estimate the shape of the uplift pressure distribution in cracks in concrete dams (primarily not along the dam-foundation contact). He used these formulae and the finite element code MERLIN implementing a LEFM model to conduct a parametric study to determine the influence of uplift pressure profiles on the stress intensity factors, like the work by Dewey et al. (1994), and the crack propagation angle. He also found that these parameters are highly sensitive to changes in the uplift pressure profile.

More recent work on modeling uplift pressures has returned to studying uplift on the base of a gravity dam due to seepage through jointed rock foundations. More specifically, research has focused on the creation of three-dimensional coupled stress/flow models. Al-Obaydi et al. (2008) developed such a model by using an equivalent porous media approach where the permeability matrix is defined by the flow through joints sets assuming the validity of the cubic flow law (2.1). They used empirical relationships to couple stress to joint aperture deformations causing changes in the permeability of the foundation, and were able to successfully model the uplift pressure distributions on a gravity dam.

Other recent work in this field has focused on uplift pressures in cracks under dynamic loading. An example of such research was conducted by Slowik and Saouma (2000). They conducted a number of experiments aimed to determine how water flows through cracks under sudden changes in crack aperture in order to propose a flow model that could be implemented in a finite element

framework. They found that the faster a crack opens, the lower the water pressure distribution. In other words, the crack opens faster than the water can flow in not allowing hydrostatic conditions to be obtained. Using this information, they proposed a flow model that could be coupled with NLFM crack propagation models under fast loading conditions.

2.3.2.2 Origins of Cracks in Concrete

Widmann (1990) pointed out that "fracture mechanics exclusively deals with problems relating to crack propagation and such safety against cracking, so that the term 'crack mechanics' would be more appropriate. Neither crack origin nor complete failure of the structure, i.e., its stability, resort to this special field." In other words, the fracture mechanics models that had been developed required input parameters describing the initial crack geometry without addressing why the crack exists. In his paper, he outlines some possible explanations for why concrete gravity dams (as well as other types dams) might have cracks and offers thoughts on the implications of these explanations on selecting the required parameters for further analysis. Some of the reasons included thermally induced deformations either during the initial curing of the concrete or throughout the dam's life, deformations caused by swelling or creep, and deformations caused by changes in abutment geometry. He also stressed the importance of understanding concrete dams as complex three-dimensional and highly indeterminate systems.

One example of research aimed at solving the problem outlined by Widmann (1990) was conducted by Li (1995). In his paper, he describes an application of viscoplastic damage theory to determine the location of cracking sites in a concrete gravity dam. His paper primarily focuses on discussions of the mathematical formulation and finite element implementation of the model, although two numerical models are presented. In one of the numerical models, Li shows the progression of fracture sites with increased load in a theoretical gravity dam that appears reasonable given the assumptions about the material properties of concrete (homogeneous and isotropic elasticity).

2.3.2.3 Numerical Models of Fracture Mechanics in Gravity Dams

One notable debate regarding applications of fracture mechanics to concrete gravity dams has been the applicability of LEFM models to concrete. Studies such as the ones conducted by Dewey et al. (1994) and Plizzari (1998) have concluded that the relative size of the fracture process zone compared to the concrete dam allows the use of LEFM. Others, such as Bhattacharjee and Leger (1994), disagreed with the assertion, especially in the neck of a dam, and concluded that NLFM methods could provide important softening effects in the fracture process zone without additional computational expense. As a result, Bhattacharjee and Leger (1994) focused their work on analyzing the effectiveness of two NLFM models: the coaxial rotating crack model (CRCM) and the fixed crack model with a variable shear resistance factor (FCM-VSRF). In their paper, the models were applied to three examples that had been previously investigated both experimentally and using LEFM models. They were able to verify the above assertion as well as conclude that CRCM produced more consistent and accurate results than FCM-VSRF, and that NLFM models had low computational costs and required simple material properties.

Another major development in the study of jointed rock with the finite element method has been the formulation of cohesive surface elements. As discussed in Section 2.1.1, flow through jointed rock was traditionally handled with either network flow or equivalent porous media models. But recently, interface elements, like cohesive surface elements, have been developed to handle the nucleation and propagation of cracks as well as fluid flow within a crack. Many formulations have been proposed, but Segura and Carol (2004) developed a poromechanical cohesive surface element that could conserve both longitudinal and transverse flow and be easily implemented in pre-existing finite element meshes, by virtue of using only pre-existing nodes. The authors later extended their work (Segura and Carol (2008a) and Segura and Carol (2008b)) to include the influence of displacements within the cohesive surface element creating a fully coupled hydro-mechanical model. Also, work was completed by Yu (2010) extending a cohesive surface element's mechanical constitutive model to include pressure sensitive rigid and elasto-plasticity, allowing for

more complicated hardening or softening behaviors to develop. Concurrent work at the University of Colorado at Boulder (Sweetser, 2012) further extended Yu's work to include porous media flow in the elements.

Shi et al. (2003) developed a methodology for including multiple cracks in a concrete gravity dam instead of only one like previous models. The major issue behind creating such a methodology is determining which of the cracks will propagate. Shi et al. (2003) determined that one possible algorithm to achieve this goal is to assume that all cracks propagate independently by restricting the growth of all but one crack at a time, determine which crack required the least energy to propagate, and then update the geometry with only that crack growing. Repeating this process will allow for multiple cracks to develop if the stress states in the concrete structure dictate this type of fracture. They validated their findings against a number of experimental results, including a large scale gravity dam model, with good overall agreement.

Similar to the discussion on uplift pressures in cracks, much of the numerical modeling of fracture mechanics in gravity dams has been focused on modeling behavior under dynamic loading. For example, Mirzabozorg and Ghaemian (2005) developed a three-dimensional smeared crack model (NLFM) assuming a simple strain softening constitutive relationship in tension and linear elasticity in compression for concrete. The concrete was also assumed to be homogeneous such that the model required only a few basic material properties. They found good agreement between their model and experimental data gathered for seismic event case studies of two concrete gravity dams.

Chapter 3

Gravity Dam with a Rigid Foundation Model

3.1 Gravity Dam Model Geometry, Loading and Material Properties

To illustrate a typical classical gravity dam design method factor of safety analysis and to provide a comparison to the finite element modeling, an example dam from Watermeyer (2006) was analyzed. The total vertical and horizontal stress distribution along the base of the example dam and the factors of safety against sliding and overturning were calculated given three different uplift pressure distributions and for varying internal friction angles. The three uplift pressure distributions were as follows:

(1) No uplift pressure applied to the base of the dam.

(2) The classically assumed linear distribution from full upstream reservoir head at the heel to downstream reservoir head at the toe.

(3) The classically assumed linear distribution including a drain located approximately two-thirds from the heel along the dam-foundation contact. The distribution of uplift pressure was assumed to vary from the total upstream reservoir head at the heel to the downstream reservoir head at the drain and toe, which is a variant on the aforementioned uplift distribution with drainage (see Section 2.3.1).

Diagrams of the three uplift pressure distributions can also be found on Figure 3.2. An example from Watermeyer (2006) was selected because vertical stress distributions were included in his paper providing a direct comparison to verify some of the calculations herein presented.

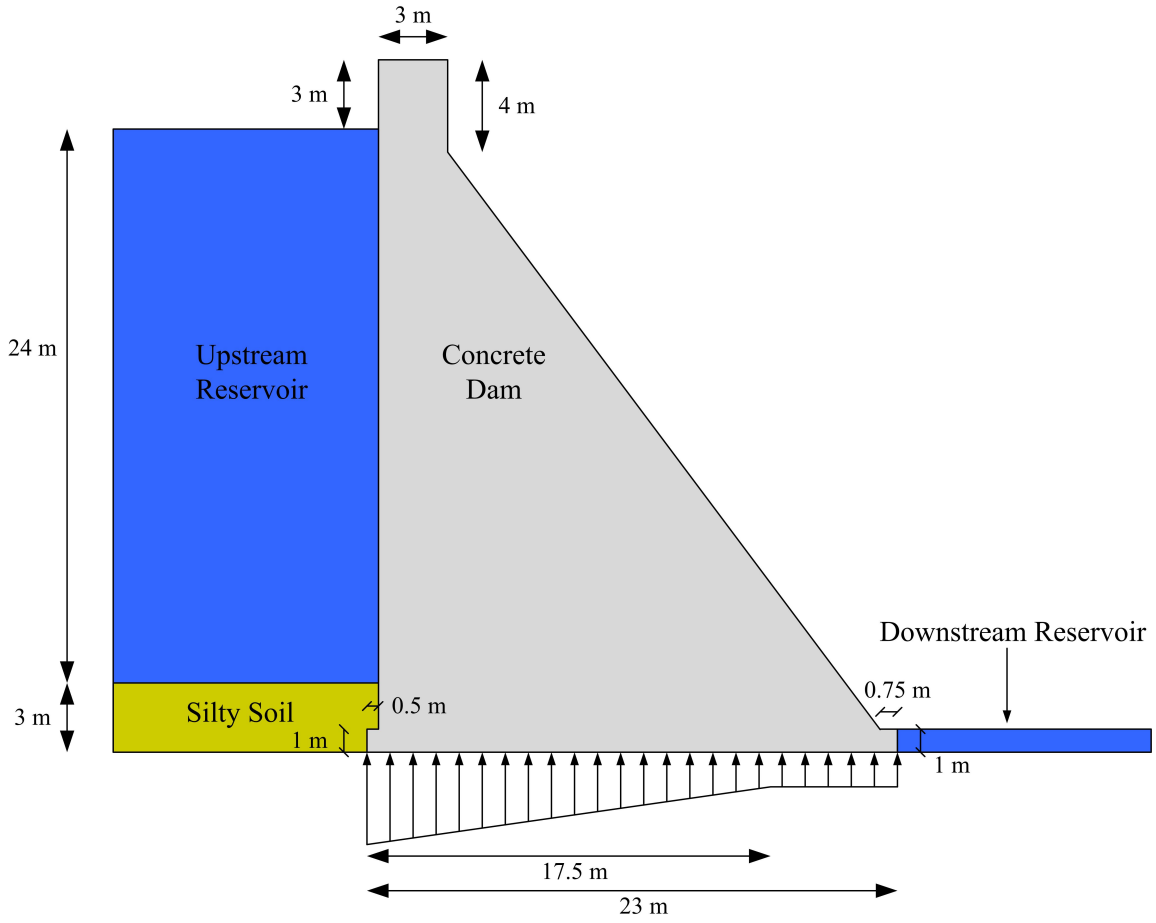

Figure 3.1: Geometry of the Example Dam from Watermeyer (2006)

Figure 3.1 contains the geometry of the example dam including the upstream and downstream water levels and the third described uplift pressure distribution. Also included in this example is a small layer of silty soil burying the heel of the dam, causing a small lateral geostatic load on the dam's upstream face. The unit weight of the concrete dam was assumed to be 23.5 kN/m^3. The silty soil's buoyant unit weight was assumed to be 10.0 kN/m^3, and the cohesion between the dam and foundation was set to zero.

3.2 Finite Element Model Development in ABAQUS

Using the same geometry and material properties from an example dam in Watermeyer (2006) described in Section 3.1, a finite element model was created in ABAQUS/Standard using

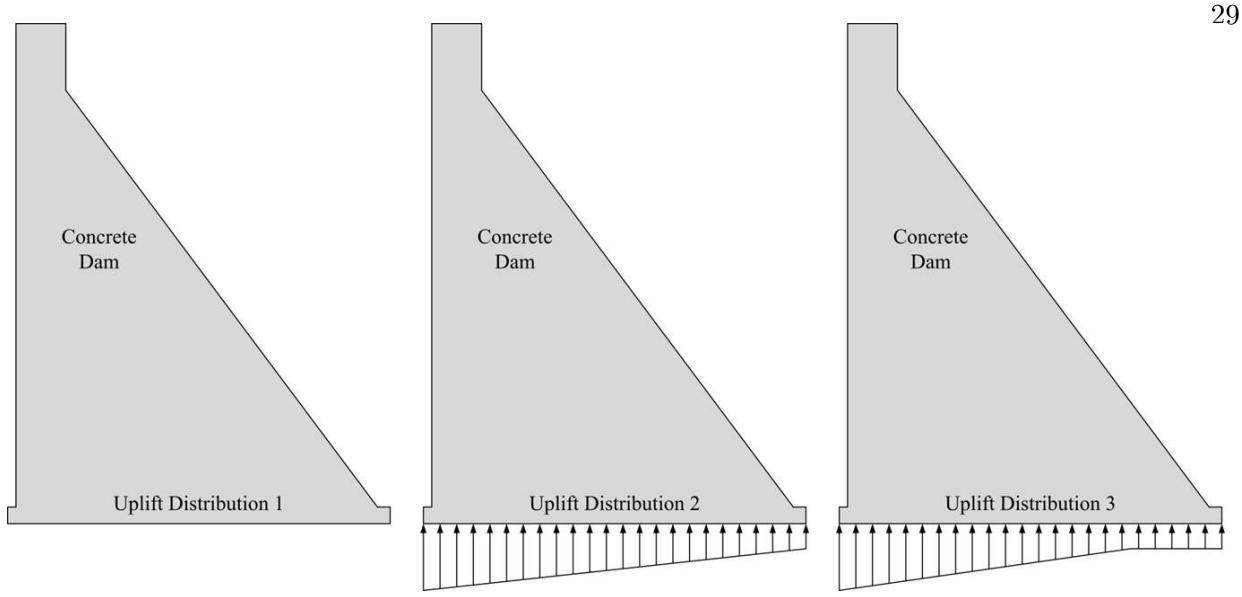

Figure 3.2: Geometry of the Example Dam Including the Three Uplift Pressure Distributions

the ABAQUS/CAE interface. In addition to the aforementioned material properties, it was assumed that the concrete dam is a linearly elastic and isotropic deformable solid with a Young's modulus of elasticity of 20.67 GPa and a Poisson's ratio of 0.2. The non-deformable foundation was modeled by implementing a discrete rigid line completely fixed in space. The contact between the dam and rigid foundation was achieved by using a surface-to-surface contact model built into ABAQUS/Standard where the tangential behavior was described by a coefficient of static friction and the normal behavior was considered unbonded – i.e., the zero cohesion condition. The coefficient of static friction was taken to be the tangent of the friction angle, which is the factor multiplied by the vertical force T used in the factor of safety analysis. Boundary conditions describing the hydrostatic upstream and downstream reservoir pressures and the geostatic pressures from the deposited silty soil layer were applied to the concrete dam, and a gravity load was applied to the entire model. In ABAQUS/Standard, the acceleration due to gravity is multiplied by the mass density of the materials in the model to produce unit weights that are then used to determine stresses due to the self weight of the model. The three different uplift pressure distributions were applied to the concrete dam as pressure boundary conditions applied directly to the base of the dam. No fixed

displacement or rotation boundary conditions were applied to the dam; only the frictional contact between the dam and rigid foundation was able to resist horizontal displacements. The full model as rendered by ABAQUS/CAE can be seen on Figure 3.3.

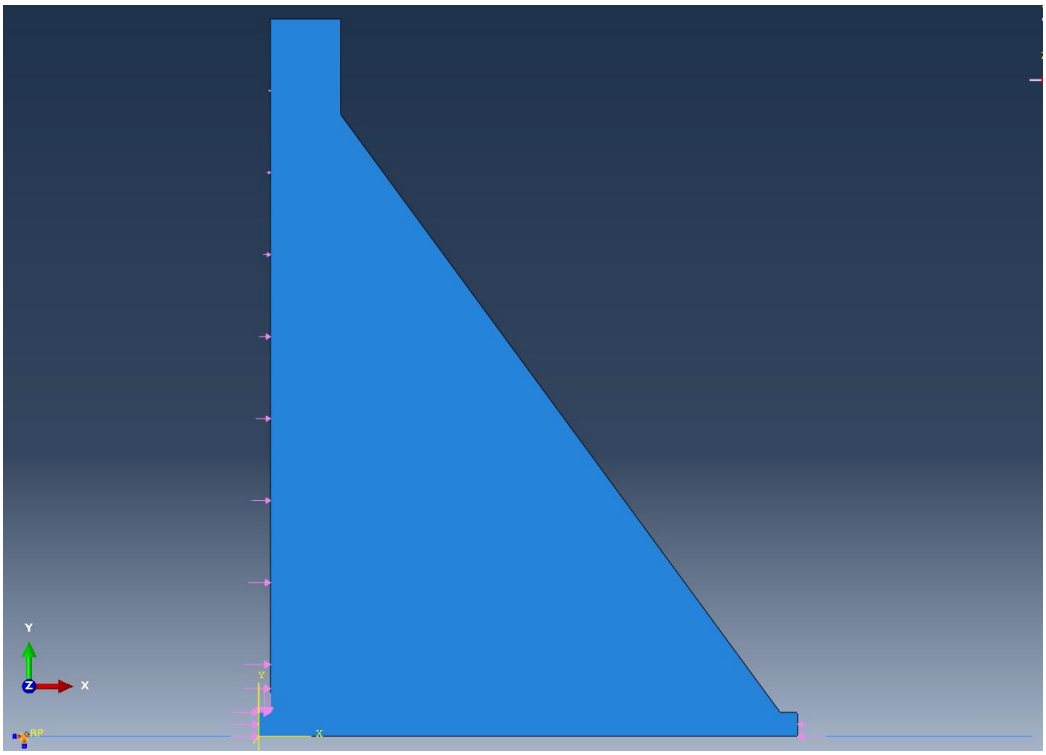

Figure 3.3: ABAQUS/CAE Rendering of the Finite Element Model with No Applied Uplift Pressure Distribution (Uplift Distribution 1)

Because no displacement or rotation boundary conditions were directly applied to the concrete dam, the model was run as a pseudo-static analysis where the gravity load was linearly increased from zero to 9.81 m/s^2 over the pseudo time period 0-1 and then the other loads were similarly ramped over a time period of 1-2. By first applying the gravity load, the full frictional resistance along the dam-foundation contact and the self weight of the dam were allowed to develop before applying the loads that act to overturn or slide the dam. It was found that if all of the loads were applied instantaneously at the start of the simulation, the static solution would not converge suggesting that a rigid body mode had developed and the system was unstable. In order to run the analysis, the model was meshed using plain strain bilinear quadrilateral elements.

3.3 Factor of Safety Analysis Using ABAQUS

To directly compare the factor of safety analysis outlined in Section 2.3.1 to results from the finite element modeling, vertical and shear stress were plotted as a function of distance along the dam-foundation contact, herein denoted as x, creating two stress distributions. These distributions were then integrated with respect to x using the trapezoidal rule (Equation (3.1)) to calculate the total vertical and shear forces. An example integration can be found on Figure 3.4. The forces were then used to conduct a factor of safety analysis using Equations (2.3) and (2.6). For the overturning calculations, it was assumed that the deformations of the dam were small enough to not significantly change the geometry. As a result, the length of the moment arms used to calculate the factor of safety against overturning by the classical gravity dam design method were also used in the factor of safety analysis using the finite element modeling results.

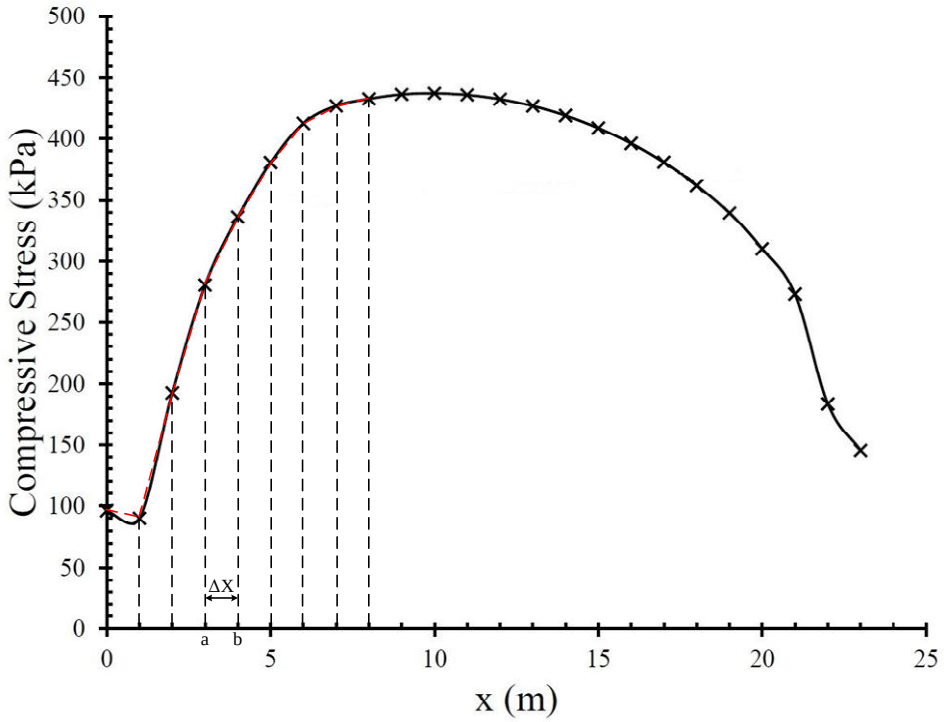

Figure 3.4: Example Numerical Integration Using the Trapezoidal Rule

$$T = \int_a^b f(x)\,dx \approx (b-a)\frac{f(a)+f(b)}{2} \tag{3.1}$$

During the second loading phase where the reservoir, uplift and soil pressures were being incrementally applied, there were some cases where the finite element model did not converge implying the development of a rigid body mode. Either the frictional resistance was overcome allowing the dam to slide or the dam overturned. Because the loads were linearly ramped up over the pseudo time period of 1-2, the time of the last converged time step represented the total percent of the loads applied to the dam before failure. In order to then calculate the factor of safeties, the total shear force developed at the last converged time step was first divided by the total percent of the loads applied to acquire the total shear that would have been attained had the system not failed. Then, this extrapolated value was used in the factor of safety analysis (see Appendix A for more details).

3.4 Finite Element Model and Classical Gravity Dam Design Method Comparisons

3.4.1 Finite Element Model Results

The classical gravity dam design methodology calculates a linear vertical stress distribution along a dam's base. As a result of the deformations, which are assumed to be zero in the classical method, the finite element model does not predict a linear distribution. A comparison of the two different methods for an example without uplift pressure at a friction angle of 30° can be found on Figure 3.5.

Figure 3.6 displays finite element vertical stress distributions for the no uplift cases and varying friction angles between the dam and foundation. The percentage assigned to each data series represents the percent of the total loads applied to the dam – i.e., the time of the last converged time step. As the friction angle decreased, it required less load to fail the dam. Low friction angles provide less shear resistance implying the systems failed due to sliding. Also, the

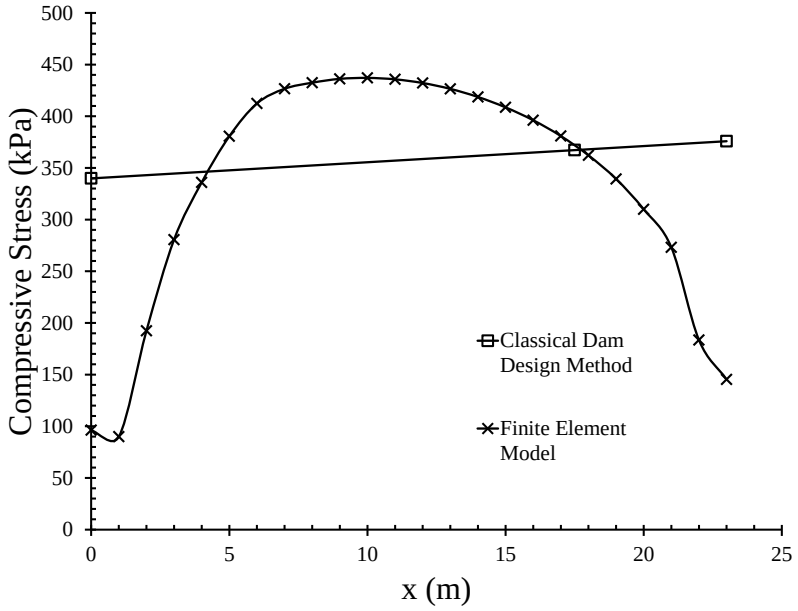

Figure 3.5: Vertical Compressive Stress Comparison for No Uplift Pressure and ϕ=30°

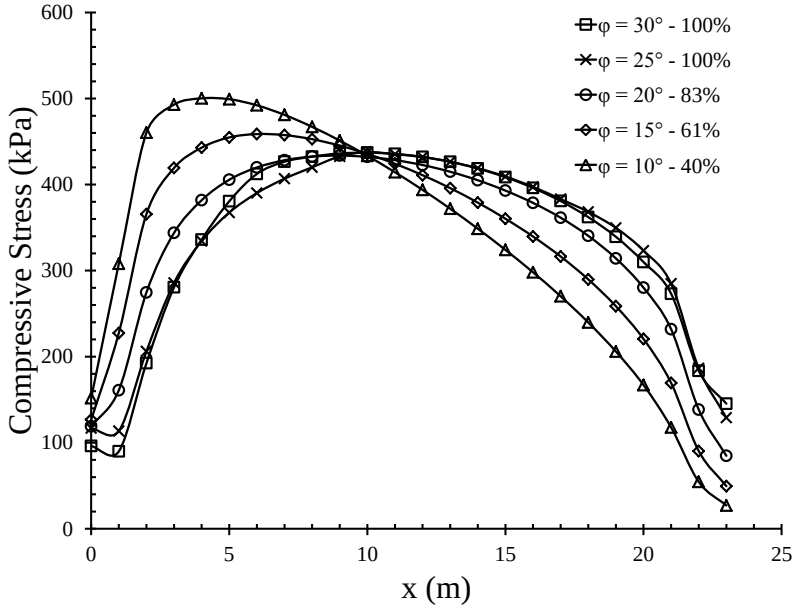

Figure 3.6: Vertical Compressive Stress for No Uplift with Varying Friction Angles

vertical stress distributions remained positive, or in compression, for all friction angles suggesting that in cases where the dam failed, it did not fail by overturning. In order to overturn, the dam

would have needed to lose contact with the rigid foundation sending the vertical stress to zero.

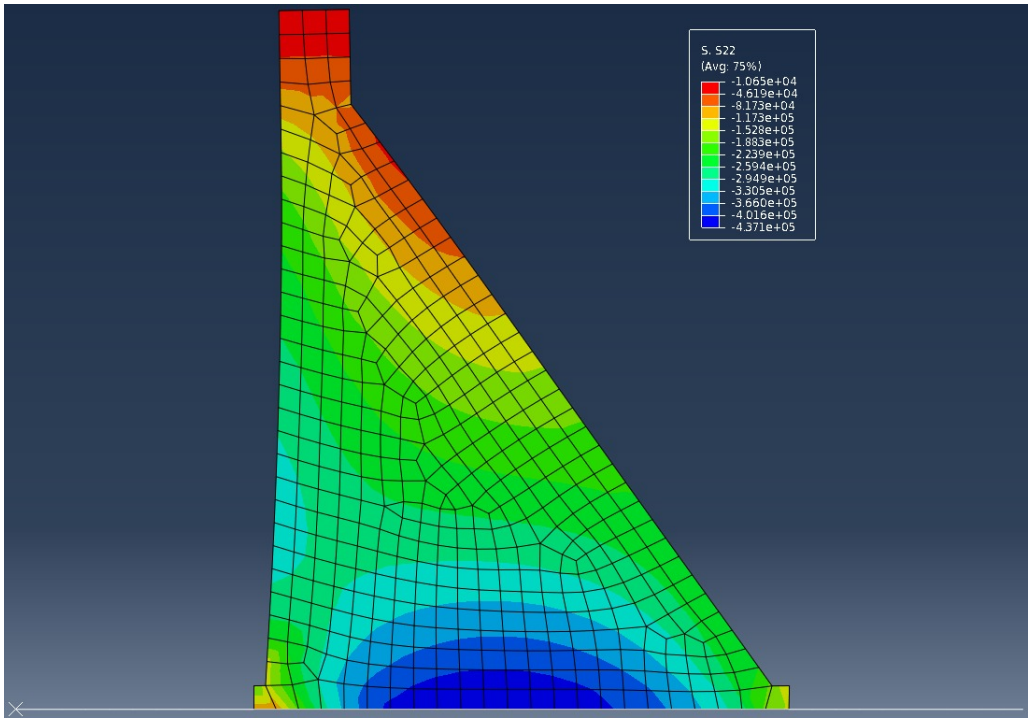

Figure 3.7: Deformed Geometry of Uplift Pressure Distribution 1 Magnified 3000 Times

Also, Figure 3.6 shows vertical stress distributions more concentrated toward the heel of the dam for lower friction angles. Because the lower friction angle simulations failed prior to the full reservoir and soil loads being applied, the dam did not deform as much in these scenarios. As the dam deforms, it primarily bends under the upstream reservoir pressure causing its centroid to shift slightly downstream, as seen on Figure 3.7. The two cases that did successfully complete, $\phi = 30°$ and $\phi = 25°$, show similar distributions suggesting that the dam deforms the same in each simulation regardless of friction angle.

A comparison of results from uplift distributions 1 through 3 can be found on Figure 3.8. As expected, at a constant friction angle of 30°, uplift distribution 1 (the no uplift pressure case) showed more frictional resistance to sliding than either uplift pressure distributions 2 or 3, as the finite element model was able to resist 100% of the pressures applied during the second loading phase. Also, the uplift case including drainage (distribution 3) resisted sliding better than the full

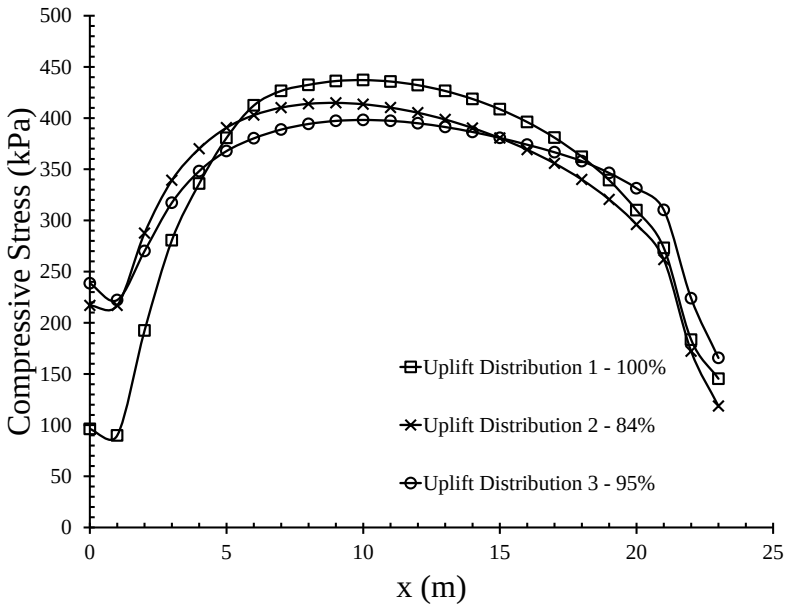

Figure 3.8: Vertical Compressive Stress for a Friction Angle of ϕ=30° and All Three Uplift Pressure Distributions

linear uplift pressure profile (distribution 2) allowing the 95% of the tractions to be applied before failing versus 84%.

3.4.2 Factor of Safety Comparisons

Results from the classical gravity dam design factor of safety analysis can be found in Table 3.1. As expected, the factor of safety against overturning does not change with respect to the friction angle between the dam and foundation, as the moments about the toe of the dam are not affected by the friction along the dam-foundation contact. It is significantly decreased by the inclusion of uplift pressure, which creates a higher overturning moment about the toe of the dam. Also, because drainage is designed to decrease the total uplift force acting on the dam's base decreasing the total uplift moment, the factor of safety against overturning is higher with a drain included than without one.

The factor of safety against sliding decreases by decreasing the friction angle, because less of the vertical force T is utilized to resist a sliding failure, as described by equation (2.3). Also, similar

to the overturning calculations, the factor of safety against sliding decreases with the addition of uplift pressure and is higher for the uplift model including a drain than the model without one; the vertical force T, essentially the effective vertical force, is lower with the inclusion of an uplift pressure distribution.

Table 3.1: Classical Dam Design and Finite Element Method Factor of Safety Analysis Comparisons

Uplift Model	Drain Location	Friction Angle	$FS_{sliding}$		$FS_{overturning}$	
			Classical	ABAQUS	Classical	ABAQUS
1	-	30°	1.33	1.34	3.89	3.78
1	-	25°	1.07	1.08	3.89	3.78
1	-	20°	0.84	0.84	3.89	3.78
1	-	15°	0.62	0.61	3.89	3.77
1	-	10°	0.40	0.39	3.89	3.77
2	-	30°	0.82	0.80	1.22	1.19
2	-	35°	0.99	0.97	1.22	1.19
2	-	40°	1.19	1.17	1.22	1.19
3	17.5 m	30°	0.93	0.92	1.71	1.67
3	17.5 m	35°	1.13	1.11	1.71	1.66

Despite the differences in vertical stress distributions along the dam's base between the classical dam design method and the finite element models, the factor of safety against overturning and sliding calculated using data from the finite element models and the methodology described in Section 3.3 yield nearly identical results to the classical design method results. The results were comparable even in cases where the finite element model did not fully converge due to reduced frictional resistance or the inclusion of uplift pressure, as seen in Table 3.1 where the calculated factor of safety against sliding was <1. The similarity between the two sets of data suggests that the finite element method can yield reasonable results for basic geometry and material conditions as far as the factor of safety is concerned. With the finite element framework, however, many more complicated mechanics aspects can be incorporated into the system and used by engineers to assess the safety of a dam in cases where the fundamental assumptions of the classical methodology are violated, such as more complicated concrete dam constitutive relationships, atypical reservoir conditions, or time-dependent loading situtations.

Chapter 4

Gravity Dam with a Deformable Foundation Model

4.1 Finite Element Model Development in ABAQUS

Using the same example dam from Watermeyer (2006), uplift pressure distributions described in Section 3.1, and the same material properties for the concrete gravity dam described in Section 3.2, the rigid foundation from the models in Chapter 3 was replaced with a deformable rock foundation. Due to the expected small strains, the rock masses were idealized as homogeneous, linear isotropic elastic materials. A table with the different rock types and their respective material properties follows.

Table 4.1: Deformable Foundation Material Properties

Material	Poisson's Ratio ν	Young's Modulus $E_{material}$ (GPa)	Stiffness Ratio $E_{material}/E_{concrete}$	Density ρ (kg/m^3)
Granite	0.2	40	1.94	2700
Sandstone	0.33	10.5	0.51	2000
Concrete	0.2	20.67	1	2396
Hard Granite	0.2	70	3.39	2700
Steel	0.3	200	9.68	8000

These materials were chosen to provide a wide range of stiffnesses relative to the stiffness of the concrete gravity dam in order to study the behavior of different types of rock foundations. The ratio of the Young's modulus of concrete to the moduli of the other foundation materials can be found in Table 4.1 in the Stiffness Ratio column. Steel was included as a foundation material to be an upper limit on the stiffness of geologic materials and to bridge the gap between the hard granite

and rigid cases.

A rendering of the deformable rock foundation finite element model as implemented in ABAQUS/CAE can be found on Figure 4.1. The foundation rock was made to extend 50 meters upstream, downstream, and under the dam, and then was fixed in both the x (horizontal) and y (vertical) directions along the outside boundaries. This was done to simulate an expansive, monolithic rock mass supporting the dam. Contact between the dam and foundation was modeled using the same contact model that was described in Section 3.2. As a result, the same psuedo-time scheme, also outlined in Section 3.2, was implemented to allow the frictional resistance to sliding to develop prior to applying the loading from the upstream reservoir. In addition to the loading on the gravity dam, tractions were applied to the foundation accounting for the upstream and downstream hydrostatic water pressure as well as the downward pressure of the three uplift pressure distributions. As water pressure acts equally in all directions, any uplift pushing the gravity dam upwards must also push the foundation downwards.

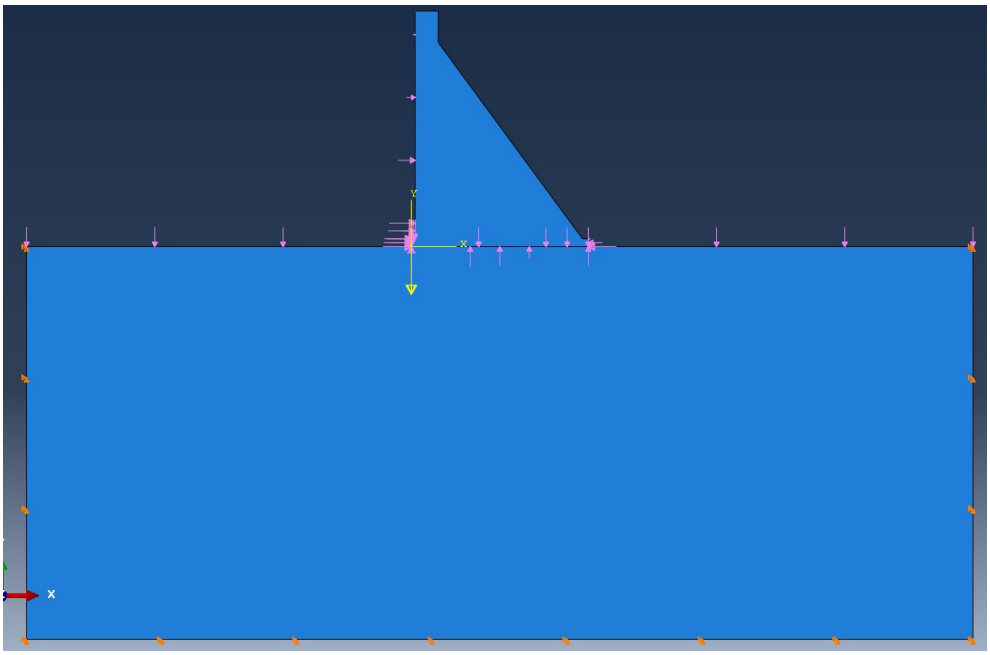

Figure 4.1: ABAQUS/CAE Rendering of the Finite Element Model with Uplift Distribution 3

4.2 Finite Element Model and Classical Gravity Dam Design Method Comparisons

4.2.1 Finite Element Model Results

Figures 4.2 and 4.3 show the finite element modeling results of a deformable granite and sandstone foundation without any applied uplift pressure. Plots of the vertical compressive stress along the dam-foundation contact for both foundations without uplift pressure and for varying contact friction angles can be found on Figures 4.4 and 4.5 respectively. These plots display similar trends to the rigid foundation case from Chapter 3. For the analyses that ran to completion (100%), the vertical stress distributions are roughly identical regardless of the friction angle. However, the lower the friction angle, the lower the sliding resistance along the dam-foundation contact. Consequently, a smaller fraction of the upstream reservoir pressure was applied to the system prior to the finite element model failing to converge. Lower lateral pressure resulted in less lateral deformation of the dam causing the centroid of the dam to shift upstream and the stress distributions to change accordingly. Also, all of the vertical stress results remained in compression meaning none of the gravity dam models failed by overturning; the finite element models that didn't fully converge likely failed through sliding instead.

Also similar to the trends discussed in Chapter 3, Figures 4.6 and 4.7 are plots for both a granite and sandstone deformable foundation with uplift pressure distributions 1 through 3. For both foundation materials, the no uplift pressure case (distribution 1) produced higher frictional resistance to sliding than the uplift pressure with drainage case (distribution 3) than the full linear pressure profile case (distribution 2) given a constant friction angle of 30°.

Lastly, with the addition of a deformable foundation, it is important to determine if the generated stresses were large enough to induce crushing in either the rock or concrete dam. The unconfined compressive strengths of concrete, granite and sandstone are approximately 28, 150, and 95 MPa, respectively. The maximum vertical compressive stress generated during either simulation (see Figures 4.2 and 4.3) was directly under the dam along the bottom edge of the foundation at

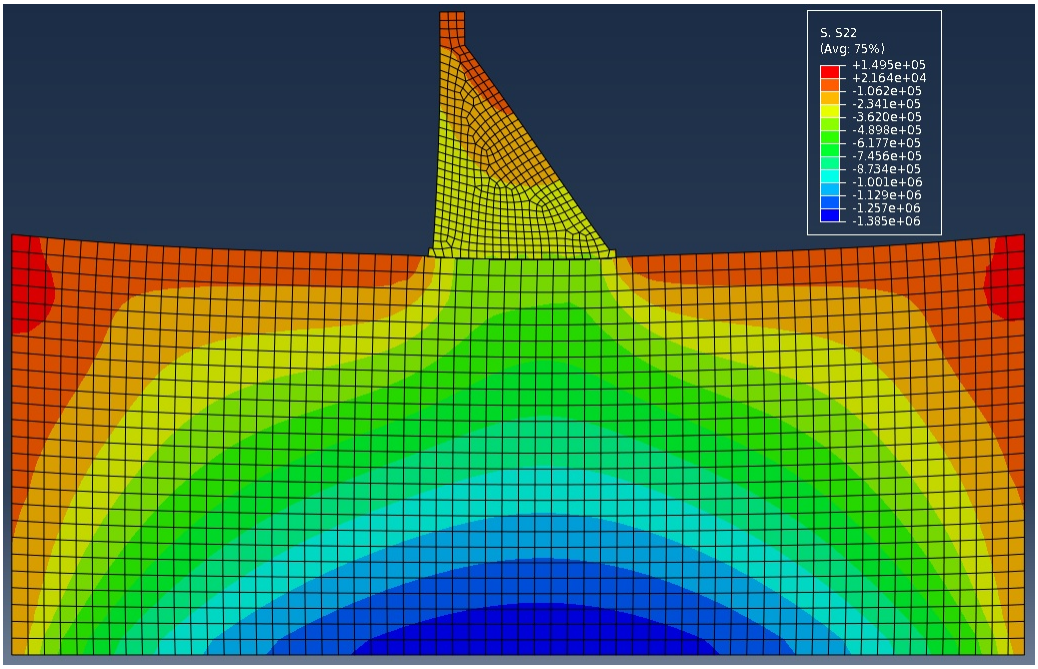

Figure 4.2: Deformed Geometry with Vertical Stress Contours Magnified 3000 Times for a Deformable Granite Foundation with Uplift Pressure Distribution 1

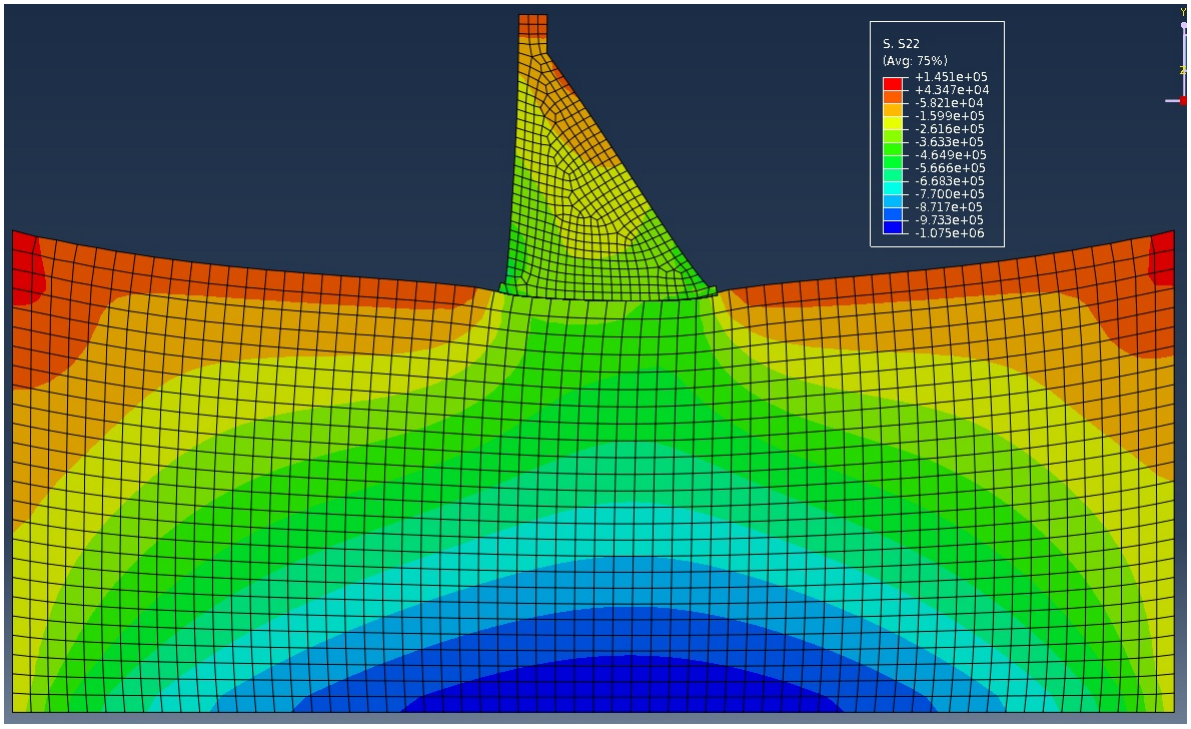

Figure 4.3: Deformed Geometry with Vertical Stress Contours Magnified 3000 Times for a Deformable Sandstone Foundation with Uplift Pressure Distribution 1

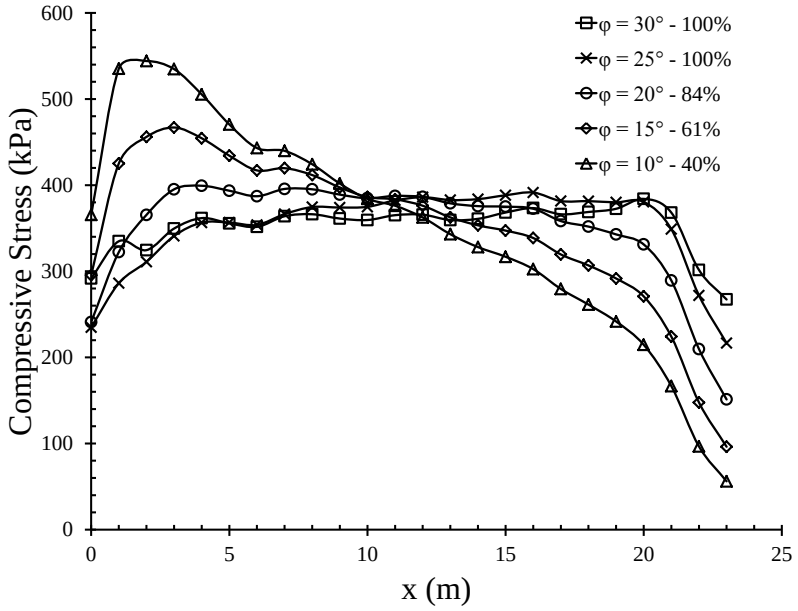

Figure 4.4: Vertical Compressive Stress for a Deformable Granite Foundation with Varying Friction Angles without Uplift Pressure

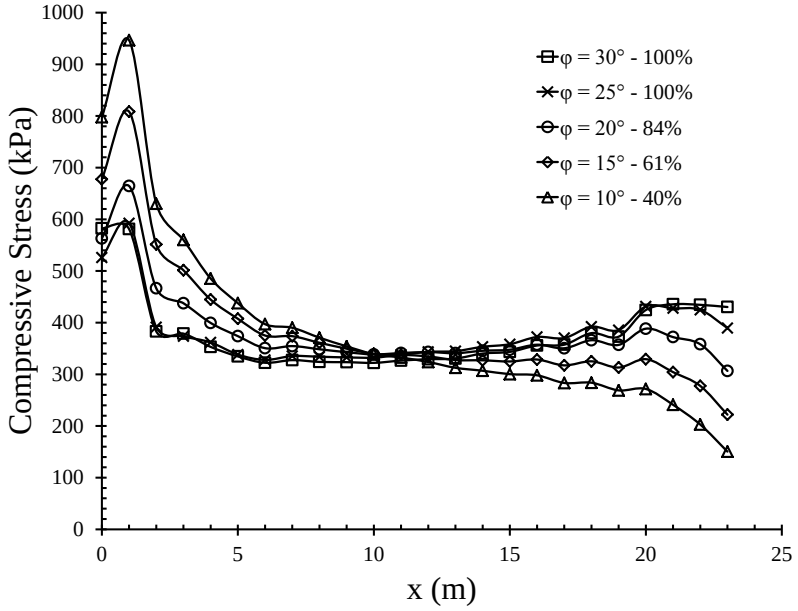

Figure 4.5: Vertical Compressive Stress for a Deformable Sandstone Foundation with Varying Friction Angles without Uplift Pressure

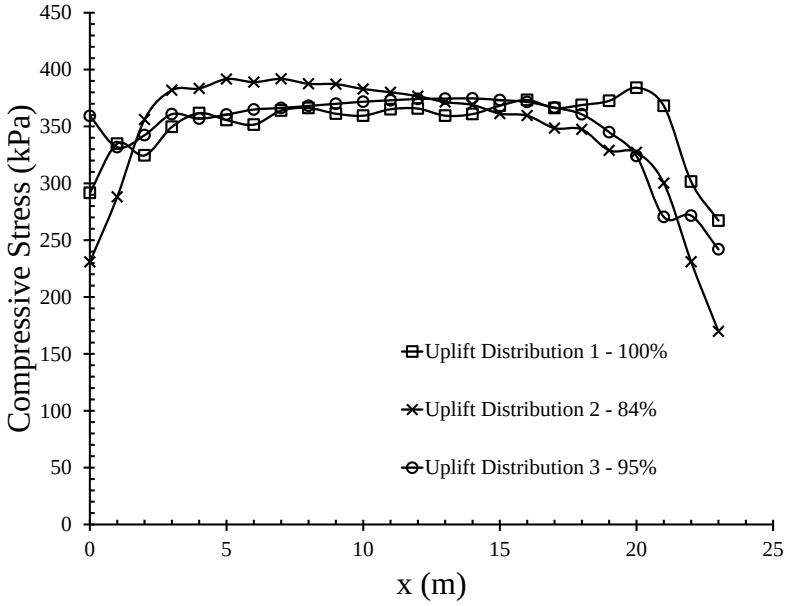

Figure 4.6: Vertical Compressive Stress for a Deformable Granite Foundation with a Friction Angle of ϕ=30°

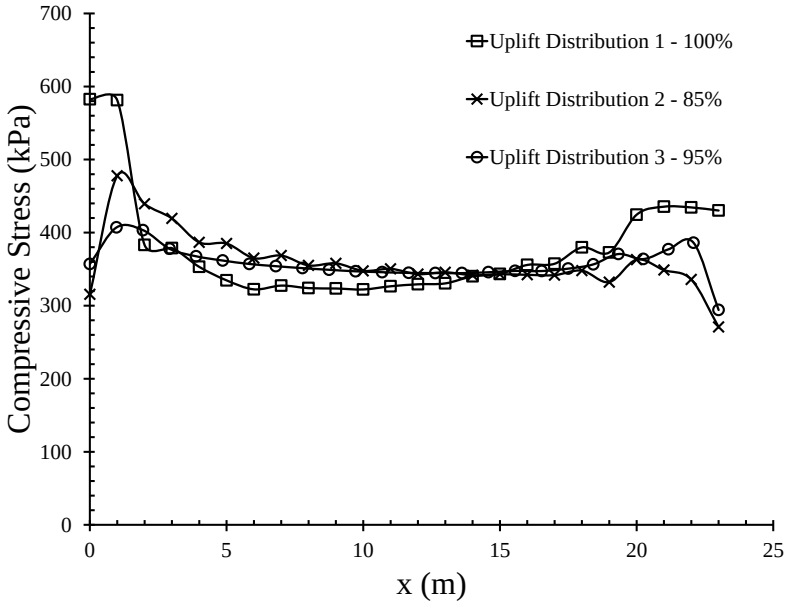

Figure 4.7: Vertical Compressive Stress for a Deformable Sandstone Foundation with a Friction Angle of ϕ=30°

a value of just over 1 MPa. Along the dam-foundation contact, the highest compressive stress was just under 1 MPa during the sandstone foundation with contact friction angle at 10° case found on Figure 4.5. Neither of these stresses were large enough to eclipse the compressive strengths of any of the materials, and as a result, it is reasonable to assume no crushing was induced.

4.2.2 Comparisons of Different Foundation Materials

A plot comparing the five different foundation materials modeled given a friction angle of 30° and uplift pressure distribution 1 can be found on Figure 4.10. As the foundation materials stiffen relative to the concrete dam, the vertical compressive stress distributions gradually change from concave up to concave down, ultimately resembling the the rigid foundation case from Figure 3.6. Under identical loading conditions, the stiffer the foundation the less it will deform, as shown by Figures 4.8 and 4.9 that compare the horizontal deformation of the granite and sandstone foundations respectively. As a result, the orientation of the concrete dam doesn't change as much with respect to the foundation. The softer foundations, like the sandstone model, deform more under the dead weight of the dam causing the stress distributions to change. The heaviest section of the dam (the upstream section) causes the upstream side of the less-stiff foundation to deflect farther tilting the dam slightly upstream. As a result, the highest vertical compressive stress is in the upstream section as more of the dam's self-weight is over this section of the foundation.

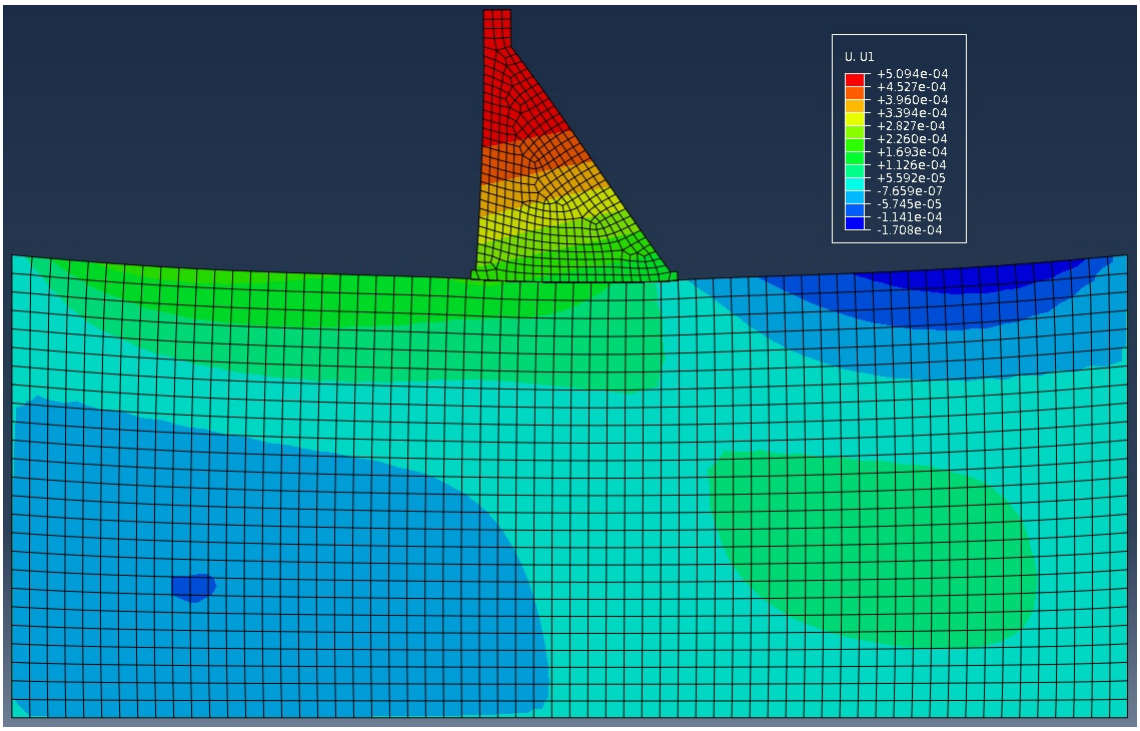

Figure 4.8: Deformed Geometry with Horizontal Displacement Contours Magnified 3000 Times for a Deformable Granite Foundation with Uplift Pressure Distribution 1

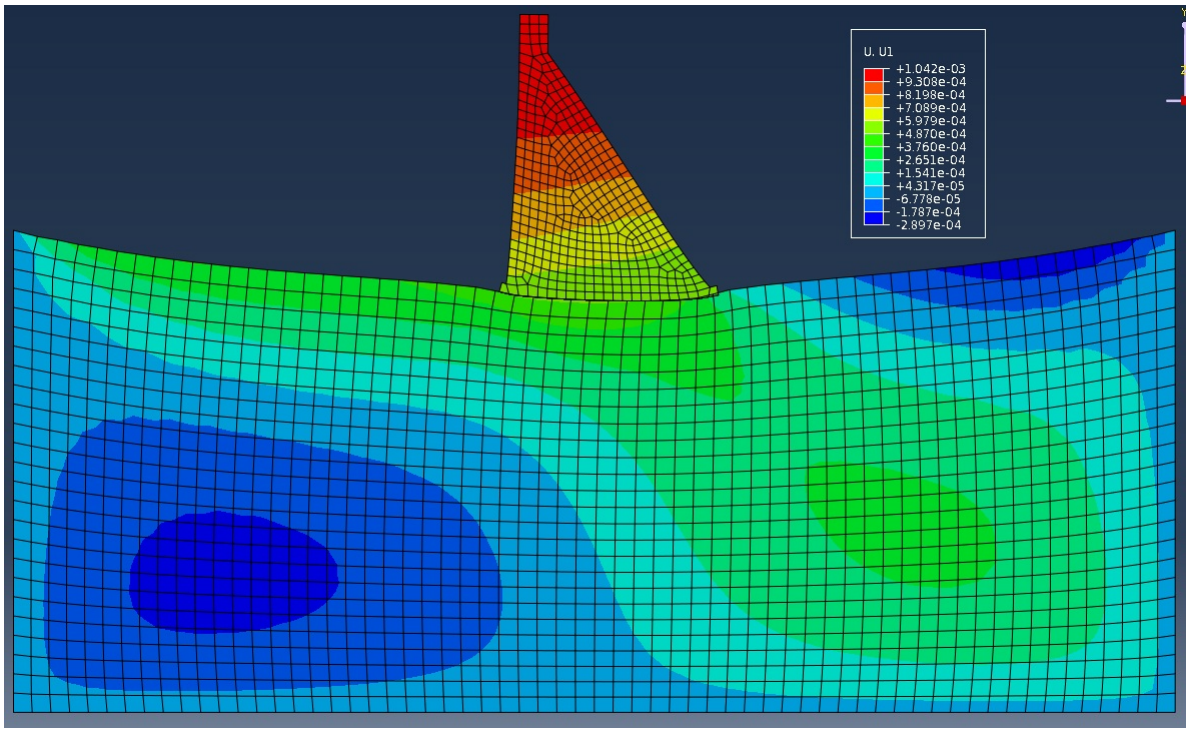

Figure 4.9: Deformed Geometry with Horizontal Displacement Contours Magnified 3000 Times for a Deformable Sandstone Foundation with Uplift Pressure Distribution 1

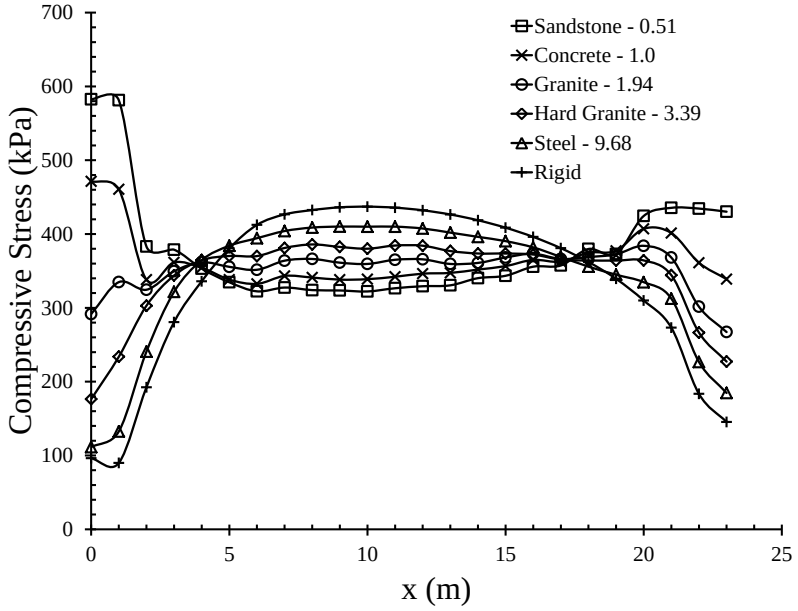

Figure 4.10: Vertical Compressive Stress for Various Deformable Foundations given No Uplift Pressure and ϕ=30°

4.2.3 Factor of Safety Comparisons

Using the same methodologies outlined in Section 2.3.1 and Section 3.3, an analysis was completed comparing factors of safety calculated using the classical gravity dam design method and the deformable rock foundation finite element results. Table 4.2 contains comparisons between the classical method and ABAQUS finite element results given a deformable granite foundation, and Table 4.3 contains similar results, but given a deformable sandstone foundation. Despite the additional complexity of a deformable foundation in the finite element models, the factors of safety calculated from the finite element results are highly comparable to the classical design method results. As expected due to the similarity between stiffer foundation materials and the rigid foundation results, the factors of safety for the granite foundation more closely resemble the classical results. However, the factors of safety from the less stiff sandstone foundation do begin to slightly deviate from the classical method. Particularly, the factor of safety against overturning for the uplift pressure distribution 1 are higher for the finite element results than the classical results, likely due to the slight rotating of the concrete dam discussed in Section 4.2.2 creating higher resisting moments. However, the maximum deviation between the two sets of results is 5.2% (the cases with friction angles of 15° and 10°), so the difference between the two is small.

Table 4.2: Factor of Safety Analysis for a Deformable Granite Foundation versus the Classical Design Method

Uplift Model	Drain Location	Friction Angle	$FS_{Sliding}$		$FS_{Overturning}$	
			Classical	ABAQUS	Classical	ABAQUS
1	-	30°	1.33	1.33	3.89	3.87
1	-	25°	1.07	1.08	3.89	3.87
1	-	20°	0.84	0.84	3.89	3.87
1	-	15°	0.62	0.60	3.89	3.87
1	-	10°	0.40	0.38	3.89	3.87
2	-	30°	0.82	0.81	1.22	1.20
2	-	35°	0.99	0.98	1.22	1.20
2	-	40°	1.19	1.16	1.22	1.19
3	17.5 m	30°	0.93	0.96	1.71	1.68
3	17.5 m	35°	1.13	1.19	1.71	1.67

Table 4.3: Factor of Safety Analysis for a Deformable Sandstone Foundation versus the Classical Design Method

Uplift Model	Drain Location	Friction Angle	$FS_{Sliding}$		$FS_{Overturning}$	
			Classical	ABAQUS	Classical	ABAQUS
1	-	30°	1.33	1.36	3.89	4.02
1	-	25°	1.07	1.09	3.89	4.06
1	-	20°	0.84	0.84	3.89	4.09
1	-	15°	0.62	0.59	3.89	4.10
1	-	10°	0.40	0.35	3.89	4.10
2	-	30°	0.82	0.83	1.22	1.24
2	-	35°	0.99	1.00	1.22	1.22
2	-	40°	1.19	1.17	1.22	1.21
3	17.5 m	30°	0.93	0.94	1.71	1.72
3	17.5 m	35°	1.13	1.14	1.71	1.70

Also, it should be stressed that even in cases where the classical gravity dam design method predicited an unstable system (factors of safety <1), the finite element data produced similar results. By using the methodology described in Section 3.3, the total forces calculated from the stress distributions at the last convereged psuedo-timestep produced comparable factors of safety when plugged into the classical gravity dam equations. Although the finite element model did not fully converge, important infomation about the stability of the system was still possible to obtain, analyze and even be used as a predictive tool like the classical design method.

Because the inclusion of homogeneous and isotropic linear elastic deformable rock foundations in the finite element models yield similar results to the classical gravity dam design method, one can infer that the finite element models predict reasonable factors of safety. The relatively small strains predicted by the models do not violate the major assumptions of the classical method. When the stress distributions, which do vary considerably from the classical method, are integrated into forces, the calculated factors of safety are nearly identical. Though with these finite element models, additional layers of complexity can be added to more accurately replicate the conditions in the field, such as anisotropic material stiffnesses, which are particularly important for jointed rocks and rocks with highly defined bedding planes, more complicated consitutive relationships for the dam and foundation, and the nucleation and propagation of cracks in both materials.

Chapter 5

Gravity Dam with Coupled Solid Skeleton Deformations and Porous Media Fluid Flow

5.1 Finite Element Model Development in ABAQUS

The previous two concrete gravity dam finite element models (described in Chapters 3 and 4) included uplift pressures by applying tractions to the model as boundary conditions. Although the factor of safety results were comparable to the classical gravity dam design method, a more physically accurate method to include uplift is by allowing for porous media flow through the dam system. Water pressures are then developed through the coupling of the solid skeletal deformations and seepage equations, and not through artifically applying a boundary condition.

Table 5.1: Poromechanical Material Properties

Material	Permeability k (m/sec)	Initial Void Ratio e_o
Sandstone	$1x10^{-10}$	0.2
Concrete	$1x10^{-12}$	0.05

Figure 5.1 shows an ABAQUS/CAE rendering of the finite element model with poromechanics. The model is similar to the deformable rock foundation model from Chapter 4, but without any applied uplift distributions along the dam-foundation contact. The other traction boundary conditions representing water pressures from the upstream and downstream reservoir were kept, and additional pore water pressure boundary conditions were added to inform the flow equations. ABAQUS automatically generates no flux boundary conditions where pore pressure boundaries

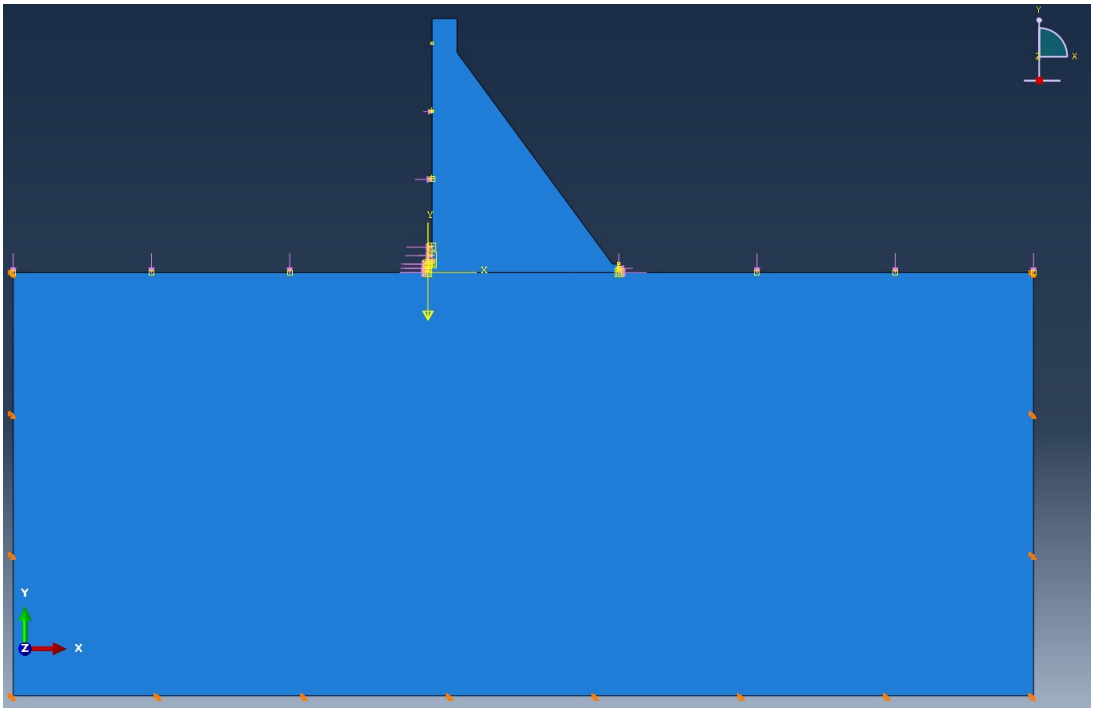

Figure 5.1: FEM Model Geometry and Boundary Conditions

aren't specified; therefore, no flow was permitted along the sides and bottom of the foundation or out of the downstream face of the dam, except into the downstream reservoir. Also, an isotropic permeability tensor and initial void ratio were set for both the concrete dam and a deformable sandstone foundation. The material properties used can be found in Table 5.1.

Poromechanical analyses in ABAQUS are run using the "soils" step, which allows for either transient or steady-state analyses. It was chosen to use the steady-state feature in order to more closely match the analyses in previous chapters. Transient analyses would be useful to see the build up of pore pressures over time, but due to the relatively low permeability of rock and concrete, they would need to run for a long time in order to reach steady-state. Like the pseudo-time scheme outlined in Section 3.2, the gravity load was applied over 0-1 pseudo-seconds, allowing the frictional resistance to build up prior to applying the traction and pore pressure boundary conditions over the final 1-2 pseudo-seconds.

5.2 Finite Element Model and Classical Gravity Dam Design Method Comparisons

5.2.1 Finite Element Model Results

Typical vertical effective stress, pore water pressure and horizontal displacement contours for the poromechanical analyses can be found on Figures 5.2, 5.3 and 5.4. Unlike the previous finite element model results, the addition of pore fluid flow predicts much greater horizontal displacement of the gravity dam relative to the foundation rock. Figure 5.4 shows noticeable lateral displacement at only 1500 times magnification, as can be seen by the overlap of the dam and foundation in the magnified deformed rendering; Figure 4.9 shows hardly any lateral displacement at 3000 times magnification. This is because the poromechanical model is directly using the effective stress along the dam-foundation contact to determine the frictional resistance to sliding. The deformable rock foundation models of Chapter 4 do not directly account for the effective stress, but instead attempt to mimic those conditions by the application of the uplift pressure tractions. In other words, the value of S22, vertical stress in the deformable foundation models and vertical effective stress in the poromechanical models, which is directly related to the developed frictional resistance, is greater in the models without the addition of poromechanics than with pore fluid flow.

The effective vertical stress and pore water pressure along the dam-foundation contact given a friction angle of 30° can be found on Figure 5.5. The total stress was calculated by adding the effective vertical stress (S22) and pore water pressure (POR) at each point along the contact (x). The pore water pressure is nearly linear decreasing from the full upstream reservoir pressure head to the downstream reservoir pressure head, as is the assumption in the classical gravity dam design method. The deviations from linearity are caused by the pore fluid flow through the dam heel and toe.

Figure 5.6 shows the total stress along the dam-foundation contact for varying friction angles, and also includes the percent of the total loads applied to the dam model. The finite element model did not fully converge for the case with a friction angle of 30° only allowing 90% of the boundary

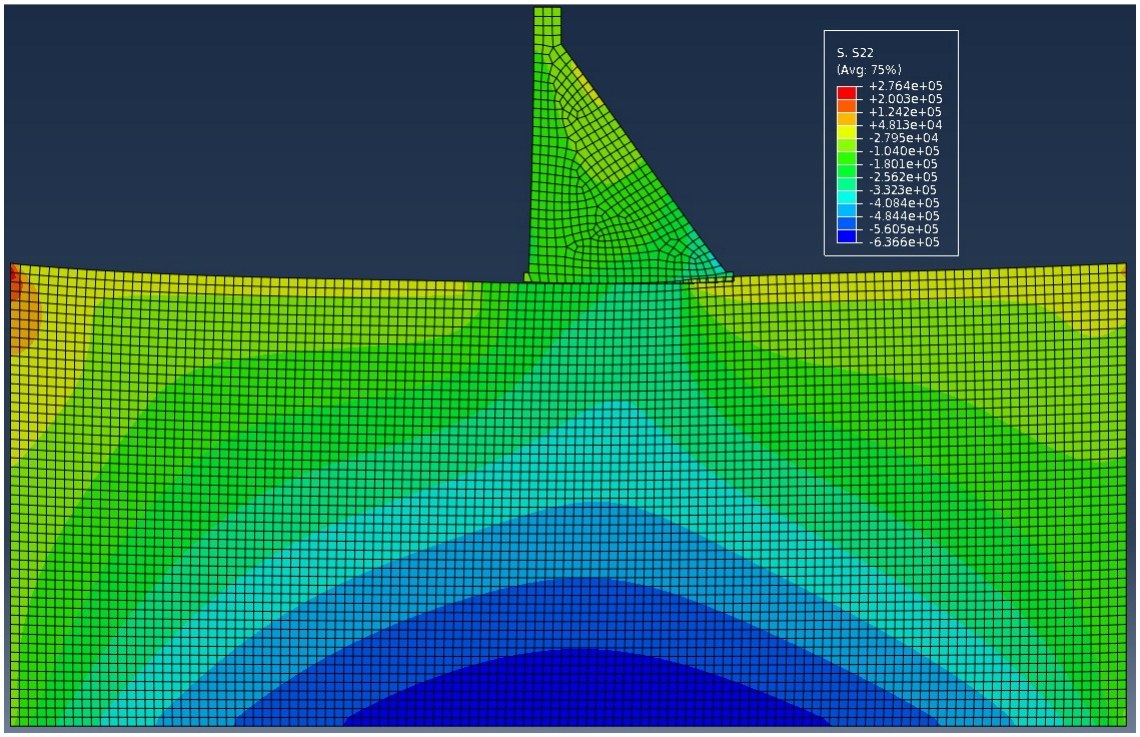

Figure 5.2: Deformed Geometry with Vertical Effective Stress Contours Magnified x1500

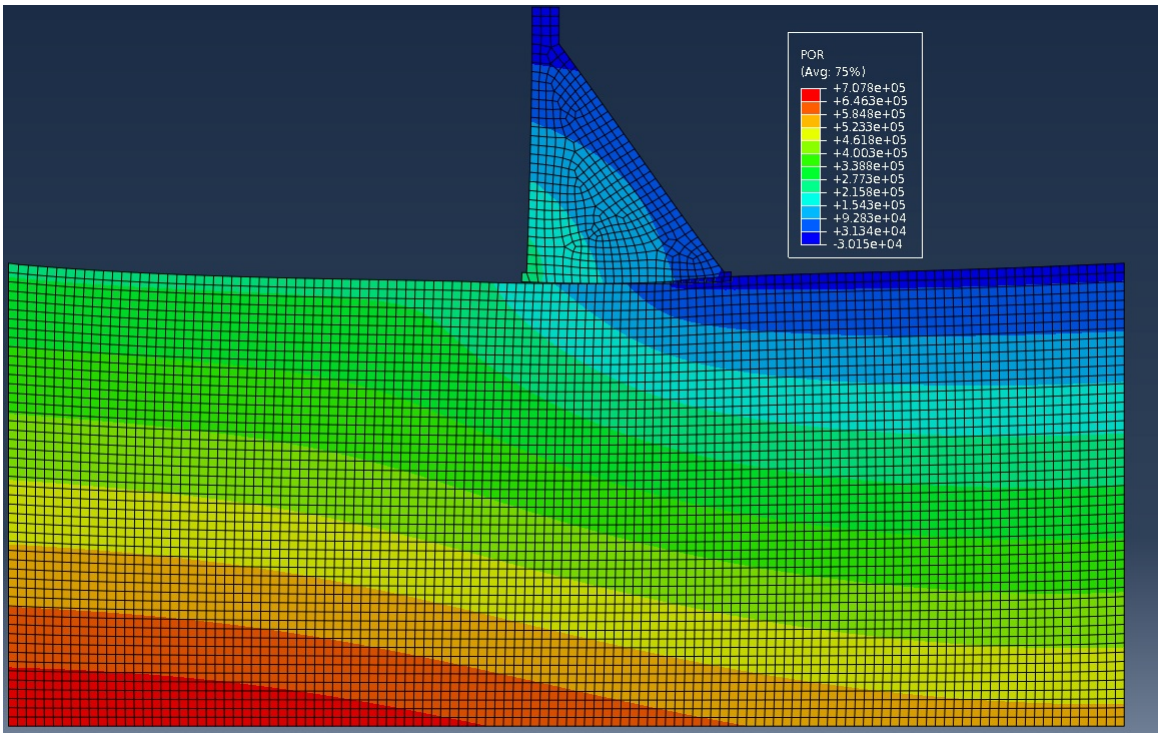

Figure 5.3: Deformed Geometry with Pore Water Pressure Contours Magnified x1500

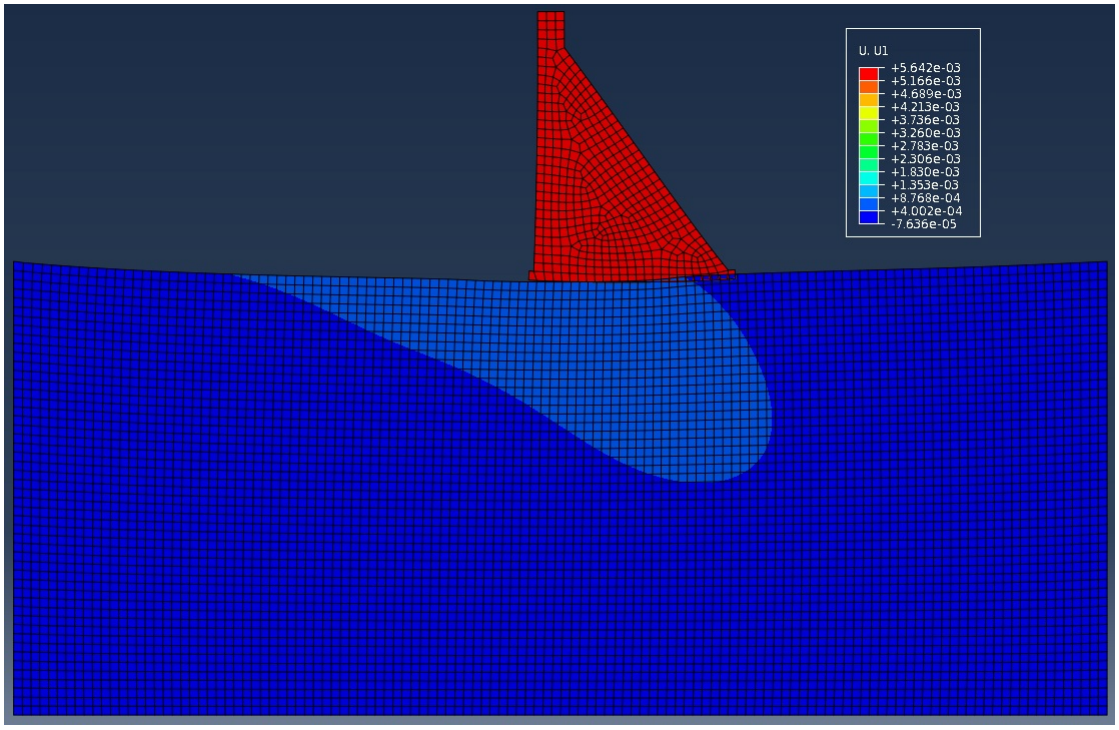

Figure 5.4: Deformed Geometry with Horizontal Displacement Contours Magnified x1500

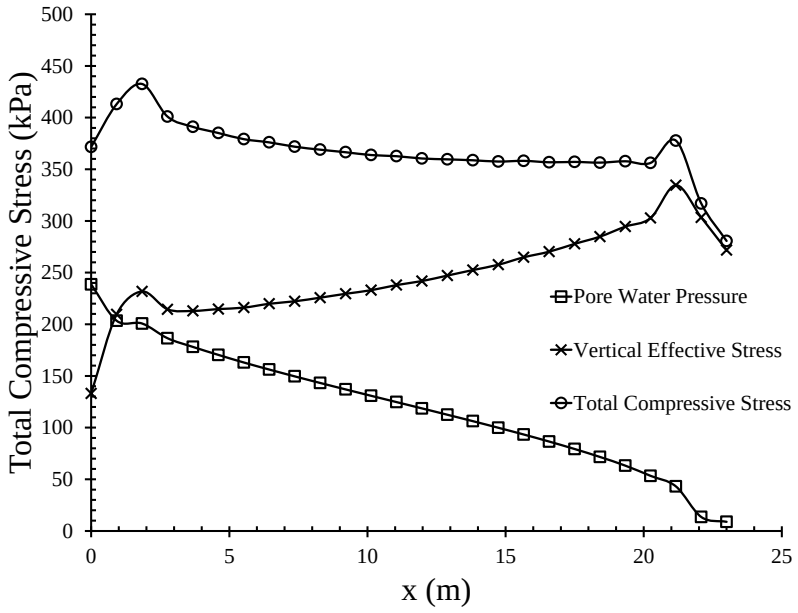

Figure 5.5: Vertical Effective Stress, Pore Water Pressure, and Total Stress Along the Dam Path Given ϕ=30°

conditions to be applied before failure, but the models did converge for the two higher friction angles. When fully converged, the total stress solutions do not depend on the friction angle of the contact.

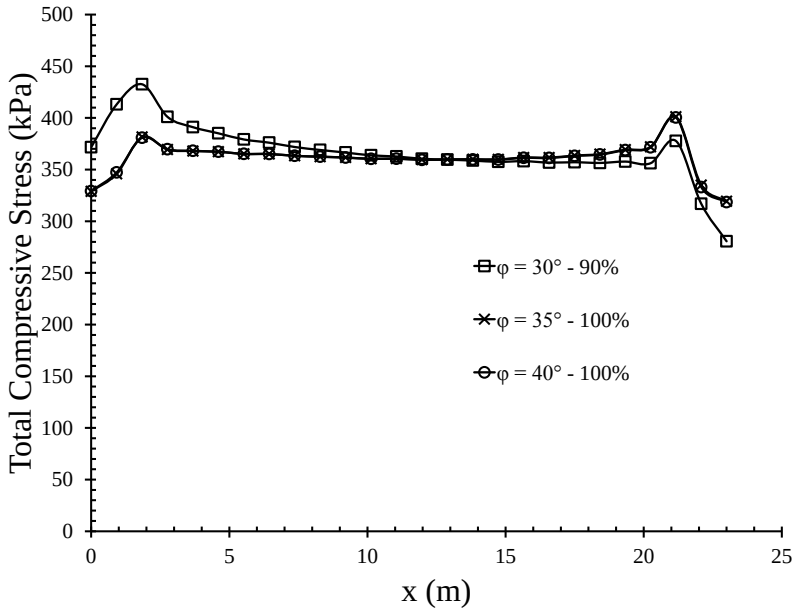

Figure 5.6: Total Compressive Stress Along the Dam Path for Various Friction Angles

Also, the total stress distributions were slightly dependent on where the effective stress was calculated. Figure 5.7 displays the total stress distributions for the base of the dam (Poromechanics – Dam Path) and the top of the foundation (Poromechanics – Foundation Path). Although similar, the solutions are different, because the stress is calculated at the Gauss points and then extrapolated to the sides of the element. The stress solution does not need to be continuous (although the pore pressure solution does), and the averaging techniques ABAQUS employed for the results displayed in Chapters 3 and 4 that make the stress solutions continuous are not as effective for poromechanical analyses. However, the differences between the two solutions are small, and both solutions agree closely with the results from the deformable sandstone foundation with uplift pressure distribution 2 (the linear uplift pressure profile) for a friction angle of 30°, also displayed on Figure 5.7.

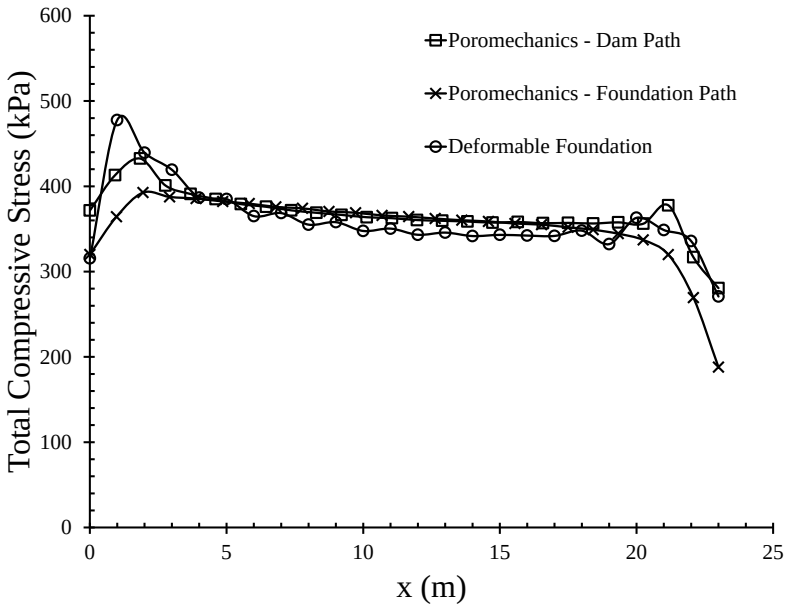

Figure 5.7: Comparisons between Dam and Foundation Paths in the Poromechanics and a Deformable Sandstone Foundation

5.2.2 Isotropic versus Anisotropic Permeability in the Sandstone Foundation

Previous results describe cases where the permeability of the sandstone foundation was considered isotropic; yet the permeability of rock, especially sedimentary rocks with defined bedding planes as sandstones often are, is better described with an anisotropic permeability tensor. Flow is generally preferred in the direction of the bedding planes. The following section contains the results of two simple simulations replacing the isotropic permeability of the foundation with one case where the permeability in the x-direction is much lower than the y-direction (denoted "Low x") and one where the y-direction permeability is lower than the x-direction (denoted "Low y"). Table 5.2 contains the two sets of material properties used for the sandstone foundation. The purpose of these simulations was to demonstrate the effect of anisotropy in that more focus was placed on the relative difference between k_x and k_y and not necessarily how accurate their values were. Recall that the isotropic permeability of the sandstone foundation was taken to equal $1\text{x}10^{-10}$ (m/sec) (see Table 5.1). As a result, the permeability of the "low" direction was assumed to be that same

value, and the "high" direction was taken to be a factor of 10^5 as permeable.

Table 5.2: Material Properties for Isotropic versus Anisotropic Permeability in the Sandstone Foundation

Description	x-Permeability k_x (m/sec)	y-Permeability k_y (m/sec)
"Low x"	$1\text{x}10^{-10}$	$1\text{x}10^{-5}$
"Low y"	$1\text{x}10^{-5}$	$1\text{x}10^{-10}$

In order to implement these two simulations into ABAQUS, the basic poromechanical model outlined in Section 5.1 was taken and then slightly altered. In the material property definition of sandstone, the isotropic permeability was replaced with the orthotropic permeability option in order to define the permeability in two orthogonal directions (k_{11} and k_{22}). ABAQUS allows for the definition of fully anisotropic permeability tensors, but for the purposes of this study, the orthotropic option sufficed. After the permeability tensor definition, ABAQUS also requires the user to create a material orientation in order to define the 11 and 22 directions, which were taken to be x and y in these examples.

Figures 5.8 and 5.9 display ABAQUS/CAE renderings of vertical effective stress and pore water pressure contours given a sandstone foundation with the "low x" anisotropic permeability tensor. Similar renderings for the "low y" case can be found on Figures 5.10 and 5.11. The most obvious differences between the two sets of results were the pore pressure distributions in the system's foundation. With flow preferred in the y-direction, as in the "Low x" case, one can imagine a flow net under the dam where only as the water nears the bottom no flux boundary is it forced to flow under the dam. In the opposite case, flow was preferred in the x-direction. An accompanying flow net would have the flow quickly turning under the dam after entering from the upstream reservoir. The result is a distribution that appears nearly hydrostatic just away from the dam-foundation contact.

A comparison of the vertical effective stress and pore water pressure solutions along the dam-foundation contact for both anisotropic cases as well as the isotropic permeability case of

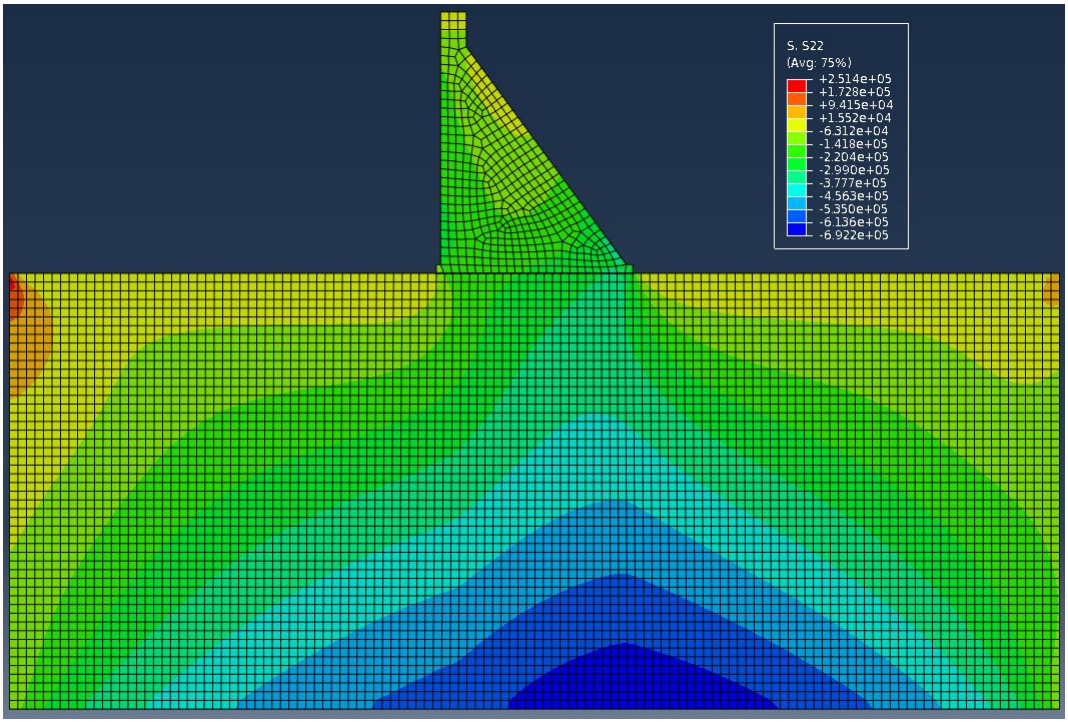

Figure 5.8: Dam Geometry with Low x Permeability in the Foundation and Vertical Effective Stress Contours

the previous section can be found on Figure 5.12. As is apparent, the anisotropic distributions do not change significantly from the isotropic case. According to the simulations, the "Low x" case was slightly less stable than the "Low y" case, which in turn was slightly less stable than the isotropic case. The "Low x" percent completion was 87.7%, which was the lowest of the three, but the three values are too similar to draw any significant conclusions. In other words, the inclusion of anisotropic permeability in a dam's foundation does significantly change the pore pressure distribution in the foundation, but doesn't seem to effect the uplift pressure acting on the dam itself.

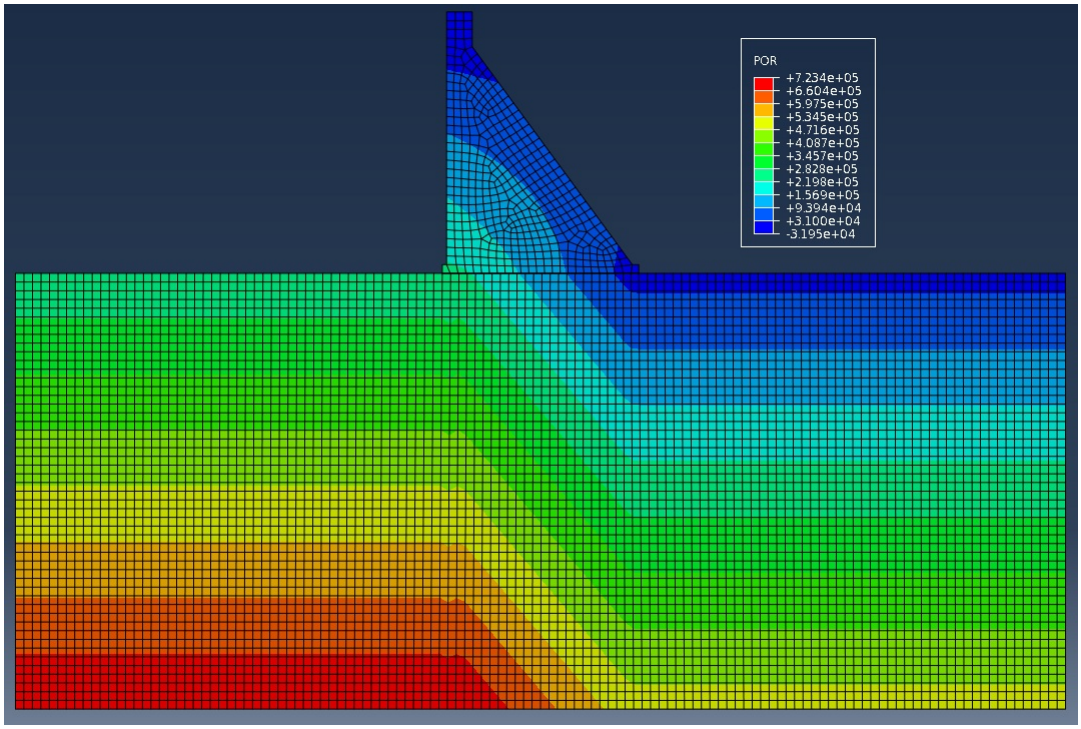

Figure 5.9: Dam Geometry with Low x Permeability in the Foundation and Pore Water Pressure Contours

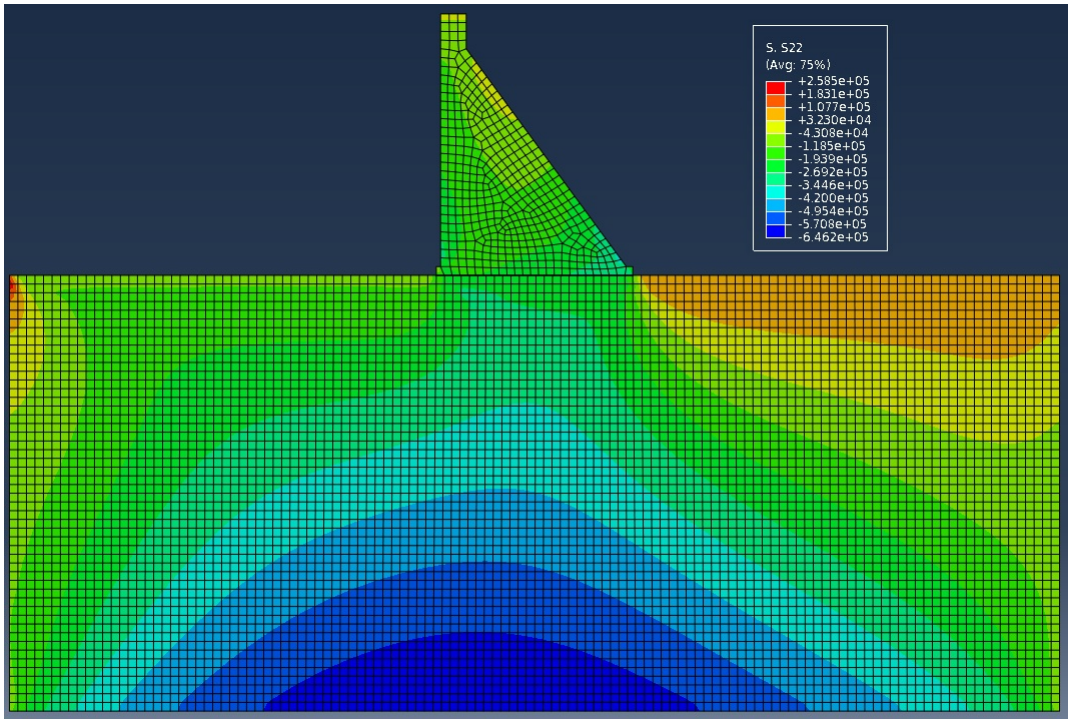

Figure 5.10: Dam Geometry with Low y Permeability in the Foundation and Vertical Effective Stress Contours

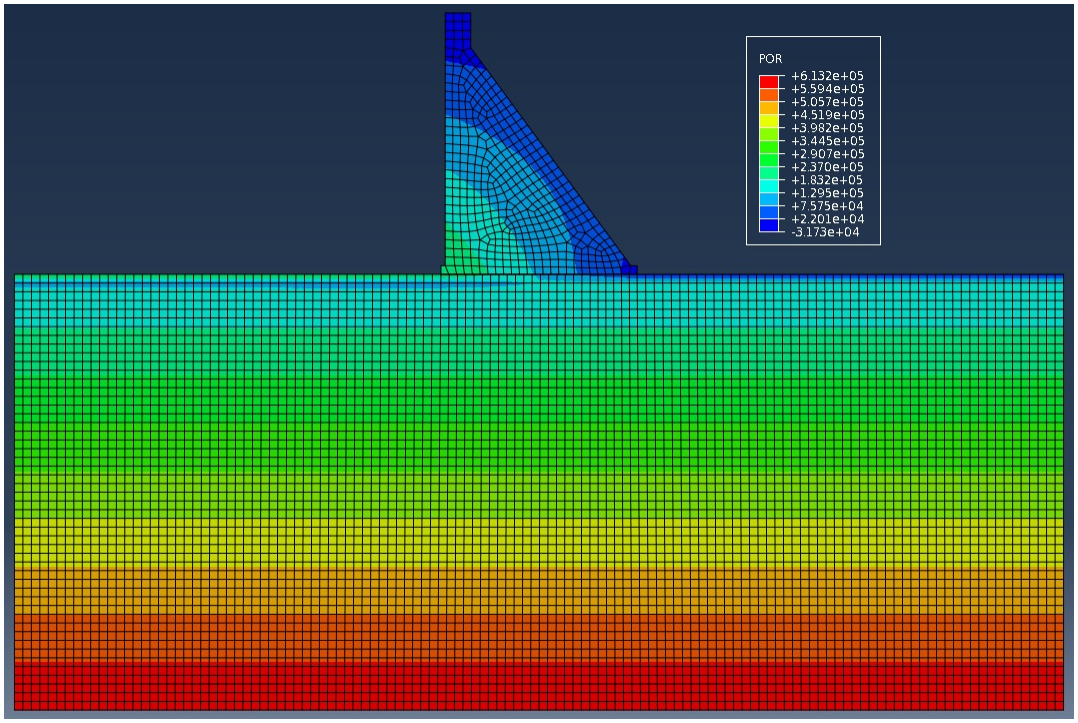

Figure 5.11: Dam Geometry with Low y Permeability in the Foundation and Pore Water Pressure Contours

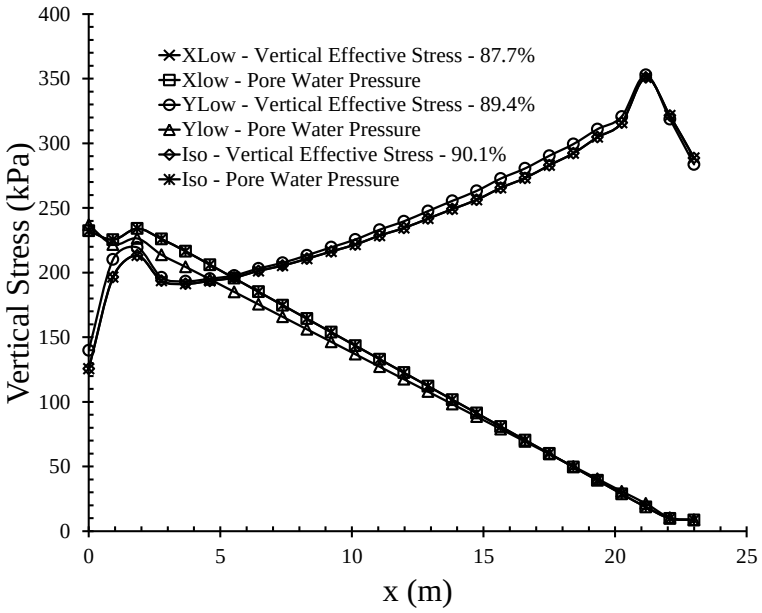

Figure 5.12: Comparisons between Anisotropic Low x Permeability and Low y Permeability in the Foundation with Isotropic Permeability Results

5.2.3 Factor of Safety Comparisons

In order to compare the results from the poromechanical anlayses to the classical gravity dam design method, some slight alterations were needed on the methodology described in Section 3.3. For the poromechanical analyses, the effective stress and pore water pressure were integrated with respect to x to get an effective downward and uplift force instead of working only with the total stress. These values were then used in the formulas outlined by Watermeyer (2006) to calculate the factor of safety against sliding and overturning (see Appendix A for more detail).

The factors of safety for the classical gravity dam design method, the finite element model with a deformable sandstone foundation, and the finite element model with enabled poromechanics can be found in Table 5.3 for three different contact friction angles. The poromechanical results can only be compared to the cases where uplift pressure distribution 2 was previously used, because there is no case without pore pressure and drainage systems are not considered. As is seen on the aforementioned table, all three values for each scenario are nearly identical. Including coupled solid skeletal deformations and porous media flow does not appreciably effect the factor of safety results calculated using only the classical method, verifying the ability to include such complexities in finite element modeling of gravity dams. Unlike the classical gravity dam design method, the finite element method has the advantage of being able to add other features. For example, anisotropic permeability models, like those discussed in Section 2.1.1, can be included in ABAQUS to account for a preferential flow direction. Using finite element methods, engineers are also able to increase the traction and pore pressure boundary conditions as functions of time to simulate flood conditions.

Table 5.3: Factor of Safety Analysis Results for Classical Design Method, Deformable Sandstone Foundation and Poromechanics

Friction Angle	$FS_{Sliding}$			$FS_{Overturning}$		
	Classical	Deformable	Poromech	Classical	Deformable	Poromech
30°	0.82	0.83	0.92	1.22	1.24	1.30
35°	0.99	1.00	1.03	1.22	1.22	1.25
40°	1.19	1.17	1.24	1.22	1.21	1.24

Chapter 6

Gravity Dam with High Permeability Sections Representing Cracks and Drains

6.1 Finite Element Development in ABAQUS

As an additional layer of complexity added to the poromechanical model described in Section 5, high permeability zones were directly modeled in ABAQUS to study the behavior of flow through cracks and drains in concrete gravity dam systems. Two sets of models were developed.

(1) A model of a crack along the dam-foundation contact with high permeability and directly meshed aperture.

(2) The same crack modeled with the inclusion of a high permeability drainage system near the heel of the gravity dam.

The crack and drain were both modeled as highly permeable porous media with linear elastic material properties. Material properties were chosen to loosely represent highly fractured concrete for the dam-foundation contact crack and a gravely soil for the drainage system. A list of material properties can be found in Table 6.1.

Figures 6.1 and 6.2 both show example ABAQUS/CAE renderings of the two different models, one with only a crack along the dam-foundation contact and one with a crack and vertical drainage system. The drainage system in Figure 6.2 was placed at 17.5 meters from the heel of the dam, which is approximately 75% of the total length of the gravity dam example from Watermeyer (2006). For both cases, with and without a vertical drainage system, four different crack lengths were investigated: a crack extending from the heel of the dam to the drainage system (denoted as

Table 6.1: Porous Media Material Properties

Material	Poisson's Ratio ν	Young's Modulus $E_{material}$ (GPa)	Density ρ (kg/m^3)	Permeability k (m/sec)	Initial Void Ratio e_0
Concrete	0.2	20.67	2396	1x10^{-12}	0.05
Sandstone	0.33	10.5	2000	1x10^{-10}	0.2
Crack	0.2	2.0	2000	1x10^{-2}	0.4
Drain	0.4	3.0	1400	1x10^{-2}	0.6

100L), a crack from the heel to three quarters of the distance to the drainage system (75L), and similar cracks to 50% and 25% the length to the drainage system (50L and 25L respectively). The same frictional contact model was used to describe the dam-foundation interface, but due to the addition of a base crack and drainage system, the interface was instead located along the bottom of the crack, which was meshed into the concrete dam and not the foundation, and through the vertical drainage system, which was created as two separate parts in ABAQUS/CAE. By breaking the drain into two pieces, the model assumes that the drainage system does not contribute to the resisting forces preventing sliding, other than the small area that develops frictional resistance, like a set of steel anchor bars would.

Applied tractions and boundary conditions were similar to those applied to the poromechanical gravity dam model described in Chapter 5, except an additional pore pressure boundary condition was applied to the top of the drainage system. This additional boundary condition was set to 0 Pa to simulate a drainage system open to the atmosphere, but can be easily adjusted to another value given appropriate information. Also similar to the model from Chapter 5, the ABAQUS analyses were run using the soils step under steady-state conditions with the gravity load applied first (over 0-1 pseudo-seconds) to insure a build-up of frictional resistance prior to applying to the pore pressure boundary conditions and tractions (over 1-2 pseudo-seconds).

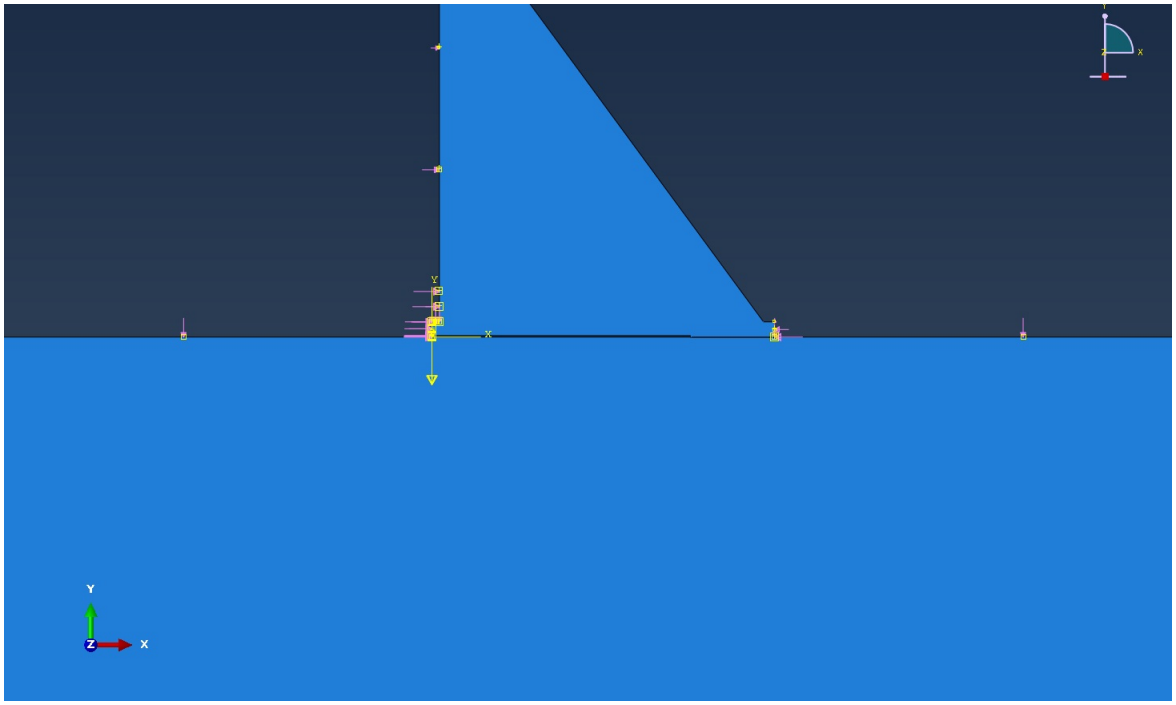

Figure 6.1: Zoomed in ABAQUS/CAE Rendering of the Geometry and Boundary Conditions for a Base Crack to 100L

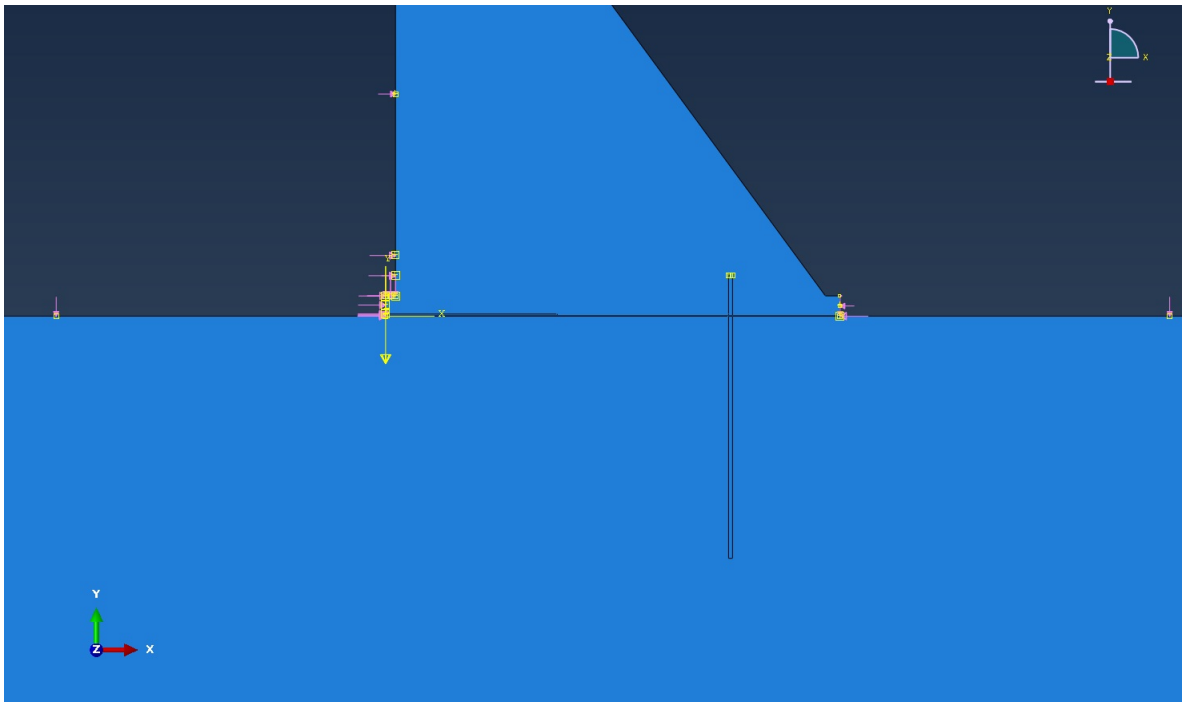

Figure 6.2: Zoomed in ABAQUS/CAE Rendering of the Geometry and Boundary Conditions for a Base Crack to 50L with a Vertical Drainage System

6.2 Finite Element Model Results

6.2.1 Crack Only

Figures 6.3 and 6.4 show ABAQUS finite element modeling results zoomed in around a high permeability crack extending 17.5 m along the dam-foundation contact. The scale of the coutour lines were altered to more clearly see the changes in the effective stress and pore water pressure solutions around the the base crack. Plots of the effective vertical stress, pore water pressure, and total stress distributions for the four considered crack lengths can be found on figures 6.5, 6.6, and 6.7. After comparing these Figures with results from the poromechanical analysis in the previous chapter (found on Figure 5.5), one can see that as the crack along the dam-foundation contact is shortened, the effective stress, total stress and pore water pressure results begin to approach the aforementioned poromechanical data. One can also see that at the end of each base crack, the effective stress solutions increase. The surrounding concrete and rock materials are approximately one order of magnitude stiffer than the crack material meaning at the same strain, they will experience higher stress, given the linear and isotropic elastic constitutive model used. However, despite the changes in the effective stress and pore water pressure distributions with changing length of a base crack, the total stress distributions remain relatively constant and similar to the poromechanical results in Chapter 5 and the deformable foundation results in Chapter 4, as seen compared on Figure 5.7. The applied loads and, especially, the self weight of the system have not changed from analysis to analysis; therefore, the total stress experienced by the dam-foundation contact has not changed either.

As expected, the higher permeability of the meshed crack relative to the concrete dam and sandstone foundation created a preferential flow path through the system altering the nearly linear pore pressure distribution found on Figure 5.5. As can be seen on Figure 6.6, for each given crack length, the pore pressure distribution was found to be constant over the length of the crack and linearly varying thereafter. As mentioned in Section 2.3.1, the classical dam design method generally assumes that some fraction of the full upstream reservoir head is applied over a crack in

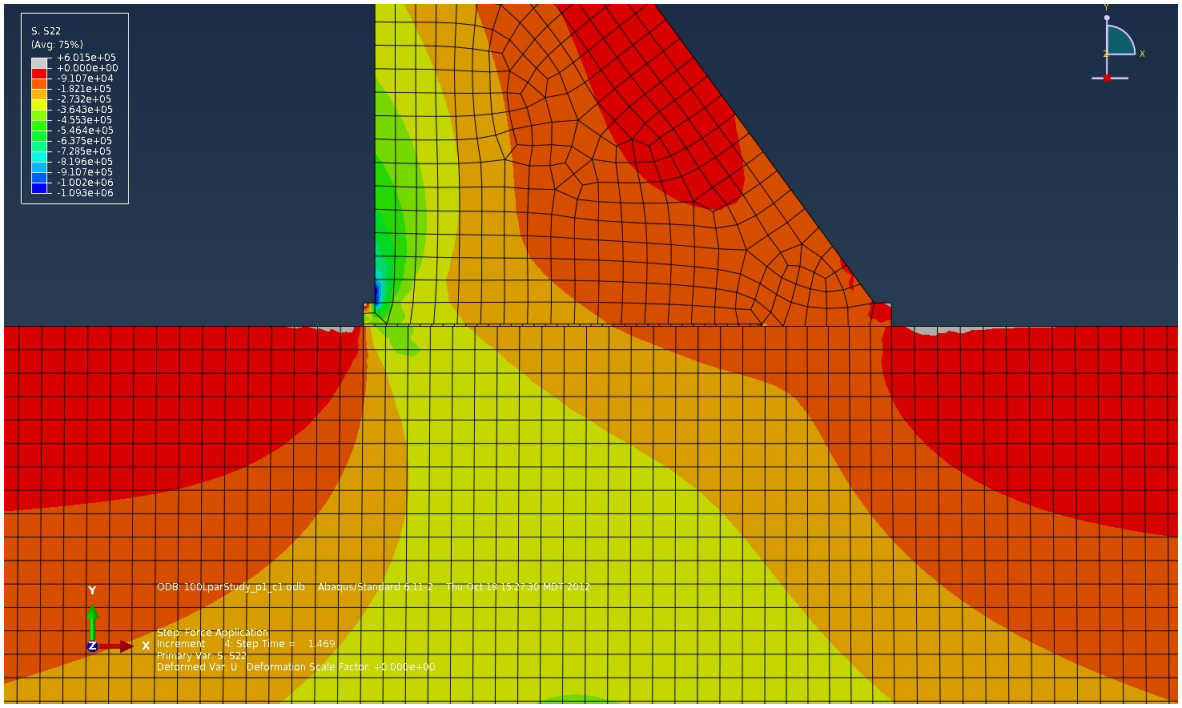

Figure 6.3: Deformed Geometry with Effective Stress Contours for a Crack to 100L

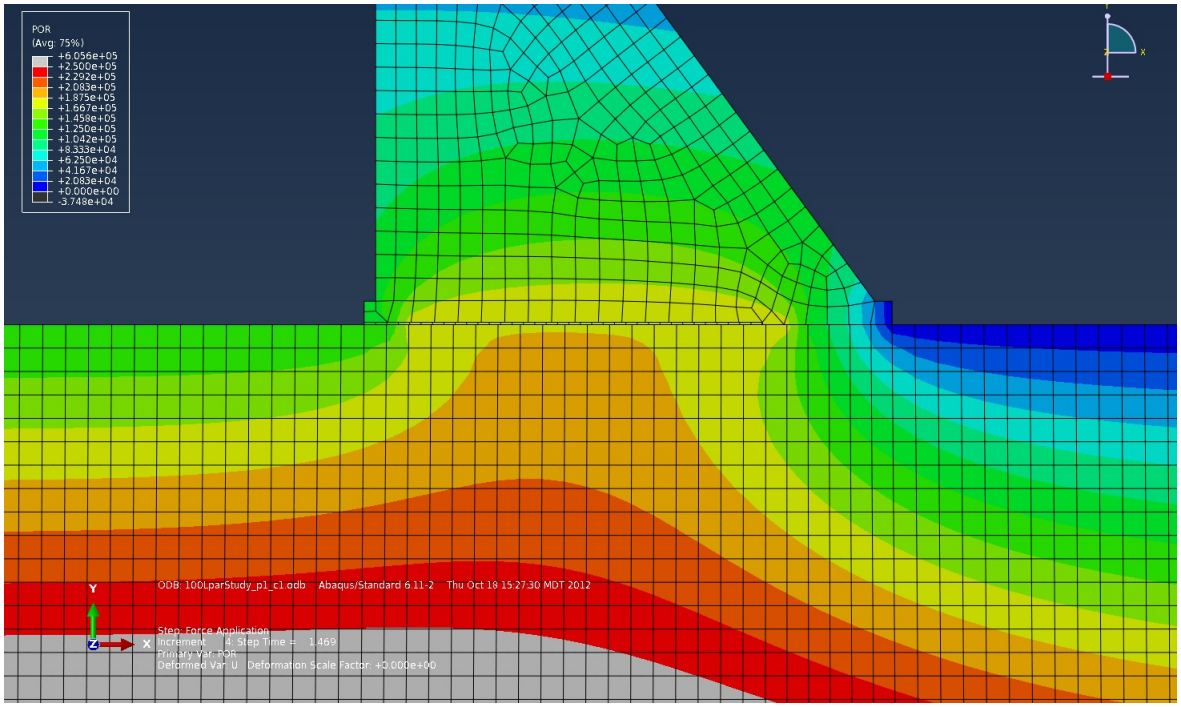

Figure 6.4: Deformed Geometry with Pore Water Pressure Contours for a Crack to 100L

the upstream face or along the dam-foundation contact. The finite element modeling results seem to further validate that claim. It should be noted that the reason shorter base cracks produced higher constant pore pressure distributions within the crack was a byproduct of how the boundary conditions were applied and not necessarily the physics behind the simulations. Because the pore water pressure boundary conditions and applied tractions were increased linearly over the final 1-2 pseudo-seconds, the percent complete values, found in the legends of Figures 6.5, 6.6, and 6.7 represent the faction of the tractions and pore pressure boundary conditions applied to the model prior to it failing to converge. As expected, the longer the base crack, the more unstable the system requiring less of the prescribed boundary conditions and pressures to cause failure.

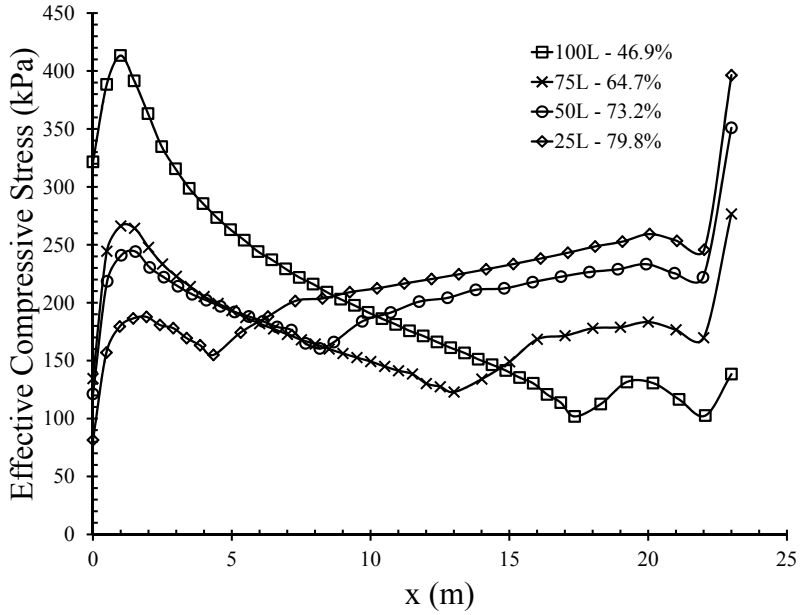

Figure 6.5: Vertical Effective Stress for Varying Crack Lengths Along the Dam-Foundation Contact

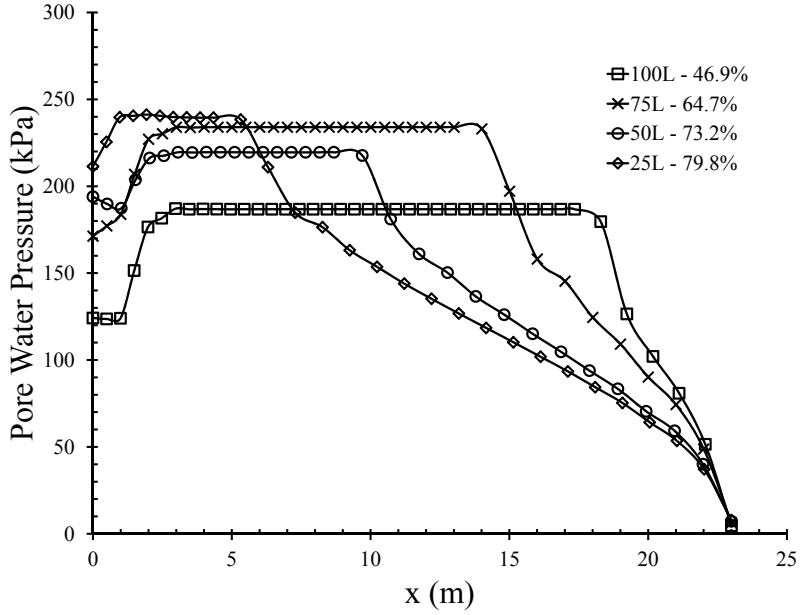

Figure 6.6: Pore Water Pressure for Varying Crack Lengths Along the Dam-Foundation Contact

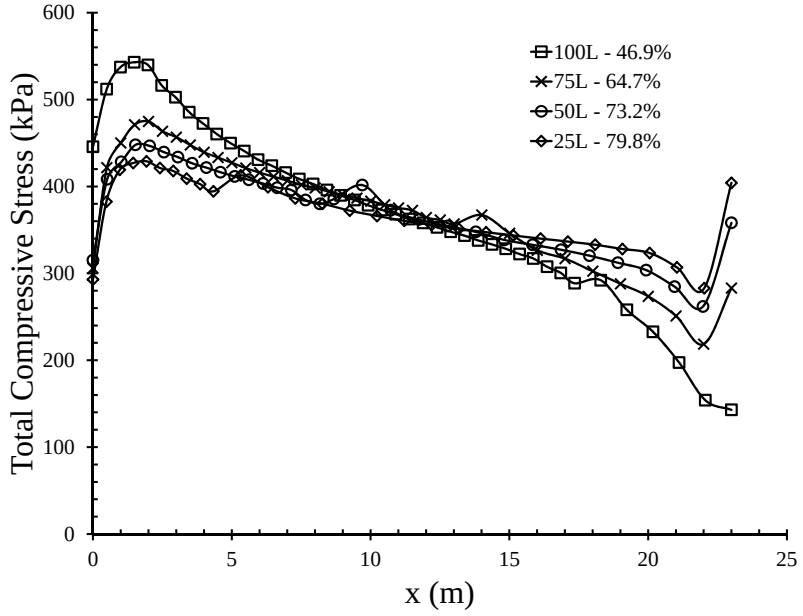

Figure 6.7: Total Stress for Varying Crack Lengths Along the Dam-Foundation Contact

6.2.2 Crack with Drain

In contrast to the previous section, the addition of a vertical drainage system significantly changed the effective stress and pore water pressure solutions, as can be seen on Figures 6.8 and 6.9. Figures 6.10, 6.11, and 6.12 show the effective stress, pore water pressure, and total stress solutions for different length base cracks with a drainage system. Like in the previous section, the total stress distributions remained relatively constant and similar to the results in previous chapters, but both the effective stress and pore water pressure solutions were different. The effective stress solutions, although altered by the different pore pressure solutions, display a similar trend to the results on Figure 6.5 in that the solutions increase after the end of the crack and, similarly, are lower within the drainage system. Like the crack, the drain's stiffness is an order of magnitude lower than the surrounding concrete and rock.

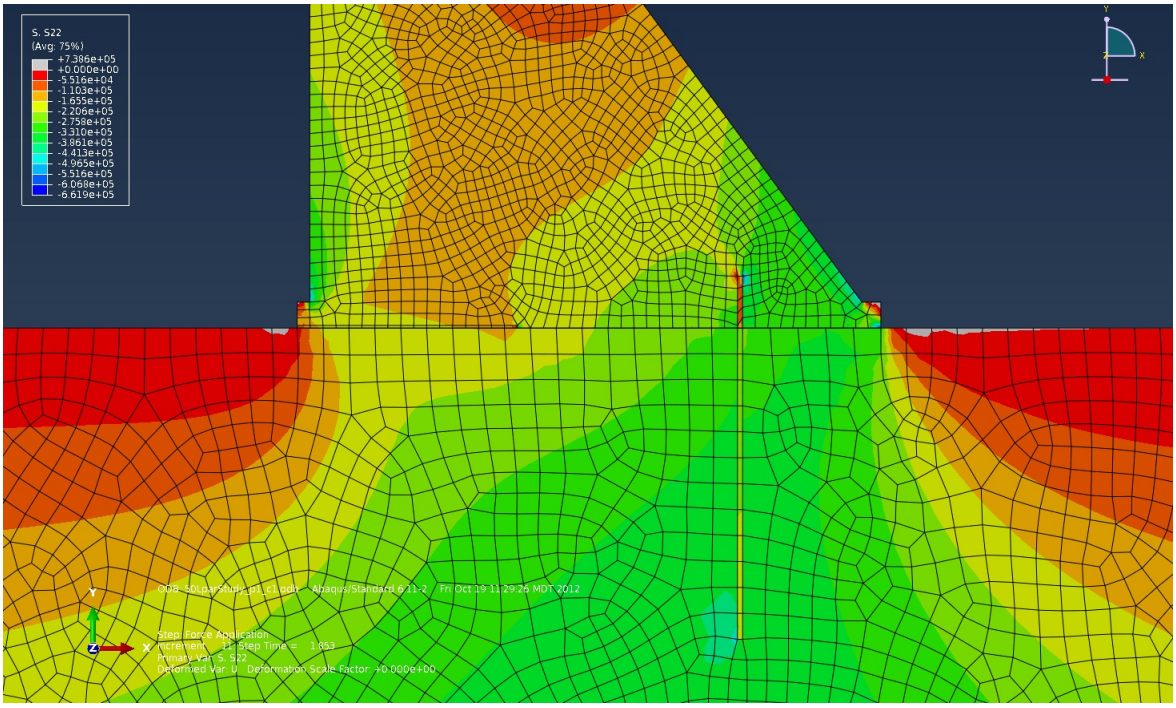

Figure 6.8: Deformed Geometry with Effective Stress Contours for a Crack to 50L Including a Drainage System

Like the models without drainage, the pore water distributions were still constant and relatively high within the crack, but with an added drainage system, they quickly dropped linearly to

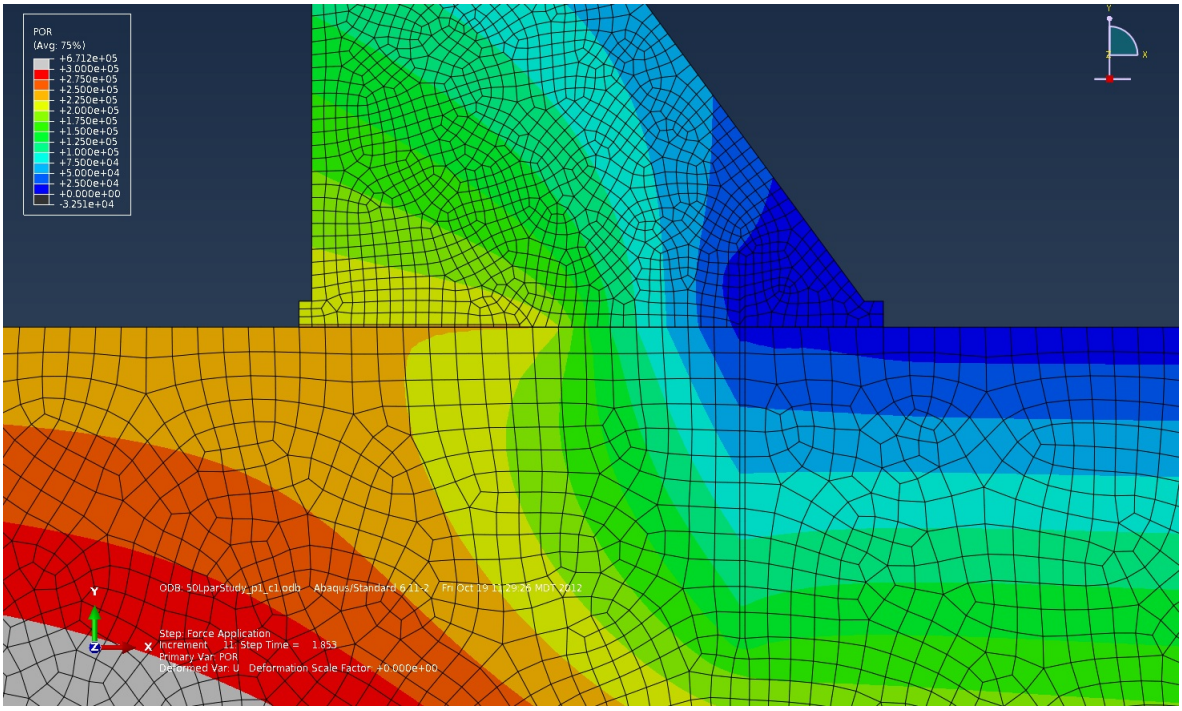

Figure 6.9: Deformed Geometry with Pore Water Pressure Contours for a Crack to 50L Including a Drainage System

near zero around the drain. Design of Small Dams suggests that the drain head be found by adding the downstream reservoir head to one third of the upstream reservoir head minus the downstream (Equation 1.1). For this dam geometry, the dam head calculated by Equation 1.1 is 94 kPa. The finite element modeling results show a drain head of approximately 10 kPa implying that in this circumstance the classical method is more conservative.

One notable exception to the constant pore water pressure distibution within the base crack was the 100L case. In this case, the base crack intersected the vertical drainage system creating a preferential flow path through the crack and into the drainage system. As a result, the pore pressure solution varied linearly from roughly the full upstream reservoir head at the face of the dam to approximately zero at the drain. Although this is an example of a fracture lowering the uplift pressure along the base of a gravity dam helping to stabilize the system, it is similar to the theoretical situation proposed by Terzaghi (1929) (see Section 2.1.1) where a fracture greatly increased the uplift pressure under a dam potentially causing failure. One advantage of the finite

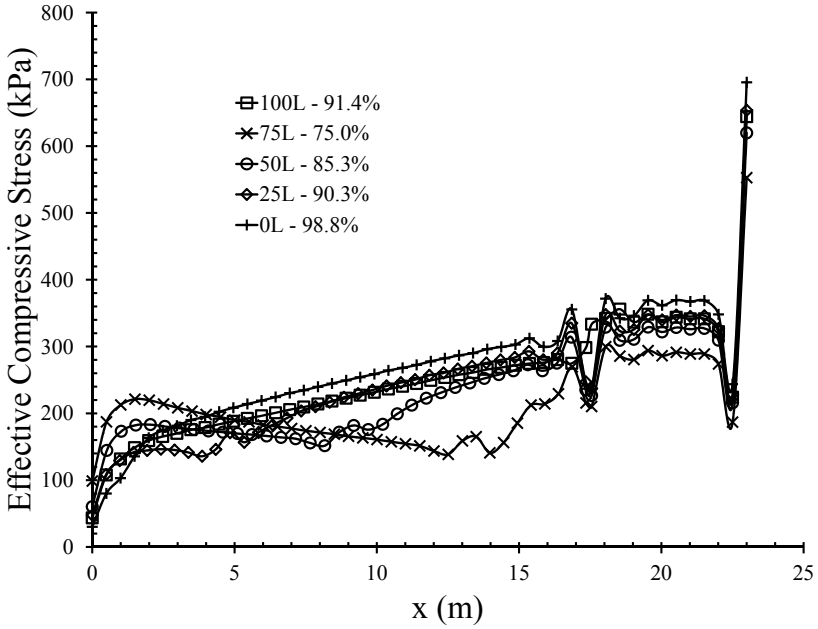

Figure 6.10: Vertical Effective Stress for Varying Crack Lengths with Drainage Along the Dam-Foundation Contact

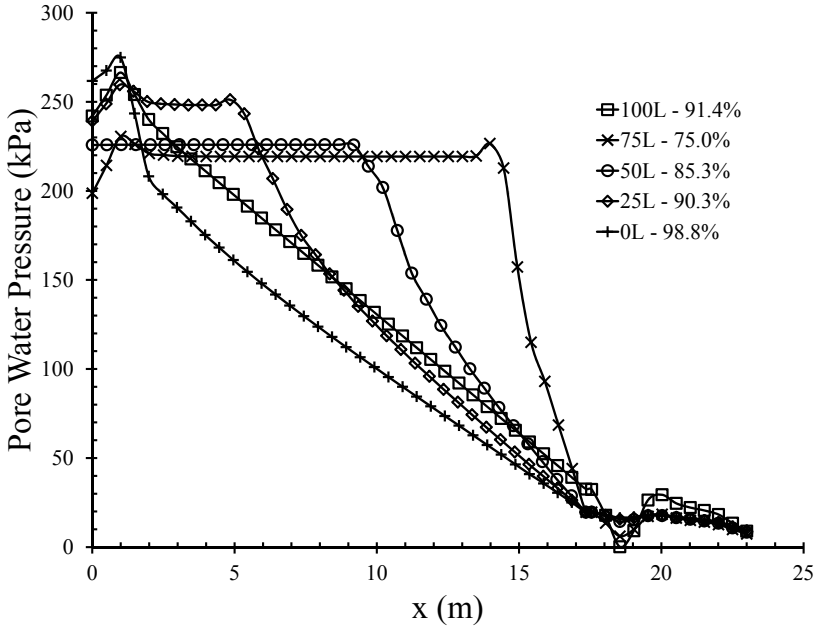

Figure 6.11: Pore Water Pressure for Varying Crack Lengths with Drainage Along the Dam-Foundation Contact

element method over the classical design method is that these types of cracks and rock joints can be modeled directly providing information about the effective stress, pore water pressure, and fluid flow in the system.

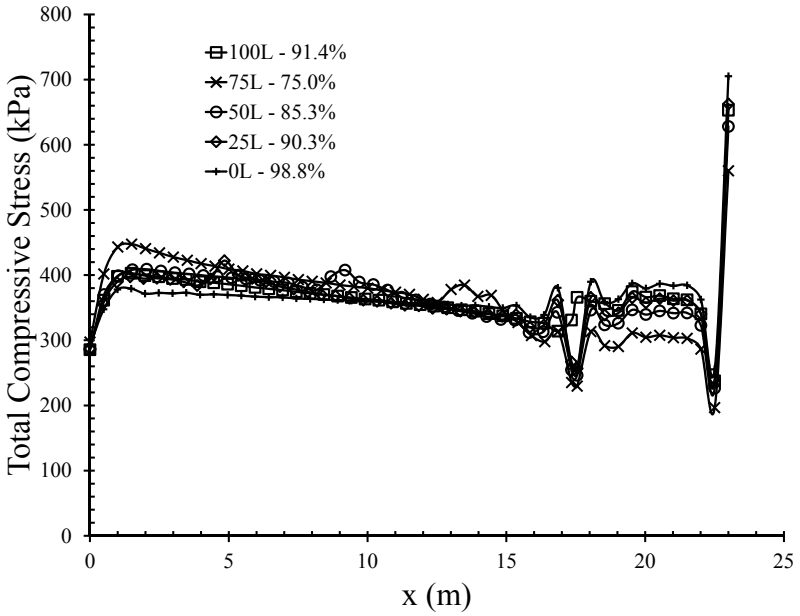

Figure 6.12: Total Stress for Varying Crack Lengths with Drainage Along the Dam-Foundation Contact

Just as the classical gravity dam design method assumes, and the finite element modeling results of previous chapters have shown, it is clear that by including a drainage system, the overall stablity of concrete gravity dams is increased. Figure 6.13 clearly shows a decrease in the pore water pressure solution from the models without drainage (solid lines) to the models with drainage (dashed lines). These results are clear even considering that in both of the cases with drainage a greater fraction of the pore pressure boundary conditions and tractions were applied to the models prior to failing to converge, which resulted in, on average, higher pore pressure distributions. Also, each percentage complete for the modeling results including drainage were nearly 10% greater than their corresponding percent complete without drainage further showing that drainage systems increased the system's stability. The notable exception is for the 100L case. In this scenario, the inclusion of a vertical drainage system increased the stability of the system by 37% for reasons

previously discussed.

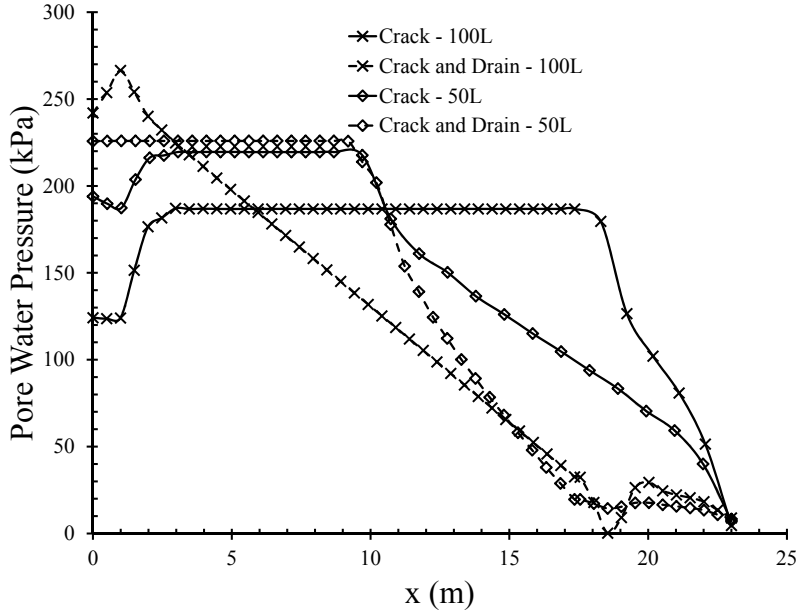

Figure 6.13: Comparison of the Pore Water Pressure with and without a Drainage System

6.2.3 Comparisons Between a Gravity Dam with Drainage System Near the Heel Versus Near the Toe of the Dam

In addition to simulating different length base cracks with and without drainage systems, a few finite element models were also developed to briefly assess the effect of drainage system location. Using the same material properties from previous models (see Table 6.1), two models each with a 2 meter long base crack were developed. The first model included a drainage system at 17.5 meters (the same location as in Section 6.2.2), and the second a drainage system at 4 meters. This provided two cases with different drainage system locations, one far downstream and the other near the dam heel, without the crack and drain intersecting creating a preferential flow path.

Contour plots of vertical effective stress and pore water pressure for downstream drainage case can be found on Figures 6.14 and 6.15. Similar plots for the upstream drainage case can be found on Figure 6.16 and 6.17. While the results for the downstream drainage case fit directly

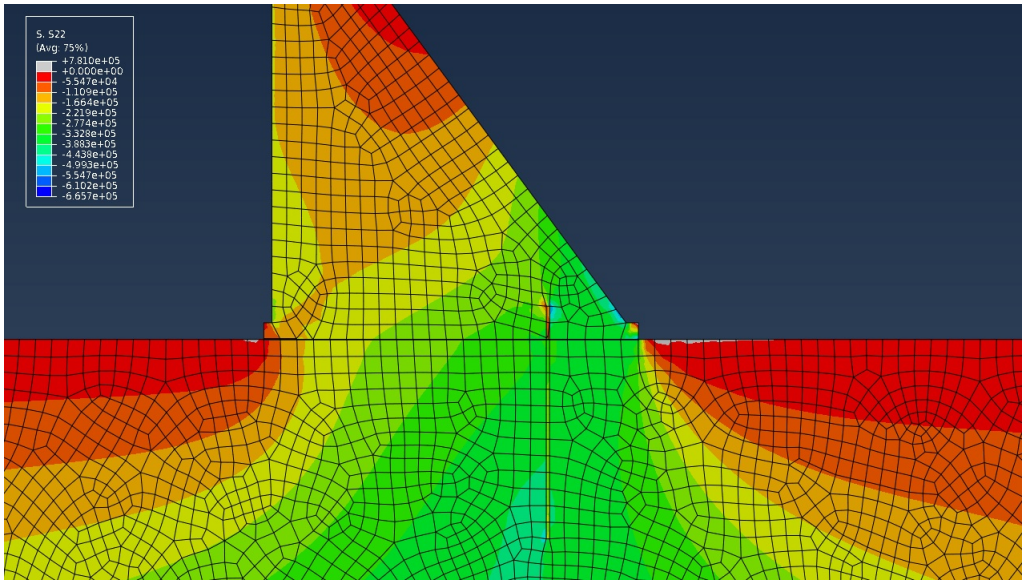

Figure 6.14: Dam with a Crack to 2 m and Drainage System Near the Toe of the Dam with Vertical Effective Stress Contours

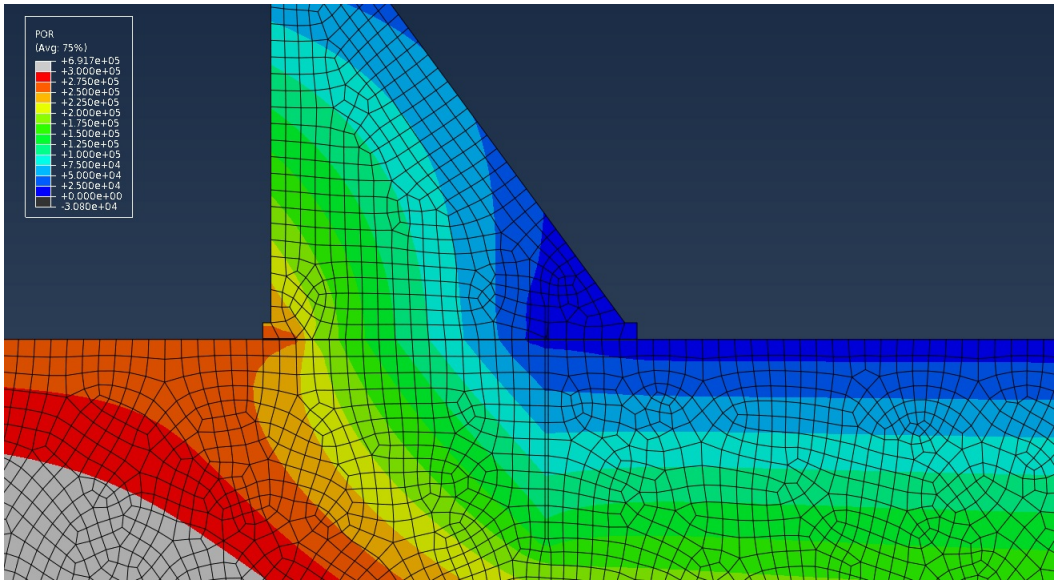

Figure 6.15: Dam with a Crack to 2 m and Drainage System Near the Toe of the Dam with Pore Water Pressure Contours

in with results presented in Section 6.2.2 (i.e. they are essentially a 12.5L case), results from the upstream drainage case depart from this mold significantly. In particular, Figure 6.17 shows a significant spike in pore pressure between the end of the base crack and drain and negative pore

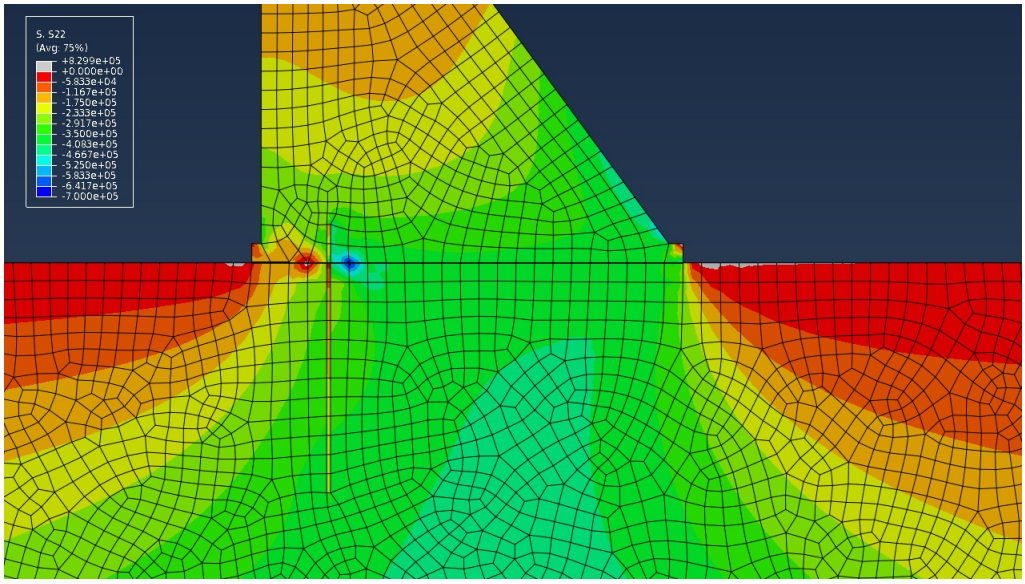

Figure 6.16: Dam with a Crack to 2 m and Drainage System Near the Heel of the Dam with Vertical Effective Stress Contours

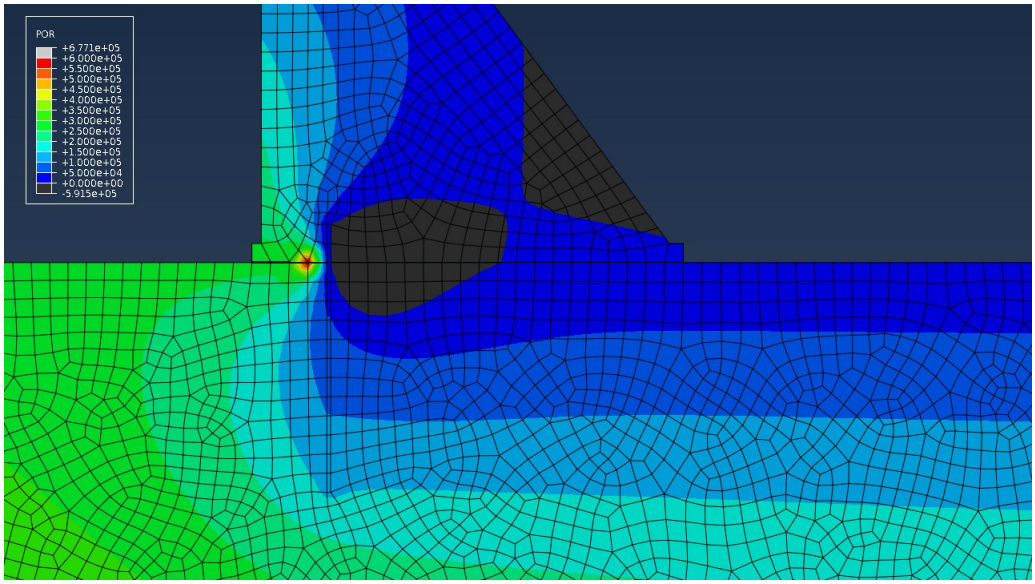

Figure 6.17: Dam with a Crack to 2 m and Drainage System Near the Heel of the Dam with Pore Water Pressure Contours

pressures immediately downstream of the drain.

Figure 6.18 is a plot comparing the vertical effective stress and pore water pressure distributions along the dam-foundation contact as well as the percent completion of the upstream and

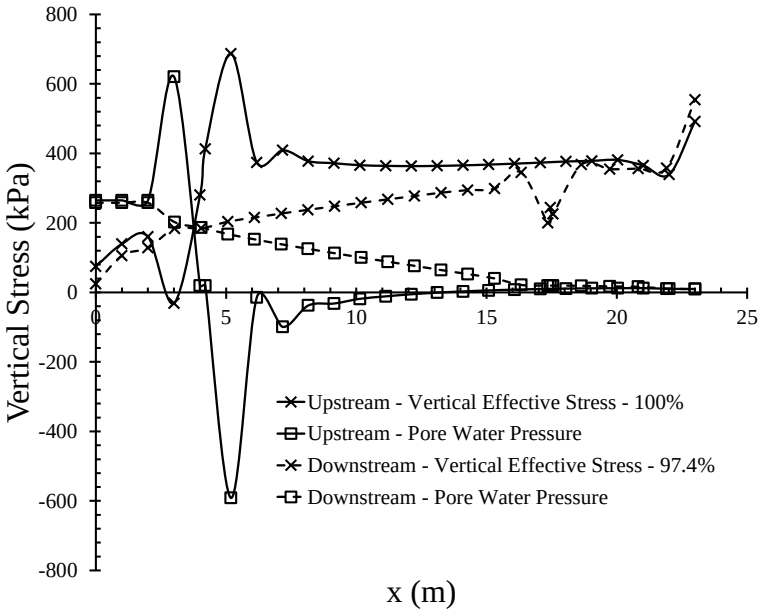

Figure 6.18: Comparison of the gravity Dam with a Crack to 2 m with an Upstream and Downstream Drainage System

downstream drainage cases. After inspection of the downstream case (dashed lines) and a comparison to the distributions on Figures 6.10 and 6.11, the results were essentially that of a 12.5L case. The percent completion value of 97.4% falls within the 0L and 25L cases, with completion values of 98.8% and 90.3%, respectively, and the overall shape of the distributions followed the same patterns as previous results. By moving the drain upstream, the overall pore water pressure distribution decreased resulting in negative pore water pressures over the majority of the dam-foundation contact. Without the water pressure to carry some of the self-weight of the dam, the overall vertical effective stress distribution increased to account for the increased load on the soil skeleton.

Finally, the upstream case also fully ran to completion meaning that moving the drainage system upstream increased the overall stability of the system. This is in agreement with results from the Volume 4 of the EPRI Reports (Chinnaswamy et al., 1990) where researchers found that drainage systems near the heel of a dam were more effective at reducing uplift pressures. However, because the finite element code CRFLOW is capable of including turbulence, it was also found that drains located too far upstream become less effective once the hydraulic gradient is high enough

to induce turbulence. Although ABAQUS has the capability to include turbulent flow, it was not implemented in this study. Figure 6.18 does seem to show a high hydraulic gradient induced in the upstream drain case, but is unclear whether turbulent flow would be induced in this circumstance.

6.2.4 Factor of Safety Comparisons

Following the same procedures outlined in Watermeyer (2006) and Section 3.3, a factor of safety analysis was performed using the classical gravity dam design method and the results of the finite element modeling. Just as in previous chapters, the stress distributions along the dam-foundation contact were integrated with respect to x to create vertical effective, shear, and uplift forces, and then input into the classical design method's formulas to calculated the "ABAQUS" factor of safeties. A full list of the factor of safeties against sliding including drainage and varying length base cracks as well as percent completion values from the finite element modeling can be found in Table 6.2.

Table 6.2: Factor of Safety Analysis for Classical Design Method and Finite Element Analysis for Models Including Base Cracks and Drainage Systems

Drain Location	Crack Length	$FS_{sliding}$		Percent Completion
		Classical	ABAQUS	
-	100L	0.46	0.48	0.47%
-	75L	0.55	0.56	0.65%
-	50L	0.64	0.66	0.73%
-	25L	0.73	0.74	0.79%
17.35m	100L	0.46	0.48	0.91%
17.35m	75L	0.66	0.69	0.75%
17.35m	50L	0.75	0.78	0.85%
17.35m	25L	0.83	0.85	0.90%
17.35m	0L	0.93	0.95	0.99%

Although all of the classical design method and finite element modeling yielded identical $FS_{sliding}$ values and these results were nearly identical to the percent completion before failure of the finite element analysis, there was a significant difference between the factor of safety results and percent completion for the 100L crack with a drain at 17.35m. The percent completion value

of 0.91% was almost twice the calculated factor of safeties (roughly 0.47). This was the same case described in detail earlier where the crack intersected the drainage system creating a preferential flow through the fracture and into the drain. It appeared that the geometry of the system was complicated enough to violate the assumptions of the classical design method rendering the factor of safety calculations, in the author's opinion, obsolete for this circumstance. As a result, effort was put into developing a different method of quantifying ultimate failure, as described in the following section.

6.3 User Material (UMAT) Failure Prediction

6.3.1 UMAT Ultimate Failure Calculation Development

The primary concern for developing an ultimate failure surface for a concrete gravity dam with flow through meshed fractures was the possibility of tension cracking causing the fractures to propagate. It was assumed that tensile failure was more likely to occur than crushing under heavy compression. It was also important, especially due to the relative importance of capturing the tensile behavior of concrete, to be able to directly account for cohesion and tensile strength. As a result, a standard Drucker-Prager yield surface was modified to include tension and compression caps and then implemented in an ABAQUS user material subroutine (UMAT) to calculate ultimate failure.

The modified Drucker-Prager ulitmate failure surface can be found in Equation 6.1.

$$f(\boldsymbol{\sigma}) = \| \mathbf{s} \| - \sqrt{F_{cap}^{\phi}} \sqrt{(A^{\phi} - B^{\phi} p)^2 - (A^{\phi} - B^{\phi} \chi)^2} \leq 0 \tag{6.1}$$

In this equation, the failure surface f is a function of stress $\boldsymbol{\sigma}$ on the material. The stress is split into its mean and norm of the deviatoric componenet, p and $\| \mathbf{s} \|$, and then inserted into the following set of equations that define the cap function (F_{cap}^{ϕ}), Heaviside function ($H(\kappa - I_1)$), and other functions that define the shape of the surface (A^{ϕ} and B^{ϕ}).

$$\mathbf{s} = \boldsymbol{\sigma} - p\mathbf{1}, \quad I_1 = tr(\boldsymbol{\sigma}) = \sigma_{ii} = 3p$$

$$A^{\phi} = \frac{2\sqrt{6}c\cos\phi}{3+\beta\sin\phi}, \quad B^{\phi} = \frac{2\sqrt{6}\sin\phi}{3+\beta\sin\phi}$$

$$F^{\phi}_{cap} = 1 - H(\kappa - I_1)\left(\frac{I_1 - \kappa}{X^{\phi}(\kappa) - \kappa}\right)^2, \quad 0 \le F^{\phi}_{cap} \le 1$$

$$H(\kappa - I_1) = (sign(\kappa - I_1) + 1)/2 = \begin{cases} 0 & I_1 > \kappa \\ 1 & I_1 \le \kappa \end{cases}$$

$$X^{\phi}(\kappa) = \kappa - R(A^{\phi} - B^{\phi}\kappa)$$

In these equations, χ defines the tensile cap and is analogous to tensile strength, c is the cohesion, ϕ is the friction angle, κ helps define the compression cap's location (through $X^{\phi}(\kappa)$), and R is a parameter defining the ellipticity the compression cap.

In order to determine appropriate values for various parameters and material properties, results from unconfined compression (UC) and unconfined tensile (UT) tests performed on concrete cylinders were taken and overlaid on a plot of the ultimate failure surface. Results of UC and UT tests from Wang et al. (2007), pg. 11-13, were used. For this application, the compressive strength of concrete (f'_c) was chosen to be 3000 psi (20.7 MPa), which is the lowest commercially used concrete strength. The rupture (tensile) strength (f'_r) was calculated using the formula in Wang et al. (2007), pg. 13, which is $f'_r = 0.62\sqrt{f'_c}$ (MPa) as recommended by the American Concrete Institute (ACI). UC and UT stress paths were then overlaid on a plot of the failure surface, and through iteration, material properties (primarily c, χ, and κ) were adjusted until the failure stresses (denoted by "X") lined up with the failure surface (see Figure 6.19). As previously mentioned, the primary goal was to characterize the tensile behavior of concrete to analyze potential fracture propagation, so only UC and UT stress paths were matched. The material parameters governing the compression cap were assumed large enough such that the concrete wouldn't likely fail due to large compressive stresses. As for the other material properties, the friction angle of concrete was assumed to be 20°, and R and β were assumed to be -1 and 10, respectively, to push the compression

cap sufficiently high. A full list of material properties can be found in Table 6.3. Also, it should be noted that plasticity was not evolved in this implementation; all of the material properties were kept constant.

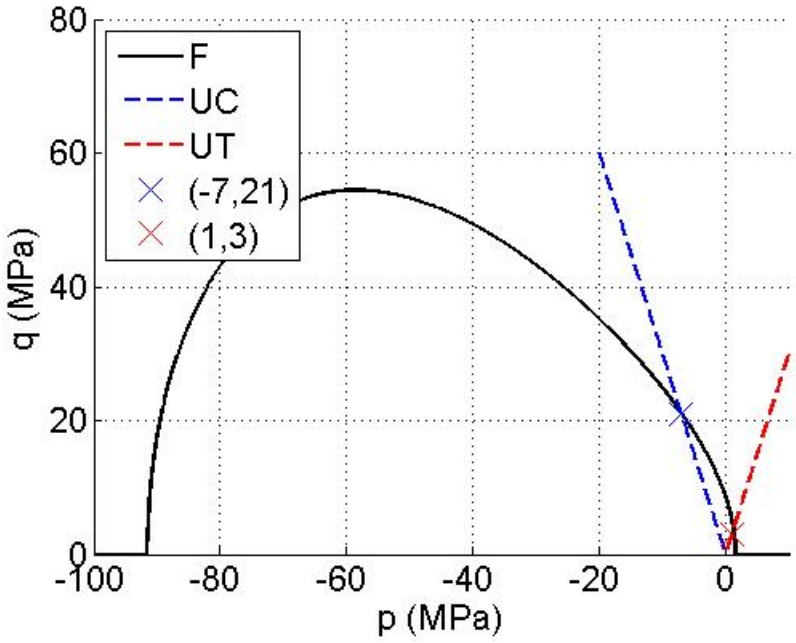

Figure 6.19: Modified Drucker-Prager Yield Surface with Concrete Unconfined Compression and Tension Stress Paths

An ABAQUS UMAT was then implemented such that at every time-step the stress solution generated by the analysis was taken and used to calculate the value of f, $\| \mathbf{s} \|$, and p at every integration point within the domain. Using these data, contour plots of f were rendered in the visualization module of ABAQUS. The concrete was considered to have reached failure if the value of f exceeded 0. Also, plots of the ultimate failure surface with stress paths at various integration points were generated in p-q space using MatLab. For reference, q is equal to $\sqrt{\frac{3}{2}} \| \mathbf{s} \|$, and a copy of the UMAT code can be found in Appendix B.

Table 6.3: Concrete Ultimate Failure Material Properties for ABAQUS UMAT

Parameter	Value
c	1.5x10^7 Pa
ϕ	20°
β	-1
κ	-2x10^6 Pa
R	10
χ	1.5x10^6 Pa

6.3.2 Results from UMAT Failure Prediction Analyses

To illustrate the use of the ultimate failure surface calculation, two previous examples were redone implementing the UMAT. The two examples that were re-purposed were the crack to 100L and the crack to 50L with a drainage system. Contour plot of f can be found on Figure 6.20 for the crack to 100L case and Figure 6.21 for the crack to 50L case. In both cases, the highest values of f (i.e. the values closest to the ulitmate failure surface) were generated in the concrete dam along the upstream side of the crack. Because the crack was less stiff than intact concrete (see Table 6.1), the dam carried more of the bending and self-weight stresses than the nearby crack causing the higher f values.

However, the f values calculated for both examples were significantly less than 0 implying that neither of the two circumstances were close to failure. Plots of the stress paths for the integration points with the highest values of f can be found on Figure 6.22 for the crack to 100L case and Figure 6.24 for the crack to 50L with drain case. In both of these figures, the stress path is small enough to be difficult to see; therefore, zoomed plots of the stress paths can be found on Figures 6.23 and 6.25, respectively. Both stress paths contain two components corresponding to the application of gravity over the 0-1 pseudo-seconds followed by the rest of the boundary conditions over 1-2 pseudo-seconds, which are represented by the abrupt change of direction. At first, the two integration points compress under the gravity load; the mean stress (p) goes slightly negative while the deviatoric stress (q) increases. With the application of the other boundary conditions, which were primarily horizontal forces due to the upstream reservoir, p and q decrease, and in the case of

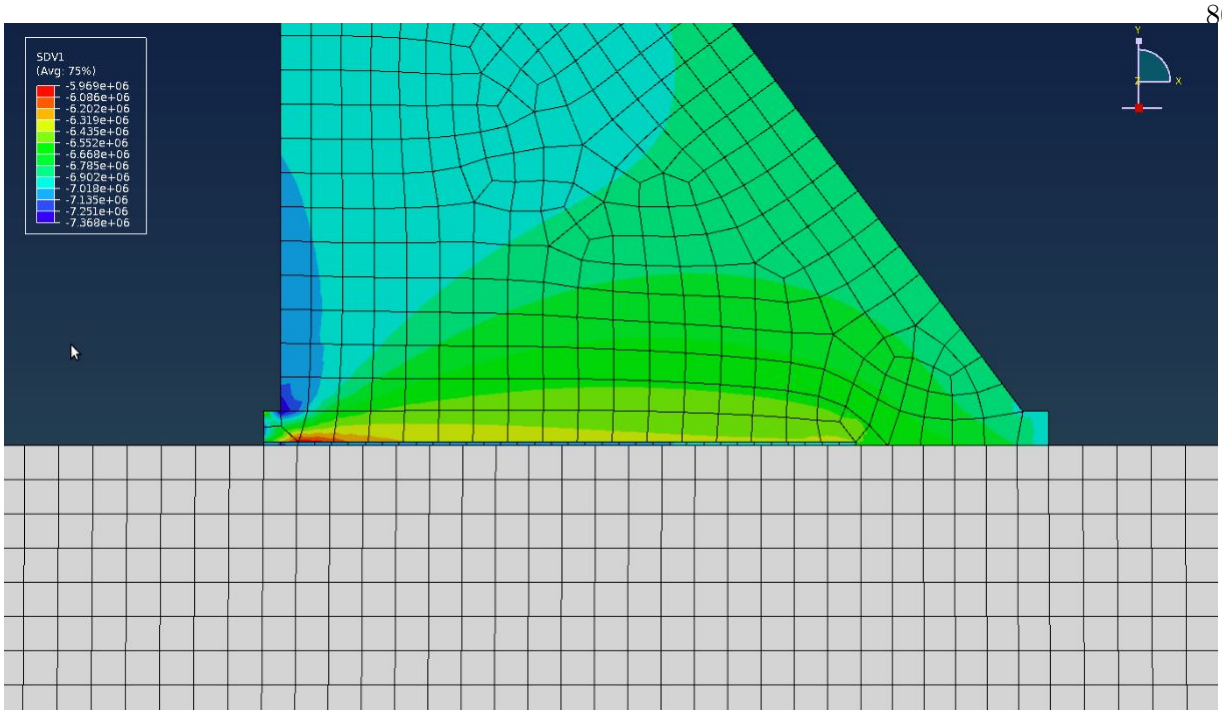

Figure 6.20: Deformed Geometry with Yield Function Contours for a Crack to 100L

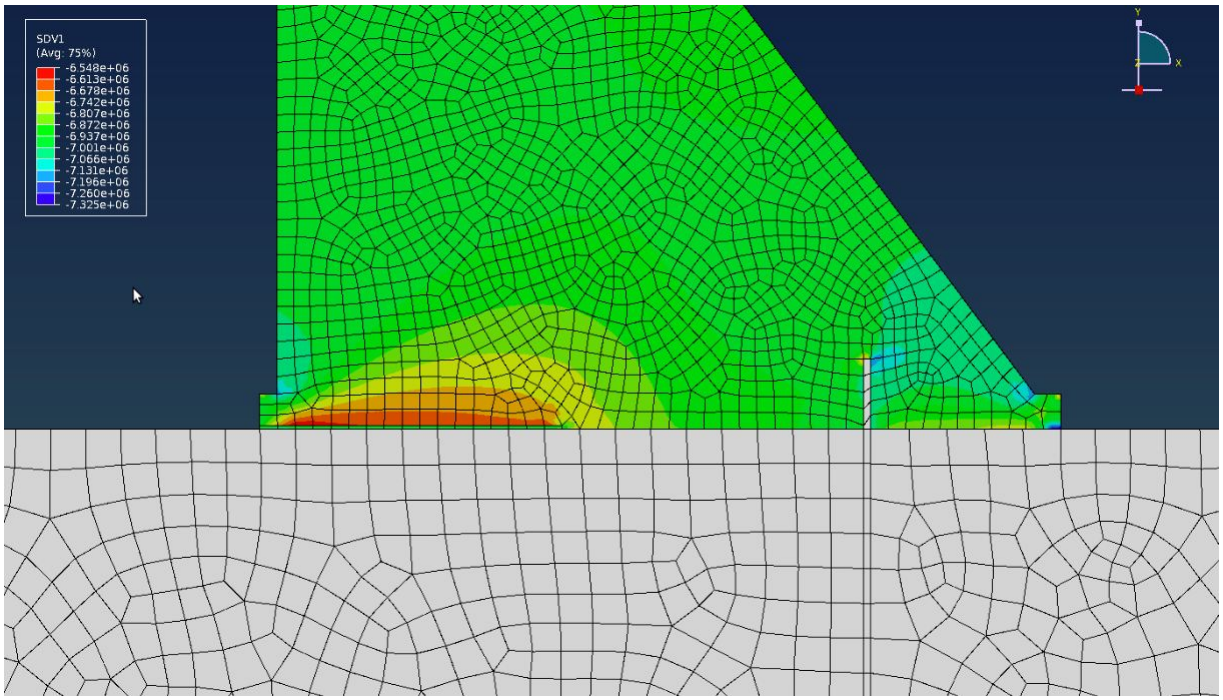

Figure 6.21: Deformed Geometry with Yield Function Contours for a Crack to 50L Including a Drainage System

the crack to 100L case, the mean stress even experiences some tension.

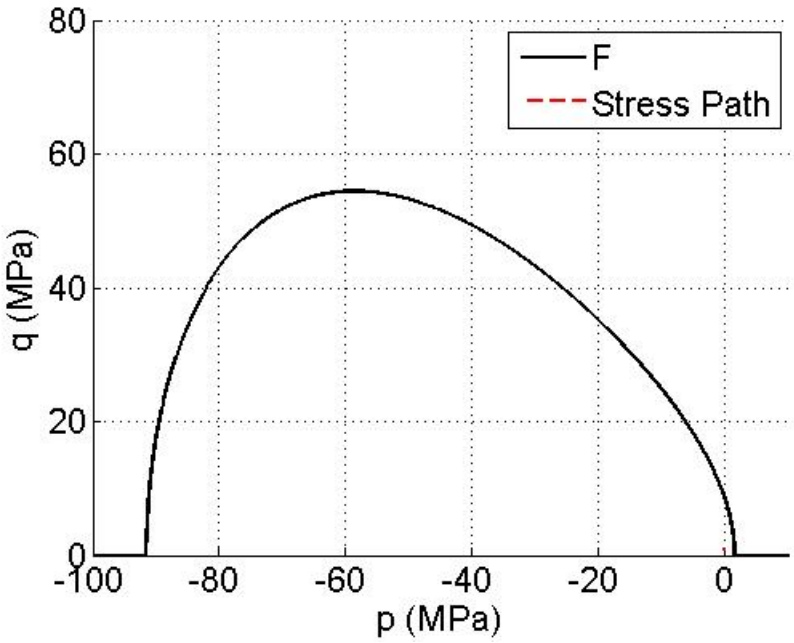

Figure 6.22: Concrete Yield Surface with Stress Path Closest to Yielding for a Crack to 100L

Yet overall, the generated stresses were not large enough to reach the ultimate failure surface in either case. This isn't necessarily surprising as concrete gravity dams are designed specifically to avoid crushing or fracturing. Although, the nearness of the stress paths to the tension cap do illustrate the need to protect against tension failures by using some reinforcement, such as steel rebar. In cases where a flood condition dramatically increases the stresses due to the upstream reservoir, it seems possible for sections of a gravity dam to reach the failure surface highlighting the potential usefulness of this analysis as a predictive tool. Also, it should be noted that there are many other consitutitive models other than a modified Drucker-Prager yield surface that can capture the behavoir of concrete, and that many more concrete tests would need to be considered, other than only unconfined compression and tension tests, in order to more fully characterize the ulitmate failure surface. This UMAT implementation should be considered then as a blueprint for the general methodology required to look at the characterizing the failure of a material, not as the best method for doing so.

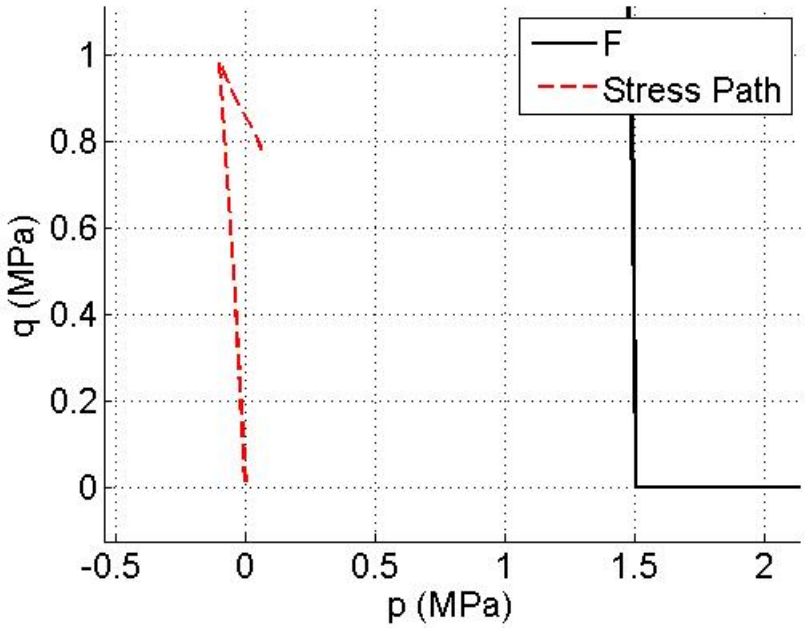

Figure 6.23: Concrete Yield Surface with Stress Path Closest to Yielding for a Crack to 100L (Rescaled)

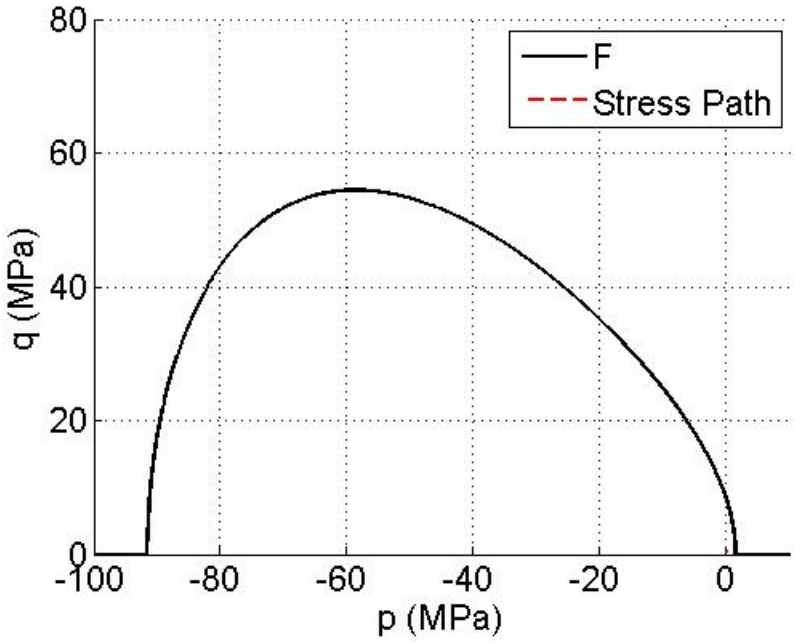

Figure 6.24: Concrete Yield Surface with Stress Path Closest to Yielding for a Crack to 50L Including a Drainage System

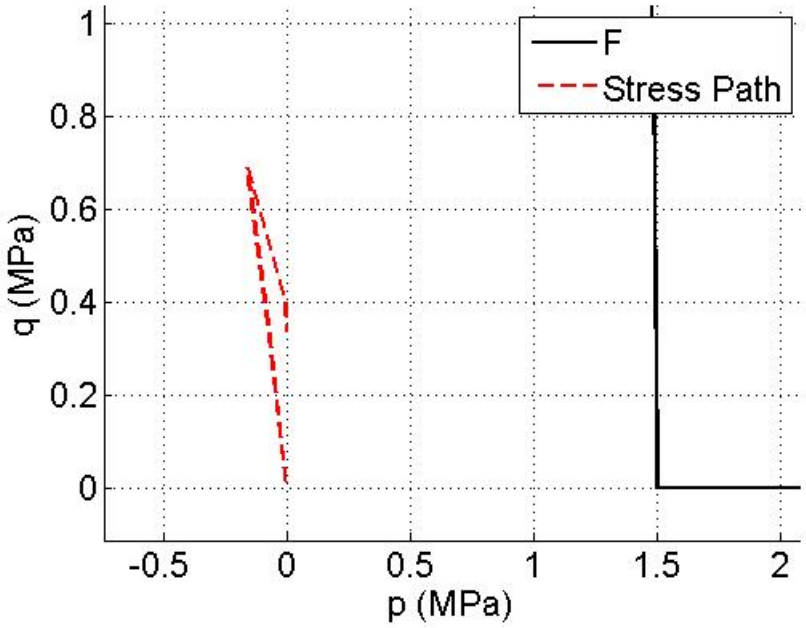

Figure 6.25: Concrete Yield Surface with Stress Path Closest to Yielding for a Crack to 50L Including a Drainage System (Rescaled)

Chapter 7

Simplified Gravity Dam with a Fracture Modeled using Poromechanical Cohesive Surface Elements in MatLab

7.1 Finite Element Model Development in MatLab

A simplified version of the concrete gravity dam system from Watermeyer (2006) was modeled using a finite element code, developed at the University of Colorado at Boulder by John Sweetser and Richard Regueiro (Sweetser, 2012), with fully pressure-sensitive, elasto-plastic, and poromechanical cohesive surface elements (CSEs) implemented. Figure 7.1 contains a diagram of the developed cohesive surface elements including information regarding the location of the nodes, degrees of freedom, and their general geometry. Other important featurues include the ability to include different tangential and normal permeabilities in the CSEs, and also the ability to set the initial aperture of the CSEs, which is in addition a function of the elastoplasticity. The code considers only small deformations and two-dimensional plane strain conditions at the present.

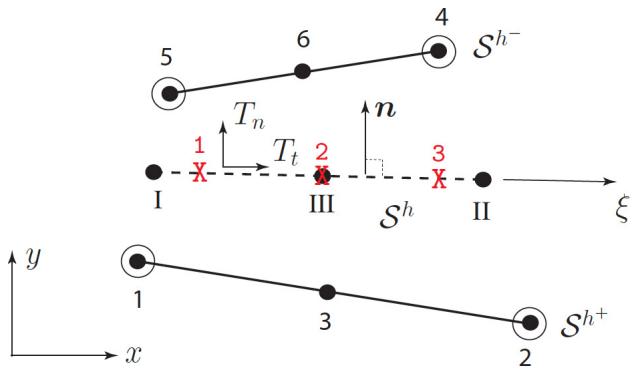

Figure 7.1: Diagram of a Pressure-sensitive, Poromechanical Cohesive Surface Element

Because the code is still in the development phase, the more complicated geometry of the previously used gravity dam system was simplified to ease the data analysis used to verify the code is working properly. In the model, a concrete gravity dam was founded on a deformable sandstone foundation with two CSEs as the dam-foundation contact. The full 14 element mesh and dam system geometry with labeled nodes and degrees of freedom can be found on Figure 7.2. For simplicity, the concrete dam was considered impermeable, although pore fluid flow was allowed through the foundation. Both the concrete dam and sandstone foundation were modeled as deformable solids using the same linear elastic material properties as previous chapters. Linear elastic and poromechanical material properties can be found in Table 6.1.

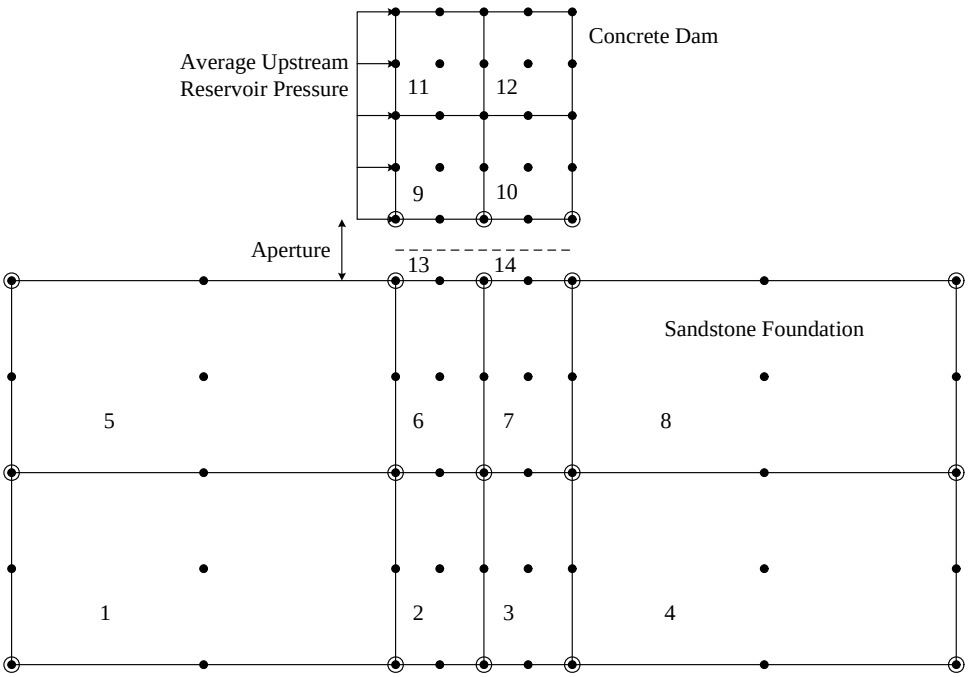

Figure 7.2: Finite Element Mesh for Poromechanical Cohesive Surface Elements in MatLab

In addition to simplifying the model's geometry and mesh, the applied tractions and boundary conditions were also streamlined. Instead of applying a hydrostatic traction along the upstream face of the dam, the traction was simplified to a uniform pressure distribution equal to the average upstream reservoir pressure. No other loads were applied to the system other than gravity. Like in previous models, pore water pressure boundary conditions were applied to the top of the foundation representing the full upstream and downstream reservoir pressures, but because the concrete gravity dam was considered impermeable, the only pore pressure boundary conditions prescribed on the gravity dam were at the heel and toe to inform the cohesive surface elements. Also similar to previous models, displacements were fixed in both x and y and no fluid flux boundary conditions were assumed along the bottom and both sides of the foundation.

As stated above, the constitutive model for the poromechanical cohesive surface elements has the capability to be fully elasto-plastic with a yield surface (7.1) and plastic potential function (7.2) defined by the following equations.

$$F = \sqrt{T_t^2 + (c - \chi \tan\phi)^2} - (c - T_n \tan\phi) \leq 0 \tag{7.1}$$

$$G = \sqrt{T_t^2 + (c - \chi \tan\psi)^2} - (c - T_n \tan\psi) \tag{7.2}$$

The yield surface and plastic potential function are evolved using the following traction-displacement relationship, described more fully by Yu (2010).

$$\chi = \chi_r + (\chi_p - \chi_r)\exp[-\alpha_\chi(\epsilon_n^p + \epsilon_s^p)]$$

$$c = c_r + (c_p - c_r)\exp[-\alpha_c(\epsilon_n^p + \epsilon_s^p)]$$

$$\tan\phi = \tan\phi_r + (\tan\phi_p - \tan\phi_r)\exp[-\alpha_\phi \epsilon_s^p]$$

$$\tan\psi = (\tan\psi_p)\exp[-\alpha_\psi \epsilon_s^p]$$

$$\epsilon_s^p = \int_0^t \dot{\epsilon}_s^p \mathrm{d}t, \quad \epsilon_n^p = \int_0^t \dot{\epsilon}_n^p \mathrm{d}t$$

$$\dot{\epsilon}_s^p = \frac{sign(T_n)}{G_f^{II}}\langle |T_t| - |T_n^* \tan\phi| \rangle \dot{u}_t^p, \quad \dot{\epsilon}_n^p = \frac{1}{G_f^I}\langle T_n \rangle \dot{u}_n^p$$

$$[[\dot{\mathbf{u}}^p]] = [\dot{u}_t^p, \dot{u}_n^p]^T, \quad \mathbf{T} = [T_n, T_t]^T$$

$$\langle T_n \rangle = \frac{(T_n + |T_n|)}{2}, \quad T_n^* = \frac{(T_n - |T_n|)}{2}$$

Essentially, the yield surface has a tension cap defined by cohesion (c) and tensile strength (χ). The compression side is defined by the frictional angle (ϕ) and dilation angle (ψ) for the yield surface and plastic potential function respectively. The four internal state variables are evolved using four rate softening material properties defined by α_c, α_χ, α_ϕ, and α_ψ. T_n and T_t are local traction vectors normal and tangential to the midline of a cohesive surface element. ϵ_s^p and ϵ_n^p are shear and normal plastic strains, and G_f^I and G_f^{II} are the mode I (tensile) and II (shear) fracture energies. Finally, $[[\dot{\mathbf{u}}^p]]$ is the rate of plastic jump displacement vector.

Table 7.1 contains a list of all the material properties used for the concrete dam, sandstone foundation and cohesive surface elements. As previously mentioned, the primary goal of the initial model was to assess the capabilities of new finite element code within the context of fractures in gravity dams and overall dam stability. Therefore, material property values were selected with enabling some of the novel features of the code, such as allowing plastic yielding within the CSEs, and not necessarily with absolute applicability to concrete fracture in mind. Similar to the user material implemented in Chapter 6, this implementation of the concrete gravity dam model was intentioned to be a blueprint for future work.

Finally, the finite element code was designed to run transiently requiring the loads to be

Table 7.1: Cohesive Surface Element and Bulk Element Material Properties

Material	Parameter	Value
Concrete	Young's Modulus (E)	20.67 GPa
	Poisson's Ratio (ν)	0.2
Sandstone	Young's Modulus (E)	10.5 GPa
	Poisson's Ratio (ν)	0.33
	Solid Real Mass Density (ρ^{sR})	2000 kg/m^3
	Fluid Real Mass Density (ρ^{fR})	1000 kg/m^3
	Solid Volume Fraction (n^{s0})	0.80
	Fluid Volume Fraction (n^{f0})	0.20
	Permeability (k)	1x10^{-7} m^2/(Pa·s)
CSE	Normal Stiffness (k_n)	10 GPa/m
	Tangential Stiffness (k_t)	10 GPa/m
	Permeability (k_{crack})	1x10^{-8} m^2/(Pa·s)
	Initial Friction Angle ($\phi_\circ$)	30°
	Initial Dilation Angle ($\psi_\circ$)	0°
	Initial Tensile Strength ($\chi_\circ$)	156 kPa
	Initial Cohesion ($c_\circ$)	90.5 kPa
	Mode I Fracture Energy (G_f^I)	10 kN/m
	Mode II Fracture Energy (G_f^{II})	10 kN/m
	Friction Angle Rate Softening Parameter (α_ϕ)	200
	Dilation Angle Rate Softening Parameter (α_ψ)	200
	Tensile Strength Rate Softening Parameter (α_χ)	900
	Cohesion Rate Softening Parameter (α_c)	900

incrementally ramped in order for the solution to converge. Just as with previous models, gravity was applied to the model first, but due to the transience, was held over a period of time after being fully ramped to allow the solutions to reach steady-state. After steady-state was reached, the horizontal traction was then ramped up over a long period of time and then held for longer until a second steady-state solution was reached. Over many iterations, it was determined that the following loading profile allowed for both steady-state conditions, the first under only gravity loading and the second including the upstream reservoir pressure, to fully develop.

(1) 0-10 seconds: linearly ramped gravity

(2) 11-310 seconds: held gravity and allowed solution to reach steady-state

(3) 311-410 seconds: continued holding gravity and linearly ramped horizontal traction

(4) 411-910 seconds: continued holding both gravity and the horizontal traction until solution reached steady-state

7.2 Finite Element Model Results

7.2.1 Simple Concrete Gravity Dam Model

Using the simplified geometry and loading conditions found on Figure 7.2 and the material properties listed in Table 7.1, the behavior of the cohesive surface elements were analyzed by plotting stress paths generated at integration points within the CSEs and by creating time histories of the CSE's aperture and pore water pressure. Figures 7.3, 7.4, and 7.5 are plots of the stress paths in T_n-T_t space including the plastic yield surface (see Equation 7.1) at three different integration points within the two cohesive surface elements. The location of the integration points can be found in Table 7.2, where the location is relative to the upstream corner of the dam-foundation contact and global element 13 is CSE 1 and global element 14 is CSE 2.

In all three stress paths, T_n was generally found to be negative indicating, as expected, compression under the self weight of the entire system. Also as expected, in both the element 1

Table 7.2: Location of the Integration Points within the Cohesive Surface Elements

CSE	Integration Point	Location
1	1	1.3 m
1	3	12.8 m
2	3	21.7 m

integration point 1 (EL1IP1) and element 1 integration point 3 (EL1IP3) cases, the application of the upstream reservoir traction caused a decrease in the compressive stress as the dam started to rotate; though, the decrease was sizably smaller in the EL1IP3 case. Due to its far downstream location, element 2 integration point 3 (EL2IP3) resisted the dam's rotation and the compressive stress increased with the application of the horizontal traction.

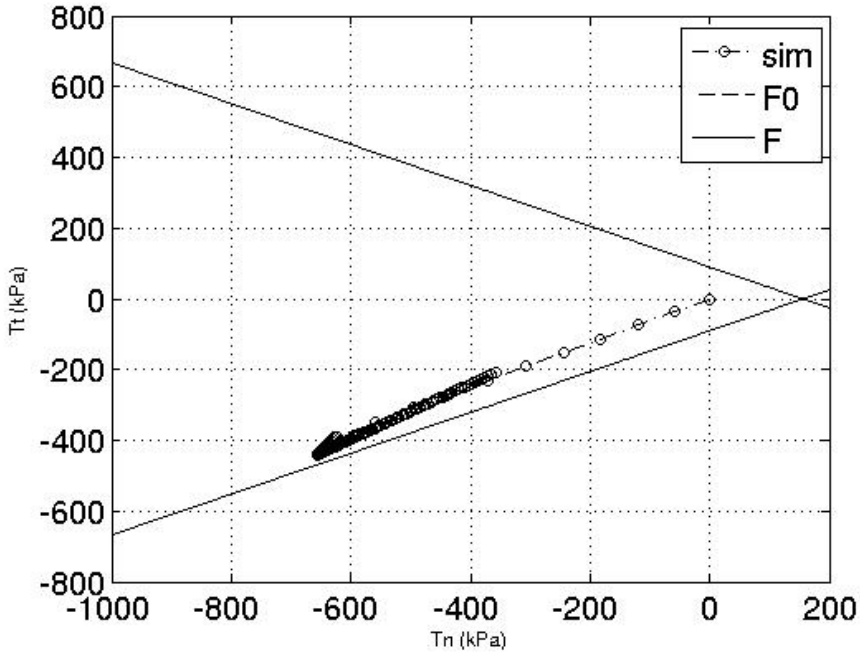

Figure 7.3: Yield Surface and Stress Path for CSE Element 1 Integration Point 1

The tangential traction (T_t) at an integration point is positive when the point is being forced downstream and negative when forced upstream. In the case of EL1IP1, the deformation of the foundation under gravity initially caused the integration point to be pulled upstream. Similarly, the deformation of the foundation forced EL2IP3 further downstream resulting in a positive T_t.

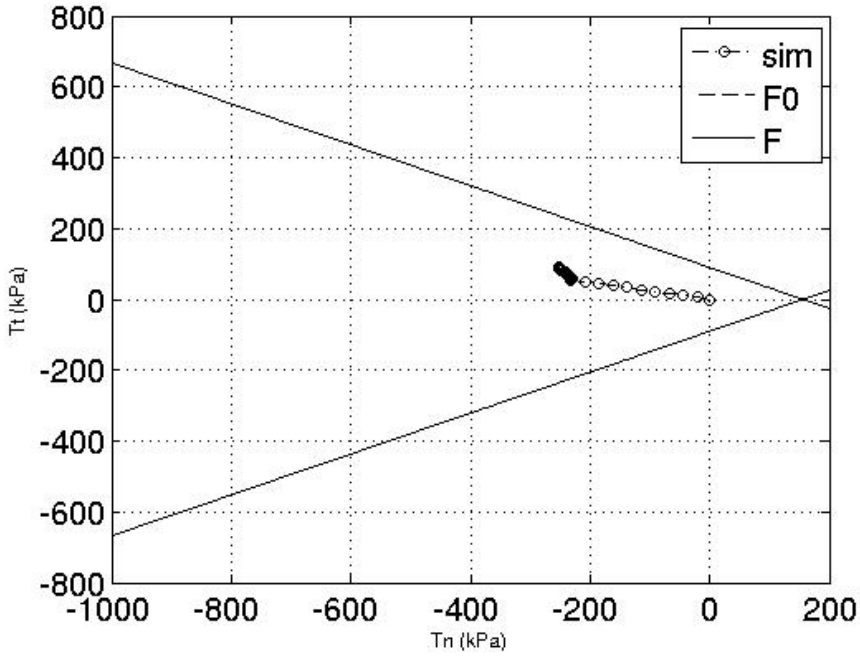

Figure 7.4: Yield Surface and Stress Path for CSE Element 1 Integration Point 3

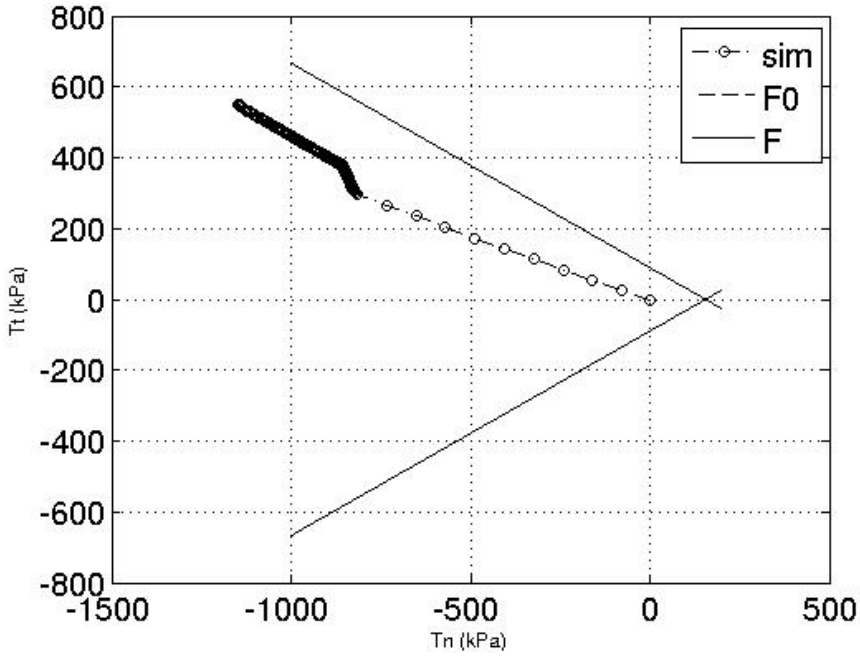

Figure 7.5: Yield Surface and Stress Path for CSE Element 2 Integration Point 3

With the application of the reservoir pressure, the additional stress pushed EL1IP1 downstream lowering the value of T_t. As for EL2IP3, the application of the horizontal traction similarly caused the integration point to be pushed further downstream.

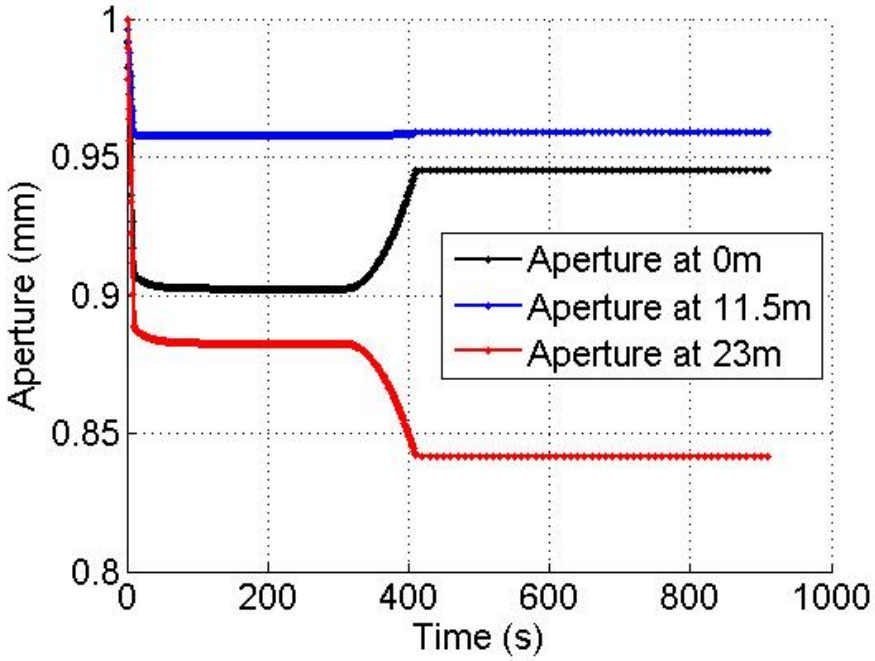

Figure 7.6: Time History of the CSEs Aperture Along the Dam-Foundation Contact

Figures 7.6 and 7.6 display the aperture of the CSEs and pore water pressure with time. The affect of the loading profile can be clearly seen on Figure 7.6 where the apertures change abruptly with each new loading stage. In this case, the initial aperture was set to 1 mm along the entirety of both CSEs, and under gravity, all of the apertures decreased. Also as expected, with the application of the horizontal loads, the upstream side of crack slightly reopened and the downstream side closed further with the rotation of the dam. As for the pore water pressure generation, both of the CSE nodes (the red and dotted green lines at a depth of 0 m) recorded the same pore pressures. They also did not consolidate like the pore water pressures at 25 m and 50 m into the foundation.

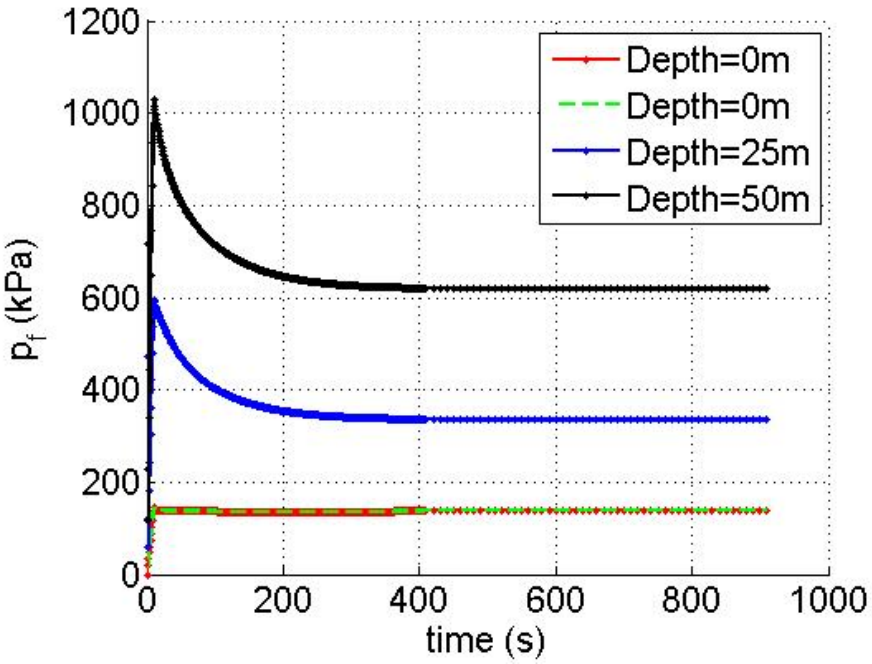

Figure 7.7: Time History of the Pore Water Pressure with Depth Through the Midpoint of the CSEs and Foundation

7.2.2 Gravity Dam Model with Higher Upstream Pressure to Induce Yielding

One important feature of the cohesive surface element formulation is that the constitutive relationship is allowed to evolve plastically. In order to demonstrate this feature, ten times the original horizontal traction was applied to the gravity dam such that the CSEs would yield. Figures 7.8, 7.9, and 7.10 are plots of the stress paths for EL1IP1, EL1IP3, and EL2IP3 in T_n-T_t space similar to the three plots in the previous section. Each of the stress paths follow the same general shape as those on Figures 7.3, 7.4, and 7.5, but in these cases, the CSEs yielded. For example, EL1IP3 experienced a softening of the friction angle, as can be seen by the relative location of the initial yield surface ($F_\circ$) and the final yield surface (F).

However, the yielding of the CSEs caused the finite element model to not run to completion. This can be seen on Figures 7.11 and 7.12 in that the aperture and pore water pressure solutions stop at around 360 seconds. Prior to failure, the results seemed to be tracing similar paths to the results of the previous section, but the inability to converge cut the solutions short. The code

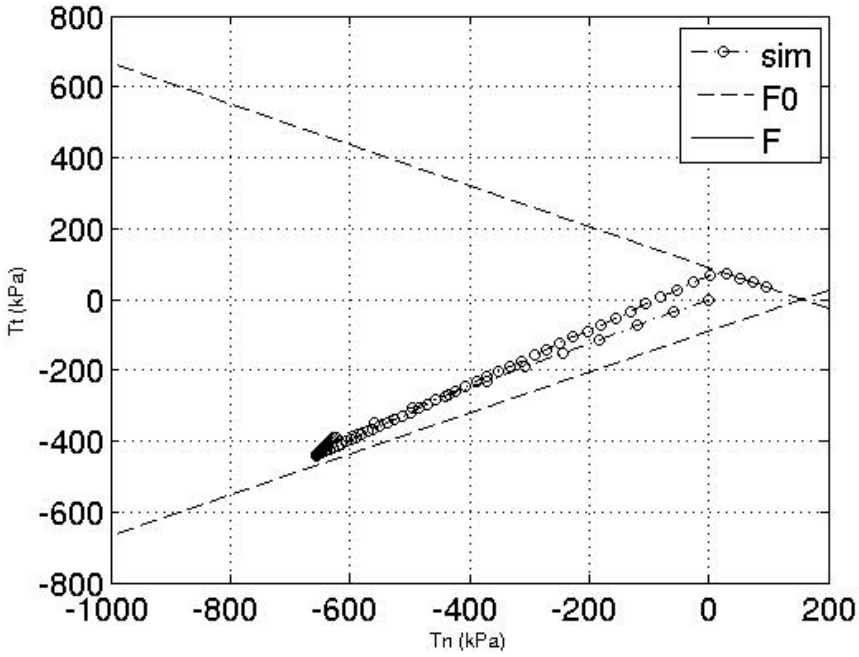

Figure 7.8: Yield Surface and Stress Path for CSE Element 1 Integration Point 1 Under a Higher Upstream Pressure

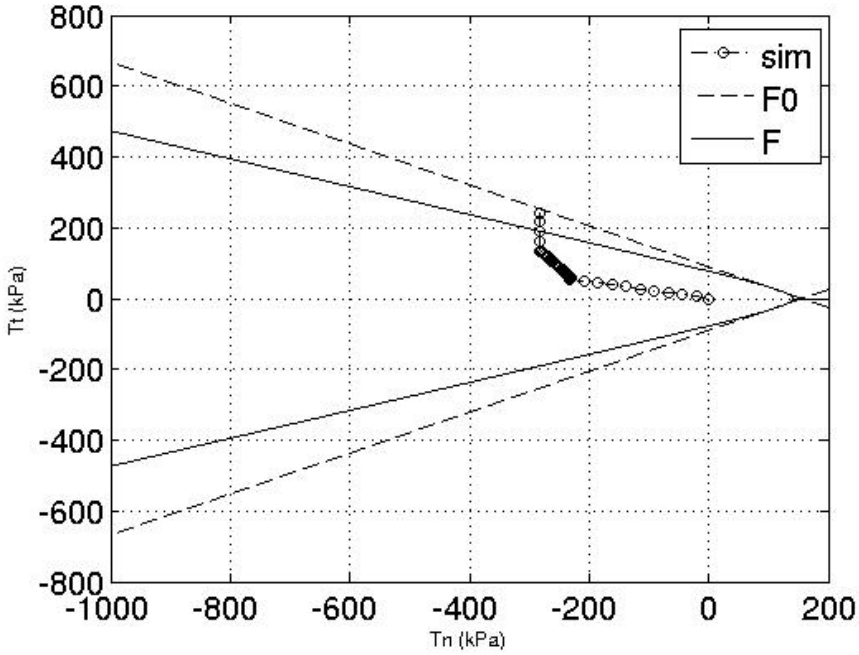

Figure 7.9: Yield Surface and Stress Path for CSE Element 1 Integration Point 3 Under a Higher Upstream Pressure

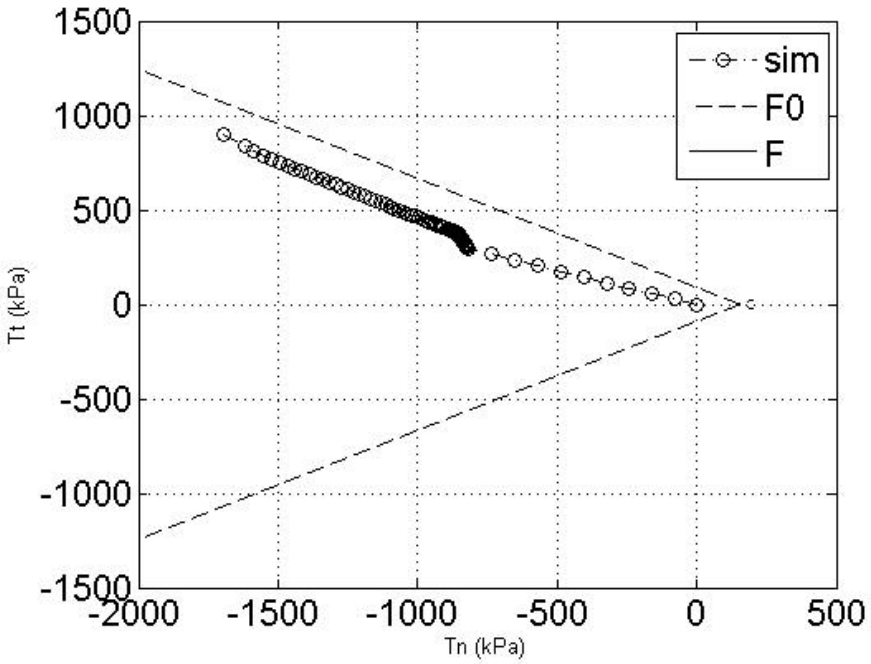

Figure 7.10: Yield Surface and Stress Path for CSE Element 2 Integration Point 3 Under a Higher Upstream Pressure

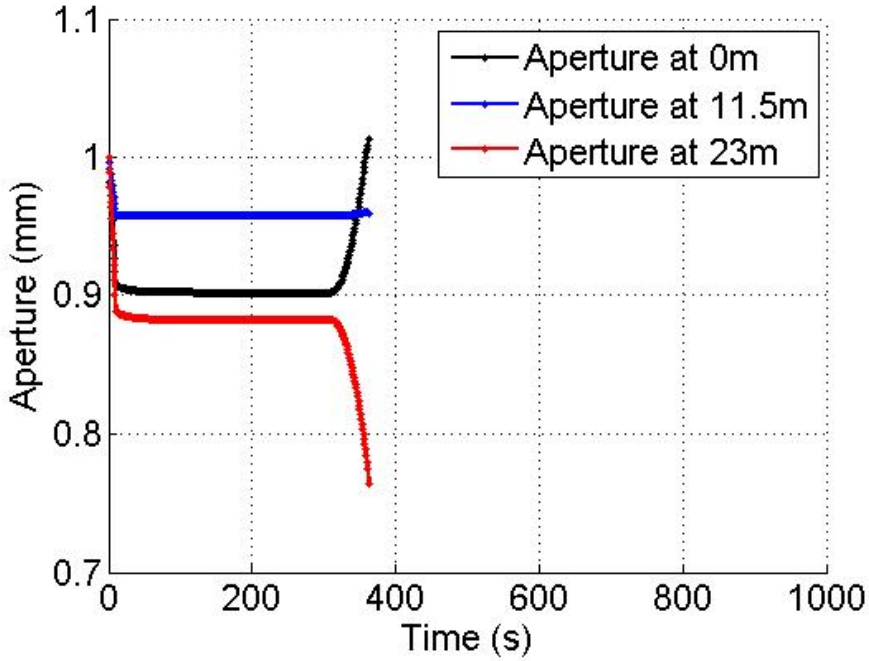

Figure 7.11: Time History of the CSEs Aperture Along the Dam-Foundation Contact for the Higher Upstream Pressure

is unable to track the stress-displacement curve during plastic softening, because the analysis is currently stress controlled. The result is convergence issues. To ameliorate the problem, an arc length procedure would track the stress-displacement curve helping the code run to completion.

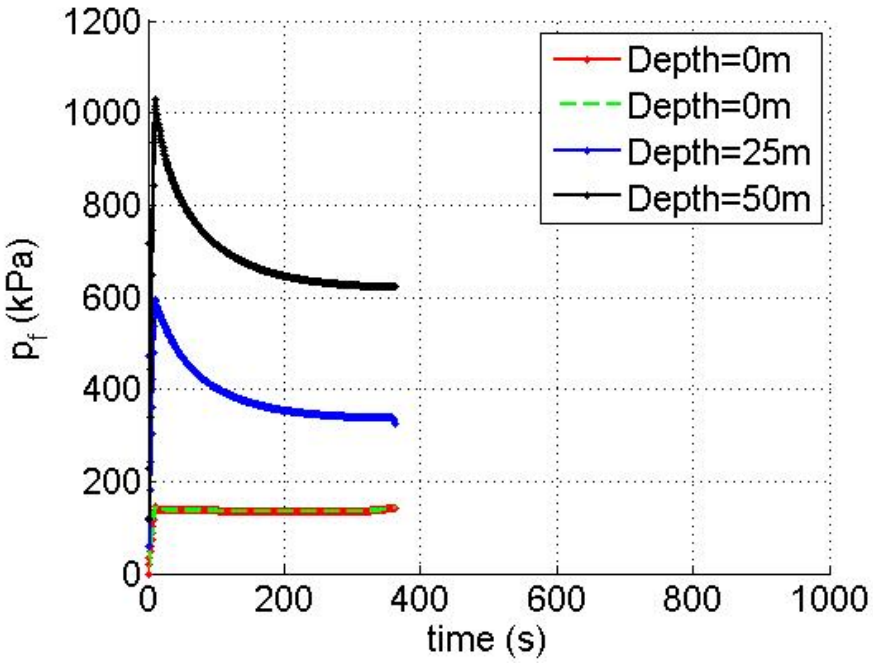

Figure 7.12: Time History of the Pore Water Pressure with Depth Through the Midpoint of the CSEs and Foundation for the Higher Upstream Pressure

7.2.3 Effect of Initial Crack Aperture on Gravity Dam Stability

To begin studying the effect of aperture on the response of the CSEs, three different initial apertures were set (0 m, 1 cm and 1 m) and the finite element code was run using the same larger applied horizontal traction as the previous section. The aperture and pore water pressure time histories for each simulation were then plotted. Figures 7.13 and 7.14 show the results given an initial aperture of 0 mm, Figures 7.15 and 7.16 an aperture of 1 cm, and Figures 7.17 and 7.18 an aperture of 1 m.

Comparisons of all three aperture plots show that despite the difference in initial aperture, the time histories were all the same. The solution failed to converge at the same point and the

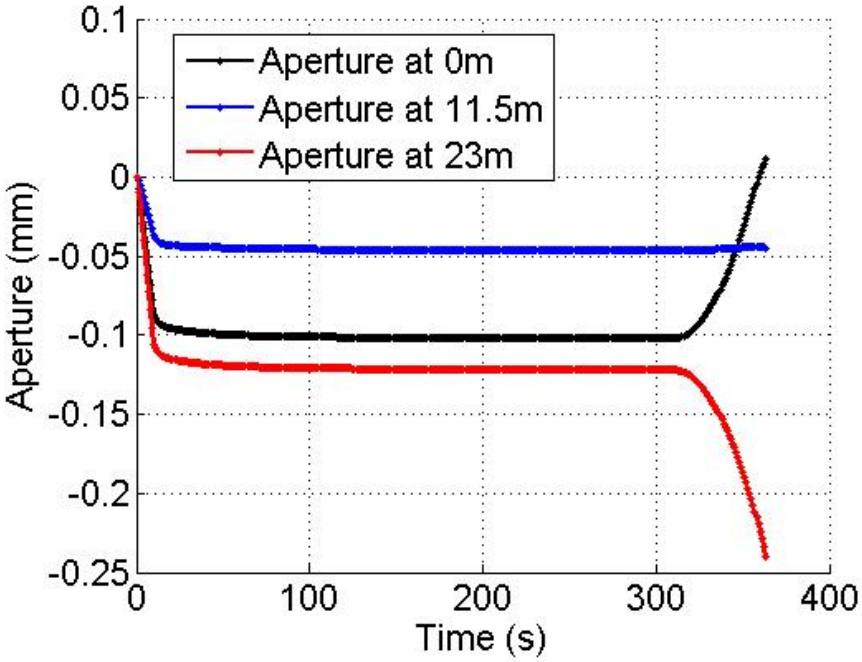

Figure 7.13: Time History of the CSEs Aperture Along the Dam-Foundation Contact for the Higher Upstream Pressure and the Initial Aperture = 0m

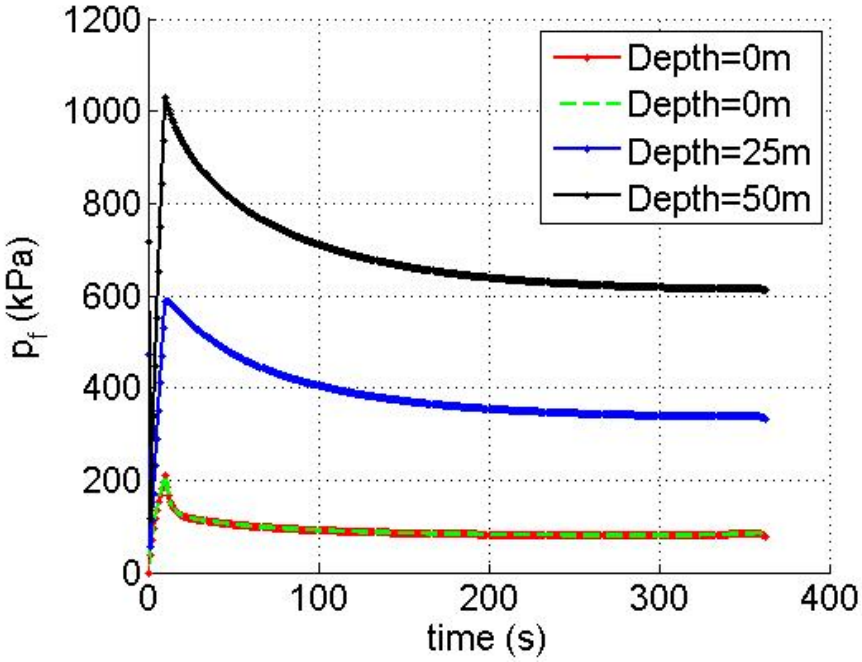

Figure 7.14: Time History of the Pore Water Pressure with Depth Through the Midpoint of the CSEs and Foundation for the Higher Upstream Pressure and the Initial Aperture = 0m

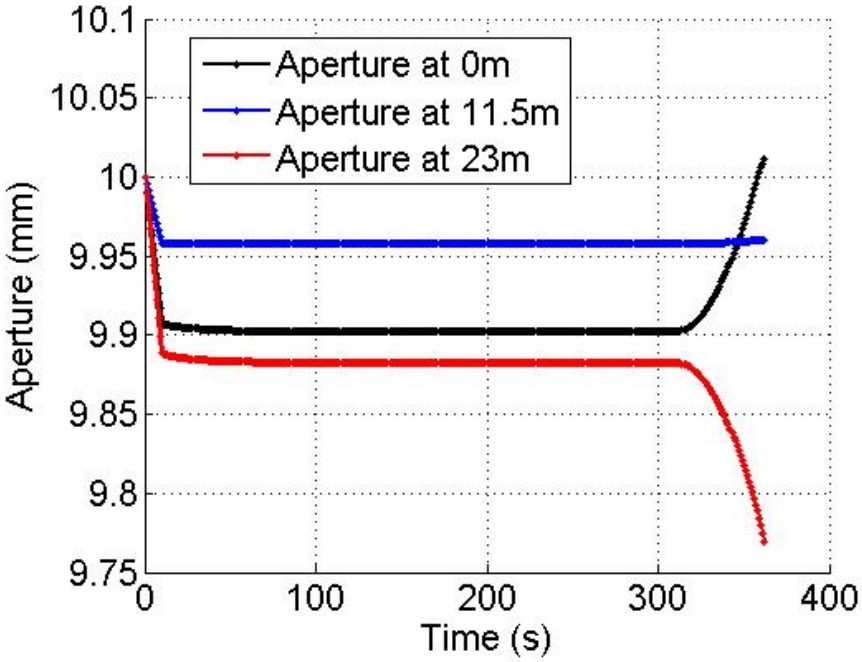

Figure 7.15: Time History of the CSEs Aperture Along the Dam-Foundation Contact for the Higher Upstream Pressure and the Initial Aperture = 1cm

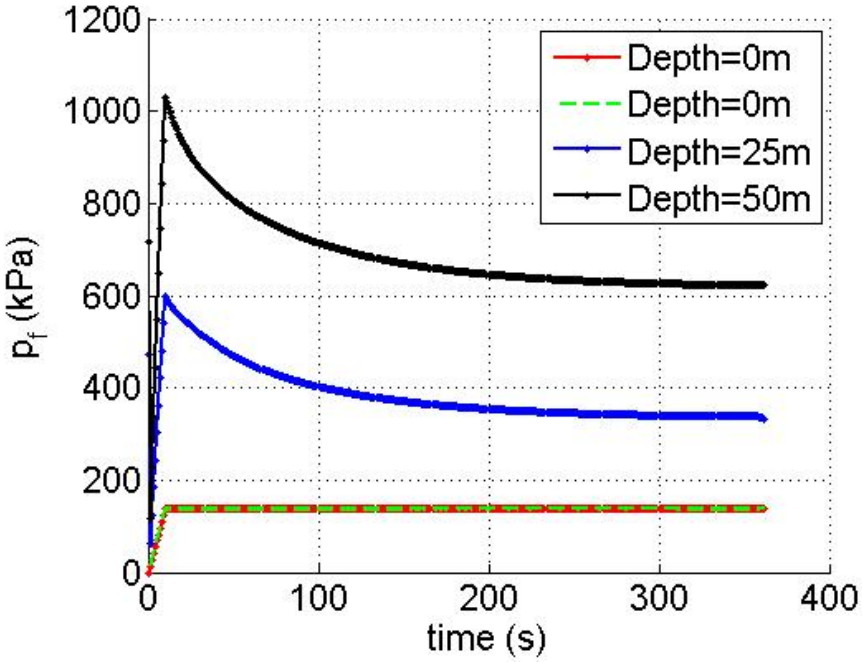

Figure 7.16: Time History of the Pore Water Pressure with Depth Through the Midpoint of the CSEs and Foundation for the Higher Upstream Pressure and the Initial Aperture = 1cm

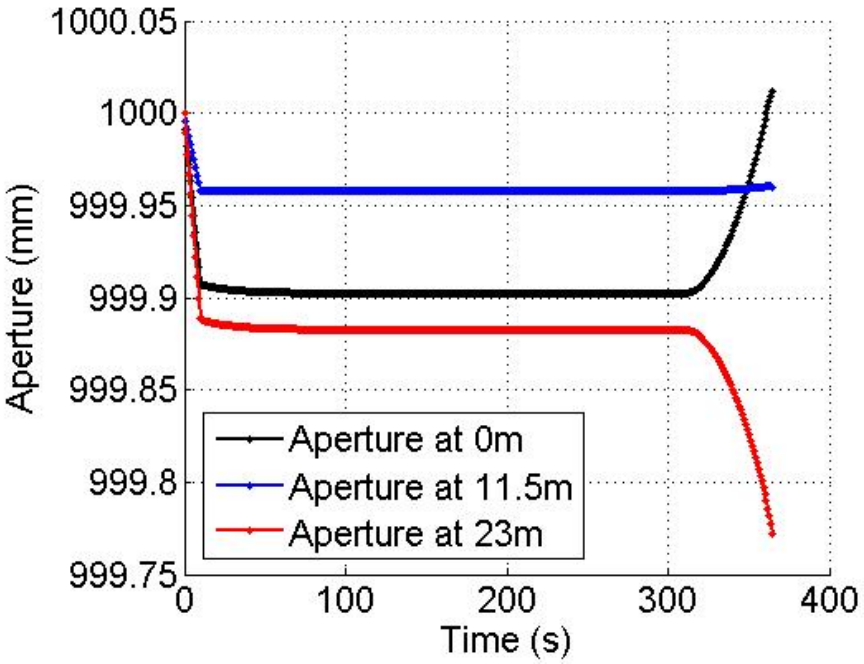

Figure 7.17: Time History of the CSEs Aperture Along the Dam-Foundation Contact for the Higher Upstream Pressure and the Initial Aperture = 1m

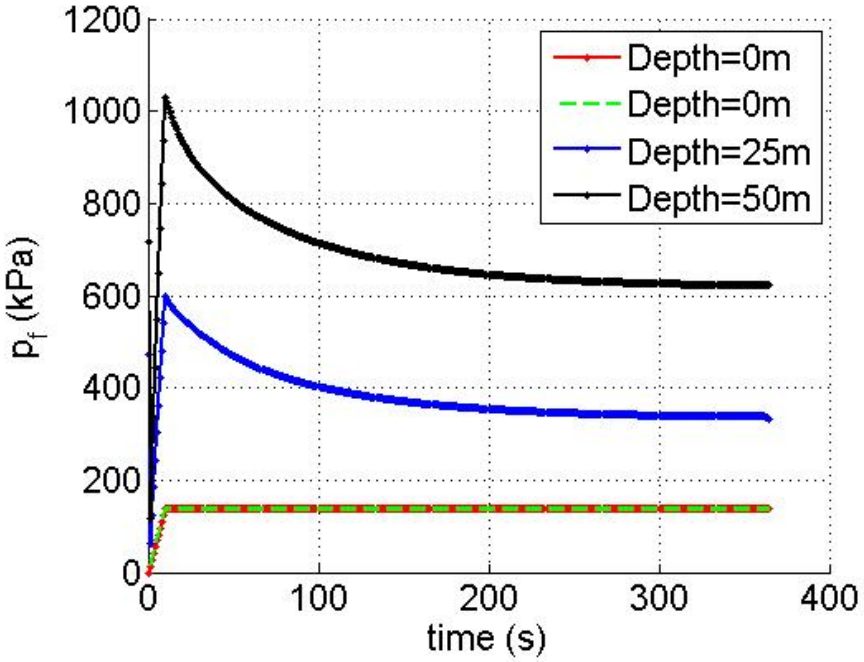

Figure 7.18: Time History of the Pore Water Pressure with Depth Through the Midpoint of the CSEs and Foundation for the Higher Upstream Pressure and the Initial Aperture = 1m

relative displacements of the CSE's nodes were equal. There were some variations in the pore water pressure time histories. The pore pressures in the CSE for the 0 m case showed some consolidation after the initial gravity load application; whereas, the other cases did not. However, it is difficult to draw concrete conclusions from these results. For one, the finite element code failed to converge and produce a full solution, but also, the finite element mesh is currently coarse. Further refinement of the mesh could lead to more influence of initial aperture on the response of the system.

Chapter 8

Future Work

8.1 Further Development of Cohesive Surface Elements in MatLab and ABAQUS

Cohesive surface elements offer the ability to directly model nucleation and propagation of fracture while accounting for fluid flow and pore pressure generation. These characteristics make them especially promising for the continued study of fractures in concrete gravity dams and their effect on overall dam stability. To that end, the CSE finite element code discussed in Chapter 7 would require further development to fully capture the necessary physics to address the problems. First, an arc length procedure needs to be implemented in order to fix convergence issues the code currently experiences during plastic yielding of the cohesive surface elements. Because the analysis is stress controlled, it is currently impossible to track the stress-displacement curve during plastic softening. An arc length procedure would follow the curve and help allow for the code to run to completion, unlike the results presented in Sections 7.2.2 and 7.2.3.

Another major code addition required to more fully understand the gravity dam problem is the ability to find a phreatic surface. Currently, porous media flow is unable to be implemented in the concrete dam, because the pore pressure solution will be inaccurate without the ability to locate the phreatic surface (it will be approximated based on the coarseness of the finite element mesh). Flow and pore pressures within the dam will directly influence the flow and pore pressure solutions within the CSEs making it an important component of the solution.

The other important changes to the current CSE finite element analysis involve expanding

the simplified gravity dam system already implemented. For one, the generation of a finer mesh, especially one with more than two cohesive surface elements, will greatly refine the solutions providing further insight into the behavior of the system. Also, the simplified implementation involves only one applied traction and an unrealistic geometry. Reapplication of the other boundary conditions and a more complicated geometry, including any drainage systems, will add accuracy to the results by more closely replicating field conditions. Finally, as discussed further in Section 7.1, the material properties used for the previous analyses did not accurately characterize either fractures in concrete or a sandstone foundation. A full characterization of both materials through careful review of existing literature or experimental testing will need to be completed to be able to gather any information other than general trends from the finite element modeling results.

As a potential alternative or addition to the necessary updates to the cohesive surface element finite element code, the same elastoplastic and poromechanical CSE formulation could be implemented into an ABAQUS user material subroutine or user element. The subroutine would be only tasked with performing the yield calculations and updating the internal state variables. ABAQUS would store the solutions, and more importantly, ABAQUS would generate the finite element mesh. ABAQUS is capable of automatically generating complicated meshes, whereas the MatLab code currently requires manual mesh creation that functionally limits the overall number of elements. Also, it is generally much simpler to develop models with complicated geometries, boundary conditions, and loading conditions using ABAQUS/CAE. Lastly, one other advantage to developing an ABAQUS UMAT is the ability to then use the other built in constitutive models, especially other complicated elastoplastic ones, for the other materials without needing to significantly update the CSE finite element code.

8.2 Co-Simulation Between ABAQUS/Standard and ABAQUS/CFD

The ABAQUS software suite is also capable of directly modeling bodies of water through ABAQUS/CFD, which is its computational fluid dynamics package. Furthermore, through co-simulations, ABAQUS/CFD can be coupled with ABAQUS/Standard, its traditional implicit solid

mechanics code in which all previous finite element models were implemented, to directly simulate the effects of fluid pressures on various structures. A co-simulation effectively passes the fluid pressure solution from ABAQUS/CFD to ABAQUS/Standard as a boundary condition, and then the stress and deformations from ABAQUS/Standard inform the flow and pressure solutions. Within the context of gravity dam modeling, this feature could be used to create realistic reservoir models that also connect to various fractures directly modeling the build-up of water pressure within these cracks. Also, ABAQUS/CFD is capable of accounting for turbulent flow, which according to EPRI Report: Volume 4 (Chinnaswamy et al., 1990), can be important when considering the effectiveness of drainage systems.

The software is not without limitations, however. Currently, ABAQUS/CFD can only model incompressible fluids. For problems involving only water, as is the case in the majority of gravity dam systems, this isn't as much an issue, but the other major limitation is the inability to couple with poromechanical analyses. As of now, ABAQUS/CFD is unable to pass fluid pressures to ABAQUS/Standard as both the necessary pore pressure boundary and traction boundary conditions (see Section 5.1).

In order to demonstrate the capabilities of ABAQUS' computational fluid dynamics software package, an example was taken from EPRI Report 1 (Amadei and Illangasekare, 1990a) from the section of the report outlining the program WELL (see Section 2.2) and implemented in ABAQUS. The program WELL uses an analytical solution developed by Goodman et al. (1983) to find the uplift pressure in a rectangular crack in dam with a constant aperture and a drain pipe. Figure 8.1 is a diagram from Goodman et al. (1983) that provides an overview of the analytical solution's geometry. WELL was reprogrammed in MatLab and example 1 from EPRI Report 1 was redone using the new code. A plot of water pressure head over the crack domain generated by the MatLab version of WELL can be found on Figure 8.2. The dip near the center of the domain is around the drain pipe, where the pressure head is kept constant.

The same geometry and boundary conditions were then implemented in ABAQUS/CFD. Figure 8.4 contains the problem geometry and mesh with overlaid water pressure contours. It

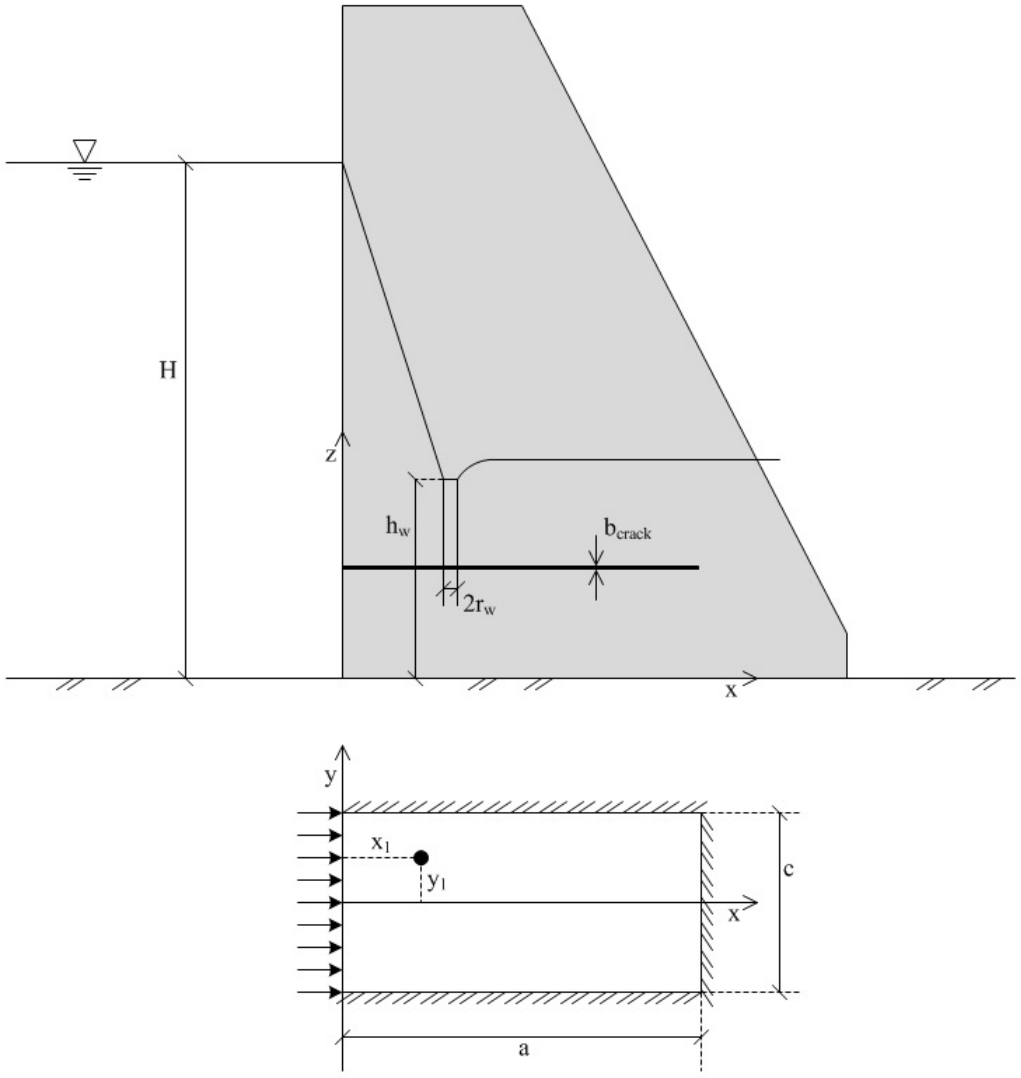

Figure 8.1: Diagram of the Analytical Solution to Water Pressure in a Rectangular Finite Crack Including Drainage from Goodman et al. (1983)

should be noted that the ABAQUS rendering contains a scale model of the problem domain; the scales for the x and y dimensions on the MatLab plot are not equal. Results from both analyses for EPRI Report 1: WELL example 1 were then compared, as seen on Figure 8.4. The curve titled "Goodman's Solution" is the result from the MatLab reprogramming of WELL and the other three curves were generated from the ABAQUS solution. All of the curves are the pressure head versus length into the crack (x) while also passing through the drain. ABAQUS/CFD requires an analysis

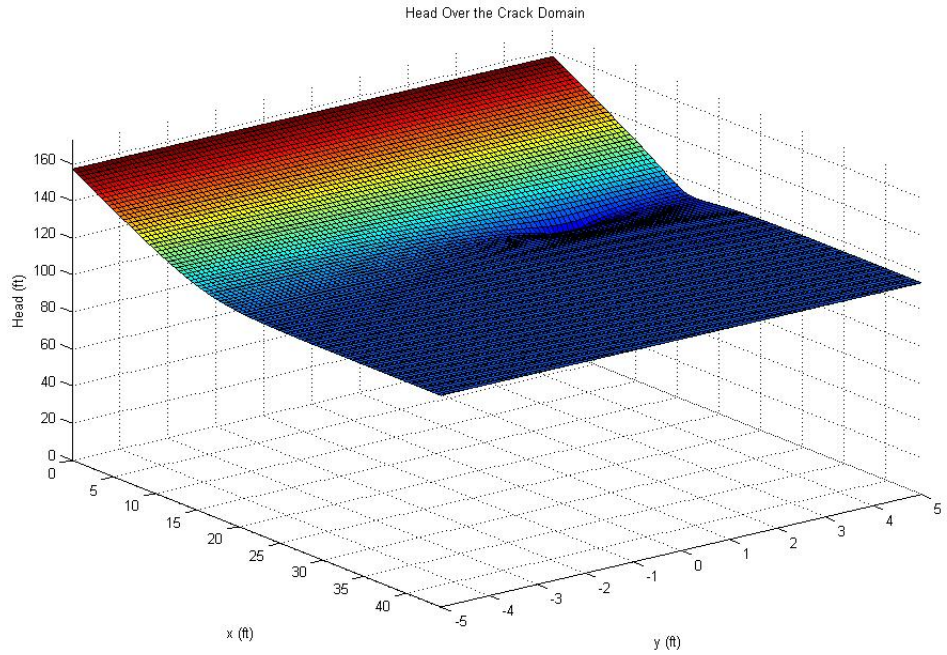

Figure 8.2: Water Pressure Result from MatLab Implementation of EPRI Report: WELL Example 1 (Amadei and Illangasekare, 1990a)

to be run transiently, so each of the three curves represents a different time step. Clearly, as the ABAQUS solution is allowed to reach steady-state, both the analytical solution and finite element analysis for this simple fracture geometry and loading conditions yield nearly identical results. The advantage of the finite element analysis is that more complicated situations that would violate the assumptions required to generate an analytical solution can be analyzed.

An example of a more complicated geometry that can be modeled using ABAQUS/CFD is a combination upstream reservoir, crack and drain, as can be seen rendered on Figure 8.5. When looking at the rendering, one needs to imagine the heel of a gravity dam fitting snuggly into the nook cut out at the base of the reservoir. In this example, water is allowed to flow from the reservoir, into the crack and then out the drain represented by an area of constant pressure head on the underside of the crack. Careful inspection of Figure 8.5 will show an area of lower pressure in the middle of the crack that is influenced by the drain.

Figures 8.6 and 8.7 display results from the realistic reservoir, crack and drain ABAQUS/CFD

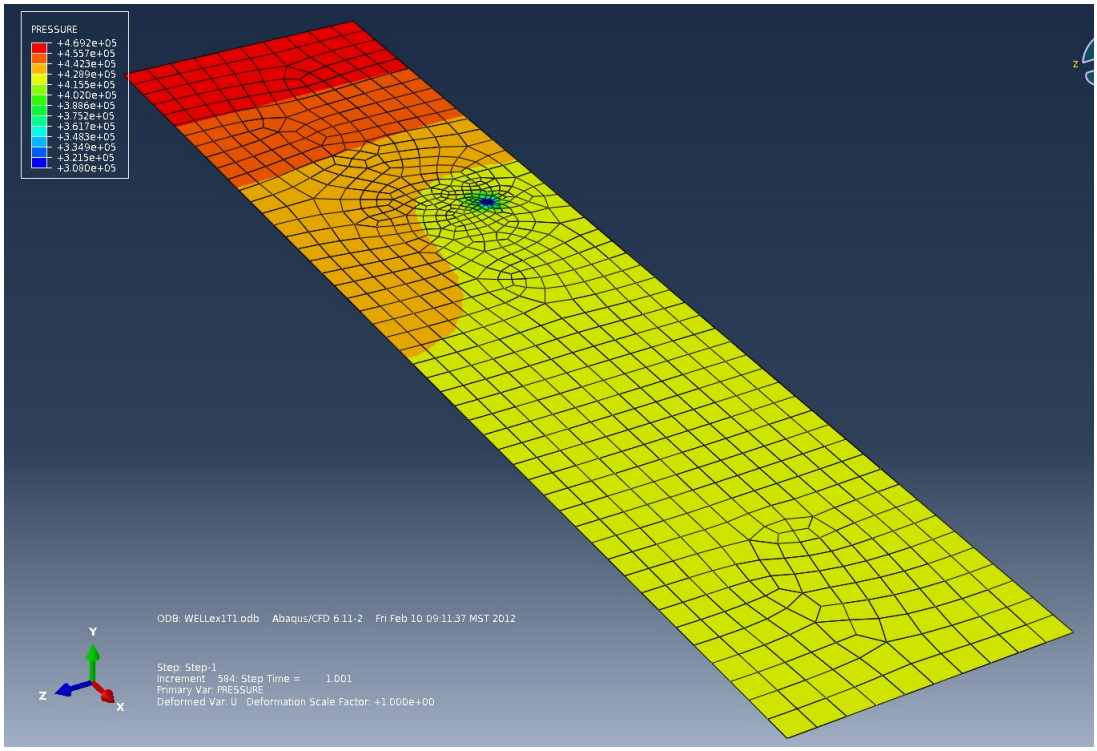

Figure 8.3: Water Pressure Result from ABAQUS Implementation of EPRI Report: WELL Example 1 (Amadei and Illangasekare, 1990a)

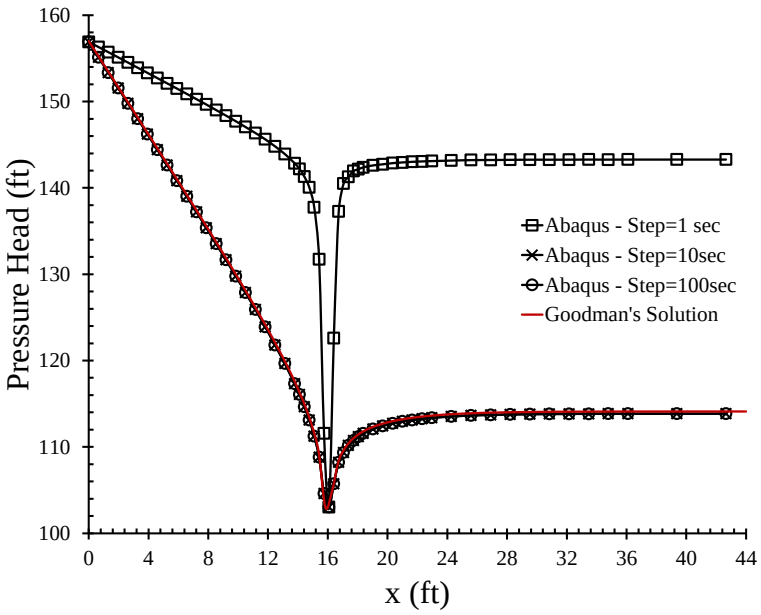

Figure 8.4: EPRI Report: WELL Example 1 MatLab versus ABAQUS/CFD Comparison

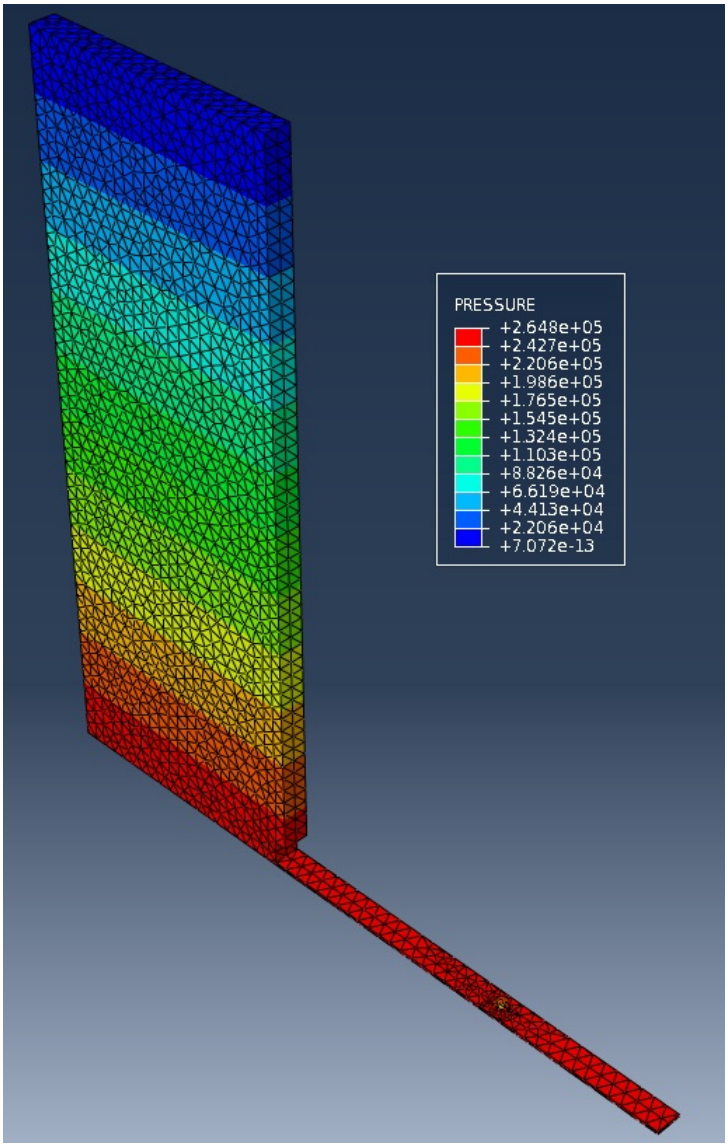

Figure 8.5: Water Pressure in a Realistic Upstream Reservoir and Crack with a Drain Geometry

model. Figure 8.6 is a plot of water pressure versus length along the underside of the reservoir and crack through the drain. In this case, x=0m is at the far side of the reservoir away from the crack entrance, the crack begins at x=10m, and the drain is positioned at x=20m. As expected, the water pressure was hydrostatic under the reservoir and decreased as it entered the crack domain. There were, however, questions as to if the solution had reached steady-state by 1000 seconds. As a result, the water pressure time histories for five points were plotted (Figure 8.7). Directly under the reservoir (x=-4.75m), the water pressure remains constant and hydrostatic. However, within

the crack (x>0), the pressure solutions fluctuated with time almost sinusoidally. It is possible that the rapid accumulation of water pressure (the analysis begins with the entire domain at 0 kPa) caused waves that hadn't fully dissipated by the end of the simulation. Regardless, by either including the effects of turbulent flow allowing for faster dissipation of energy or by letting the finite element analysis run for longer (although, a finer mesh would need to be generated in the reservoir domain where less accuracy is required to significantly decrease the analysis' run time), this realistic reservoir, crack and drain geometry could provide a valuable tool for analyzing the stability of gravity dams.

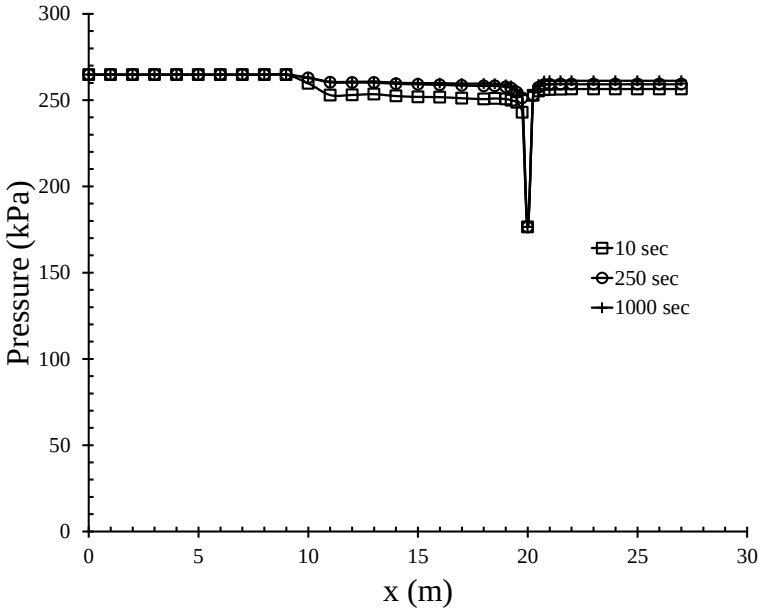

Figure 8.6: Water Pressure Along the Underside of the Reservoir and Crack (y=0m) at Various Times During the Transient ABAQUS/CFD Simulation

8.3 Implementation of a Probabilistic Framework

One primary goal of this research was to take the developed finite element models and implement them within a probabilistic framework to begin to quantify the variability associated with gravity dam stability. Determining reasonable values for the aperture and length of an in situ crack is often impossible, yet crucial to fully understanding the potential stability issues. As discussed

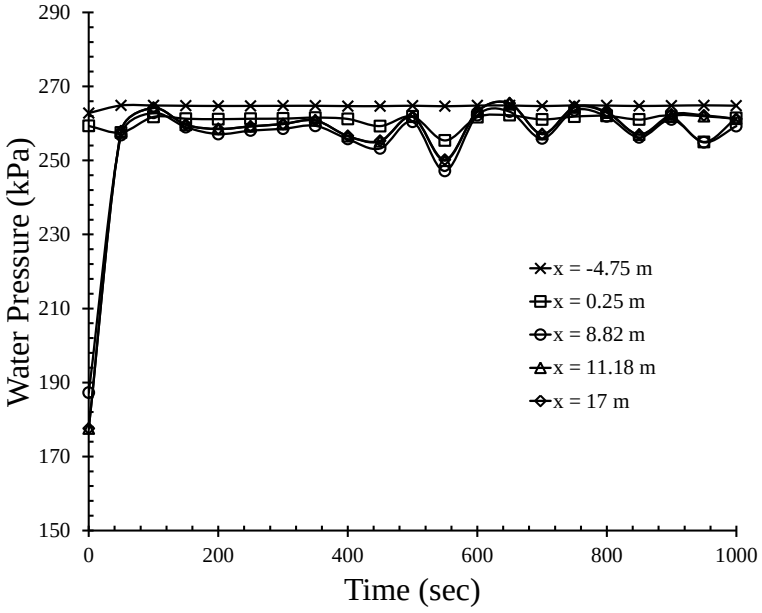

Figure 8.7: Water Pressure at Various Positions (x) Along the Underside of the Reservoir and Crack

throughout this report, there are a number of circumstances where even a small change could cause dramatic changes in a solution, such as a slightly longer crack finally intersecting a drainage system significantly altering the uplift pressure distribution. Probabilistic methods attempt to account for some uncertainty by allowing users to input probability distributions for important parameters, such as crack aperture, crack length, or foundation permeability, sample from them, and then input the sampled values into multiple runs of the finite element analysis. The many analyses are then aggregated and probability density functions of important results, such as the total uplift force or overturning moment, are generated. Based on a failure criteria defined for the particular problem, the ratio of failed analyses is compared to the total number ran to define a safety margin, replacing traditional deterministic factor of safety analyses. An example of a failure criteria could be an upper threshold on the total uplift force; all analyses that produced a high enough uplift force would be considered to have failed.

As a way to more fully understand one of the many probabilistic frameworks, an example from ERPI Report 2 (Amadei and Illangasekare, 1990b) was redone in MatLab and compared to

the results presented in said document. The EPRI report was focused on the development of the program MCWELL, which implemented the program WELL (Amadei and Illangasekare, 1990a) into a Monte Carlo iteration (see Section 2.2 for more details). Specifically, MCWELL example 1 used triangular distributions to represent the probability density functions of both crack length and width. Also, the example introduced a new parameter called "reinforcement" that was used in the failure criteria definition. When the calculated uplift force was greater than the total reinforcement resisting the uplift, the dam was considered to have failed. The amount of reinforcement was also considered to be subject to some uncertainty, so was therefore represented by a beta distribution.

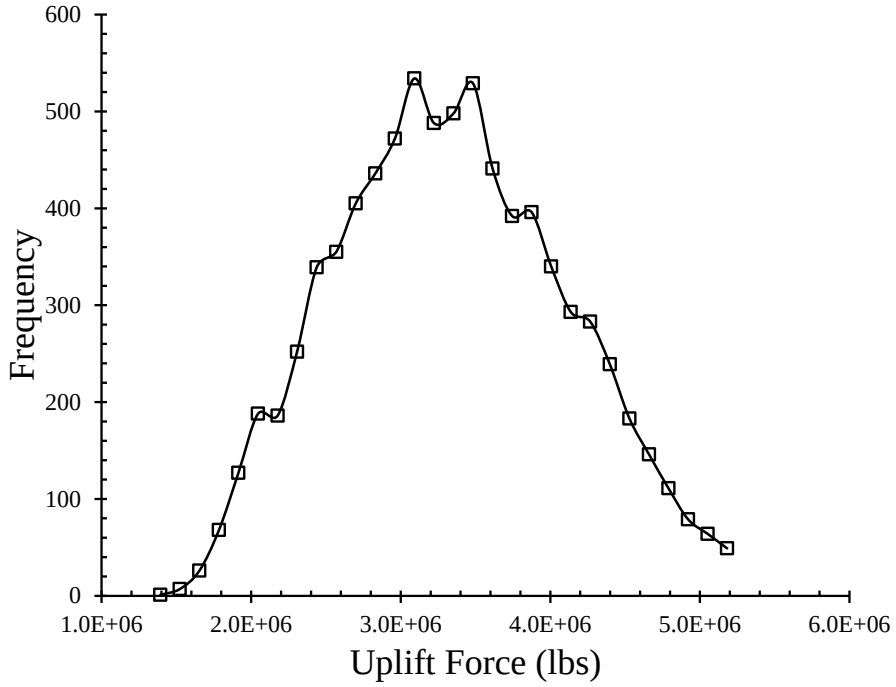

Figure 8.8: MCWELL Example 1: EPRI Results for Uplift Force Probability Density Function

Reproductions of the output probability and cumulative density functions of the total uplift force from the EPRI report are presented on Figures 8.8 and 8.10 and compared to the similar results from the example redone in MatLab on Figures 8.9 and 8.11. Table 8.1 shows a more expanded set of results comparing the mean (μ) and standard deviation (σ) of the uplift force and the x and y direction component of the overturning moment from the EPRI results to two different

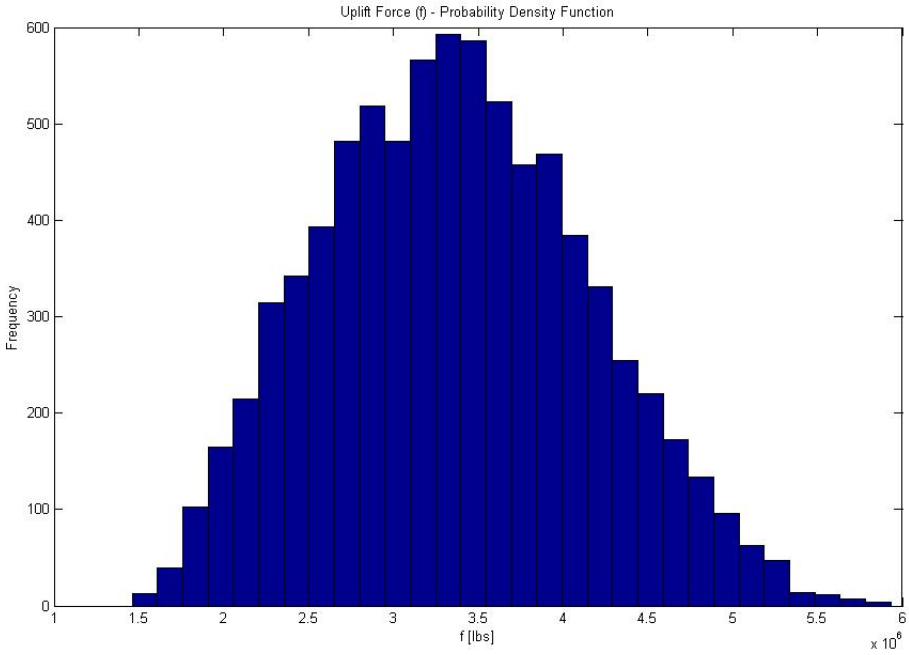

Figure 8.9: MCWELL Example 1: MatLab Results for Uplift Force Probability Density Function

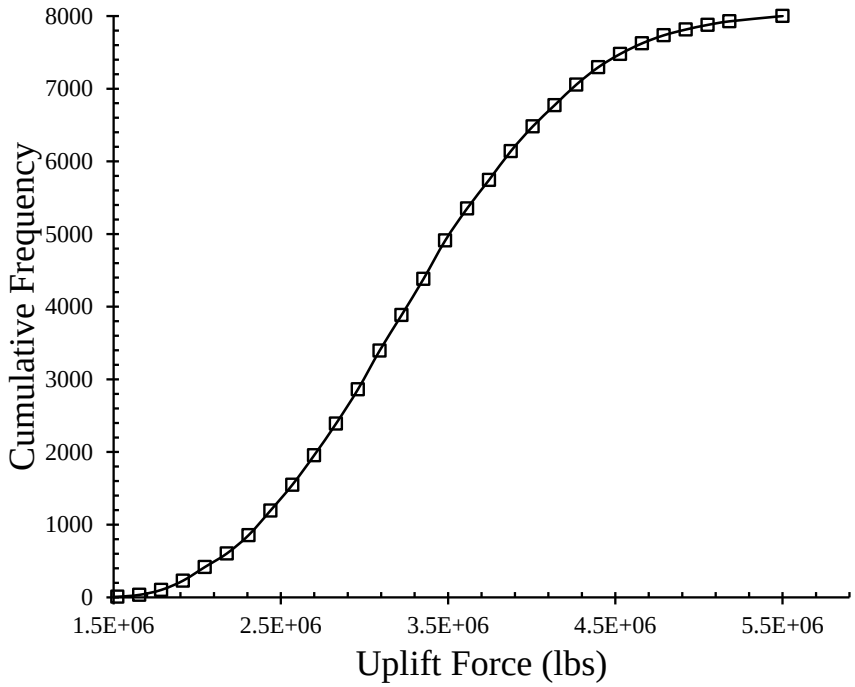

Figure 8.10: MCWELL Example 1: EPRI Results for Uplift Force Cumulative Density Function

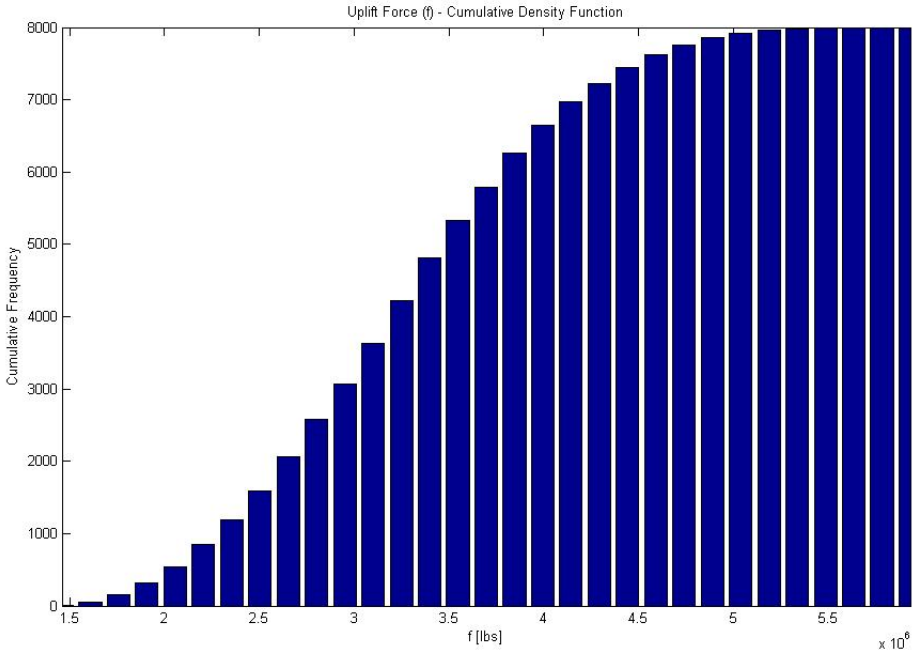

Figure 8.11: MCWELL Example 1: EPRI versus MatLab Comparisons

MatLab simulations. The first MatLab simulation was run 32,000 times, and the second 16,000 times. Also included in the table are the safety margins calculated from the three sets of results.

By inspection of the four figures, results from the version of MCWELL reprogrammed in MatLab appear to match the results from EPRI Report 2. Also, every calculated mean and safety margin were the same across all three sets of results. The only difference between the data sets was each of the standard deviations of the MatLab results were roughly twice as large as the values reported in the EPRI report. One major difference between the original MCWELL and redone MatLab version is the random number generator used to sample values from the input probability distributions. Random number generators have improved significantly since the late 1980s, such that MatLab has its own built in functions. MCWELL was originally programmed in FORTRAN, which did not have a standard generator but many user created ones, and the difference between the two could have caused the discrepancies in the standard deviations. Without knowing exactly which random number generator was originally used, this hypothesis is impossible to test. However,

Table 8.1: MCWELL Example 1 EPRI versus MatLab Comparisons

Variable	Statistic	EPRI		MatLab 32000		MatLab 16000	
Uplift Force	μ	3353	kips	3360	kips	3368	kips
	σ	314	kips	785	kips	788	kips
X-Moment	μ	-53	kips·ft	-51	kips·ft	-52	kips·ft
	σ	12	kips·ft	29	kips·ft	29	kips·ft
Y-Moment	μ	70930	kips·ft	71037	kips·ft	71244	kips·ft
	σ	8125	kips·ft	20421	kips·ft	20495	kips·ft
Safety Margin		41.57%		41.89%		42.09%	

the primary goal of implementing a probabilistic framework is the generation of safety margins, and the three sets of results produced nearly identical failure assessments.

Despite the importance of implementing probabilistic methods, the finite element models developed for this research have not yet been adapted to achieve this goal due to time restrictions. However, when they are implemented, one should consider the following thoughts on the subject. ABAQUS currently has the ability to perform relatively "simple" parametric studies. If the parameters of interest are easy to manually manipulate within an ABAQUS input file, such as material properties, which are only defined in one location, writing a python script to execute a series of analyses sampling from a probability density function of that parameter is relatively straightforward. What is significantly more difficult is varying any parameter that requires knowledge of ABAQUS' mesh generation commands, which would be required to script python code capable of changing the problem's geometry. In other words, varying some of the important parameters, like crack aperture and length, is possible, but not necessarily easy to implement.

On the other hand, the MatLab cohesive element code described in Chapter 7 could be also altered to include some probabilistic framework. One advantage of the MatLab code is that parameterizing the initial aperture or length of a fracture would be relatively simple as compared to ABAQUS. The code would require some structural changes, namely the location where the initial aperture is defined and the creation of function that runs the entire analysis, but once completed, it could become a powerful tool for analyzing fractures in gravity dams within a probabilistic frame-

work. Similarly, if an ABAQUS user subroutine implementing the same CSE formulation as the MatLab code was developed, the initial aperture of the fracture could then potentially be considered a "simple" parameter allowing for the use of ABAQUS' parametric study features. Regardless, more work needs to be done to fully delve into these possibilities for developing a probabilistic framework to accompany the many finite element models.

Chapter 9

Conclusions

The purpose of this research was to use modern finite element methods to analyze the effects of uplift pressures and fluid flow in fractures on the stability of concrete gravity dam systems. Models ranged in complexity from simple dams on rigid foundations to allowing fully coupled porous media flow through dams and their deformable foundations. Cracks and drainage systems were modeled using relatively high permeability zones, and the framework for aperture dependent, fully elastoplastic, and poromechanical cohesive surface elements and quantifying uncertainty within gravity dam systems through a probabilistic framework were laid out. Ultimately though, all of the finite element models were compared with the classical gravity dam design method. The goal was to use the comparisons to verify results gathered from the finite element analyses, but also to discover some of the advantages and limitations of both methods.

The classical method will forever be a part of gravity dam design both for its simplicity and accuracy. Provided that a dam was well constructed and founded on good rock, the classical method is more than capable of providing engineers with the necessary design parameters. Throughout this report, it has been shown that despite the added layers of complexity, the finite element analyses have been able to replicated results from the classical calculations. But where the finite element method shows its importance to gravity dam design and maintenance, is in capturing the behavior of situations that violate the assumptions of the classical methods, such as a crack extending far enough to intersect with a drain pipe or a rock fault system short circuiting a drainage curtain. Finite element analysis is also able to include more complicated material models that may be relevant

to a field condition, the ability to assess flood conditions through changing boundary conditions, and, if fully implemented, the ability to assess the nucleation and propagation of fractures using newly developed cohesive surface elements. More work needs to be done, but these models and analyses have helped expand the toolbox available to gravity dam engineers. With the full implementation of the latest methods and development of a probabilistic framework, the ability of the finite element method to fully address the problems facing concrete gravity dams seems very likely.

Bibliography

Al-Obaydi, M. A., Samadhiya, N. K., and Viladkar, M. N. (2008). 3d coupled stress-flow analysis of jointed rock mass beneath a concrete dam. In The 3rd International Conference on Water Resources and Arid Environments (2008) and the 1st Arab Water Forum.

Amadei, B. (1990). Volume 7: Three dimensional modeling of dams with cracks using the boundary element method - programs bedam and bedamc. Technical report, University of Colorado at Boulder, Department of Civil Engineering - Funded by Electric Power Reserach Institute, Boulder, CO.

Amadei, B. and Illangasekare, T. (1990a). Volume 1: An analytical soultion for uplift in concrete dams - programs well, uplift & welld. Technical report, University of Colorado at Boulder, Department of Civil Engineering - Funded by Electric Power Reserach Institute, Boulder, CO.

Amadei, B. and Illangasekare, T. (1990b). Volume 2: Uplift pressures in cracks in dams: A probabilisitc approach using monte carlo simulation - program mcwell. Technical report, University of Colorado at Boulder, Department of Civil Engineering - Funded by Electric Power Reserach Institute, Boulder, CO.

Amadei, B. and Illangasekare, T. (1990c). Volume 8: Uplift pressures in cracks in concrete gravity dams - experimental study. Technical report, University of Colorado at Boulder, Department of Civil Engineering - Funded by Electric Power Reserach Institute, Boulder, CO.

Amadei, B., Illangasekare, T., and Grenoble, B. A. (1990). Volume 5: Uplift in cracks in concrete dams - field study. Technical report, University of Colorado at Boulder, Department of Civil Engineering - Funded by Electric Power Reserach Institute, Boulder, CO.

Amadei, B., Illangasekare, T., Morris, D. I., and Boggs, H. (1989). Estimation of uplift in cracks in older concrete gravity dams: Effect of head losses in drain pipes on uplift. Journal of Energy Engineering, 115(1):39–46.

Asgian, M. (1988). A Numerical Study of Fluid Flow in Deformable, Naturally Fractured Reservoirs. Ph.d. thesis, University of Minnesota.

Bazant, Z. P. (1984). Size effects in blunt fracture: Concrete, rock, metal. Journal of Engineering Mechanics, 110(4):518–535.

Bhattacharjee, S. S. and Leger, P. (1994). Application of nlfm models to predict cracking in concrete gravity dams. Journal of Structural Engineering, 120(4):1255–1271.

Bligh, W. (1910). Dams, barrages and weirs on porous foundation. Engineering News, 64(26):708–710.

Brahtz, J. H. A. (1936). Pressures due to Percolating Water and their Influence upon Stresses in Hydraulic Structures. U.S. Department of the Interior, Bureau of Reclamation, Denver, CO.

Bruhwiler, E. and Saouma, V. E. (1995). Water fracture interaction in concrete - part ii: Hydrostatic pressure in cracks. ACI Materials Journal, 92(4):383–390.

Bureau of Reclamation (1976). Design of gravity dams. Technical report, U.S. Department of the Interior, Bureau of Reclamation, Denver, CO.

Bureau of Reclamation (1977). Design of arch dams. Technical report, U.S. Department of the Interior, Bureau of Reclamation, Denver, CO.

Bureau of Reclamation (1987). Design of small dams. Technical report, U.S. Department of the Interior, Bureau of Reclamation, Denver, CO.

Bureau of Reclamation (1999). A procedure for estimating loss of life caused by dam failure. Technical Report September, U.S. Department of the Interior, Bureau of Reclamation, Dam Safety Office, Denver, CO.

Bureau of Reclamation (2004). Drainage for dams and associated structures. Technical report, U.S Department of the Interior, Bureau of Reclamation, Technical Service Center, Denver, CO.

Carol, I., López, C. M., and Roa, O. (2001). Micromechanical analysis of quasi-brittle materials using fracture-based interface elements. International Journal for Numerical Methods in Engineering, 52(12):193–215.

Carpinteri, A. (1982a). Application of fracture mechanics to concrete structures. Journal of the Structural Division, 108(4):833–848.

Carpinteri, A. (1982b). Notch sensitivity in fracture testing of aggregative materials. Engineering Fracture Mechanics, 16(4):467–481.

Casagrande, A. (1961). Control of seepage through foundations and abutments of dams. Géotechnique, 11(3):161–182.

Cedergren, H. R. (1977). Seepage, Drainage, and Flow Nets. John Wiley & Sons.

Chahrour, A. H. and Ohtsu, M. (1994). Crack growth prediction in scaled down model of concrete gravity dam. Theoretical and Applied Fracture Mechanics, 21:29–40.

Chinnaswamy, C., Illangasekare, T., and Amadei, B. (1990). Volume 4: A numerical model to estimate uplift in cracks in gravity dams - program crflood. Technical report, University of Colorado at Boulder, Department of Civil Engineering - Funded by Electric Power Reserach Institute, Boulder, CO.

Cundall, P. (1983). Numerical modelling of water flow in rock masses. Technical report, Department of the Environment, London, England.

Dewey, R. R., Reich, R. W., and Saouma, V. E. (1994). Uplift modeling for fracture mechanics analysis of concrete dams. Journal of Structural Engineering, 120(10):3025–3044.

Ebeling, R. M., Nuss, L. K., Tracy, F. T., and Brand, B. (2000). Evaluation and comparison of stability analysis and uplift criteria for concrete gravity dams by three federal agencies. Technical Report January, Department of the Army, U.S. Army Corps of Engineers, Washington, D.C.

Federal Energy Regulatory Commission (1997). Engineering guidelines for the evaluation of hydropower projects: Chapter 10 - other dams. Technical Report October, Federal Energy Regulatory Commission, Division of Dam Safety and Inspections, Washington, DC.

Federal Energy Regulatory Commission (1999). Engineering guidelines for the evaluation of hydropower projects: Chapter 11 - arch dams. Technical report, Federal Energy Regulatory Commission, Division of Dam Safety and Inspections, Washington, DC.

Federal Energy Regulatory Commission (2002). Engineering guidelines for the evaluation of hydropower projects: Chapter 3 - gravity dams. Technical Report October, Federal Energy Regulatory Commission, Division of Dam Safety and Inspections, Washington, DC.

Goodman, R. E., Amadei, B., and Sitar, N. (1983). Uplift pressure in crack below dam. Journal of Energy Engineering, 109(4):207–221.

Grenoble, B. A. (1989). Influence of Geology on Seepage and Uplift in Concrete Gravity Dam Foundations. Ph.d. thesis, University of Colorado at Boulder.

Grenoble, B. A., Amadei, B., and Illangasekare, T. (1990). Volume 6: Influence of rock discontinuities on seepage and uplift in concrete gravity dam foundations - program jointflo. Technical report, University of Colorado at Boulder, Department of Civil Engineering - Funded by Electric Power Reserach Institute, Boulder, CO.

Grenoble, B. A., Illangasekare, T., and Amadei, B. (1988). Crflow: Finite element analysis for flow through a crack in a concrete dam. Technical report, University of Colorado at Boulder, Department of Civil Engineering - Funded by Electric Power Reserach Institute, Boulder, CO.

Hillerborg, A. (1983). Fracture Mechanics of Concrete. Elsevier, New York, NY.

Hillerborg, A., Modeer, M., and Petersson, P.-E. (1976). Analysis of crack formation and crack growth in concrete by means of fracture mechanics and finite elements. Cement and Concrete Research, 6:773–782.

Illangasekare, T., Amadei, B., and Brannon, J. H. (1990). Volume 3: A model to estimate uplift in a crack with a box drain - program intra1. Technical report, University of Colorado at Boulder, Department of Civil Engineering - Funded by Electric Power Reserach Institute, Boulder, CO.

Irwin, G. (1957). Analysis of stresses and strains near the end of a crack traversing a plate. Journal of Applied Mechanics, 24(3):391–364.

Junrui, C., Yanqing, W., and Shouyi, L. (2004). Analysis of coupled seepage and stress fields in rock mass around the xiaowan arch dam. Communications in Numerical Methods in Engineering, 20(8):607–617.

Kaplan, M. F. (1961). Crack propagation and the fracture of concrete. Journal of the American Concrete Institute, 58(5):591–609.

Li, Z. (1995). Viscoplastic damage model applied to cracking of gravity dam. Theoretical and Applied Fracture Mechanics, 22(2):165–170.

Long, J. (1983). Investigation of Equivalent Porous Medium Permeability in Networks of Discontinuous Fractures. Ph.d. thesis, University of California, Berkeley.

Louis, C. (1969). Rock Mechanics Research Report No. 10: A Study of Groundwater Flow in Jointed Rock and Its Influence on the Stability of Rock Masses. Imperial College of Science and Technology, London, England.

Mills-Bria, B. L., Nuss, L., O'Connell, D., and Harris, D. (2006). State-of-practice for the non-linear analysis of concrete dams at the bureau of reclamation. Technical Report January, U.S. Department of the Interior, Bureau of Reclamation, Denver, CO.

Mirzabozorg, H. and Ghaemian, M. (2005). Non-linear behavior of mass concrete in three-dimensional problems using a smeared crack approach. Earthquake Engineering & Structural Dynamics, 34(3):247–269.

Muskat, M. (1937). The flow of fluids through porous media. Journal of Applied Physics, 8(4):274.

Oda, M. (1986). An equivalent continuum model for coupled stress and fluid flow analysis in jointed rock masses. Water Resources Research, 22(13):1845–1856.

Plizzari, G. A. (1998). On the influence of uplift pressure in concrete gravity dams. Engineering Fracture Mechanics, 59(3):253–267.

Reich, R. W. (1993). On the Marriage of Fracture Mechanics and Mixed Finite Element Methods: An Application to Concrete Dams. Ph.d. thesis, University of Colorado at Boulder.

Riegel, Alexander, Creager, Harza, Houk, Karpov, Matthes, Steele, Stratton, and Wiggin (1952). Uplift in masonry dams: Final report of the subcommittee on uplift in masonry dams of the committee on masonry dams of the power division. Transactions, 117:1218–1252.

Robinson, P. C. (1984). Connectivity, Flow and Transport in Network Models of Fractured Media. Ph.d thesis, Oxford University.

Rocha, M. and Franciss, F. (1977). Determination of permeability in anisotropic rock-masses from integral samples. 9:67–93.

Samaniego, J. A. (1985). Simulation of Fluid Flow in Fractured Rock: A Probabilistic Approach. Ph.d. thesis, University of London.

Saouma, V. E., Ayari, M., and Boggs, H. (1989). Fracture of Concrete and Rock. Springer-Verlag, New York, NY.

Scott, G. A. (1999). Guidelines: Foundation and geotechnical studies for existing concrete dams. Technical Report September, U.S. Department of the Interior, Bureau of Reclamation, Technical Service Center, Denver, CO.

Scott, G. A. and Mills-Bria, B. L. (2008). Nonlinear, 3-d, dynamic, coupled dam-foundation analyses for estimating risks at hungry horse dam. In 28th Conference of the U.S. Society of Dams, Portland, Or.

Segura, J. M. and Carol, I. (2004). On zero-thickness interface elements for diffusion problems. International Journal for Numerical and Analytical Methods in Geomechanics, 28(9):947–962.

Segura, J. M. and Carol, I. (2008a). Coupled hm analysis using zero-thickness interface elements with double nodes. part i : Theoretical model. International Journal for Numerical and Analytical Methods in Geomechanics, 32(August):2083–2101.

Segura, J. M. and Carol, I. (2008b). Coupled hm analysis using zero-thickness interface elements with double nodes, part ii : Verification and application. International Journal for Numerical and Analytical Methods in Geomechanics, 32(September):2103–2123.

Serafim, J. L. and del Campo, A. (1965). Interstitial pressures on rock foundations of dams. Journal of Soil Mechanics and Foundations Division, 91(SM-5):65–85.

Shapiro, A. M. and Andersson, J. (1983). Steady state fluid response in fractured rock: A boundary element solution for a coupled, discrete fracture continuum model. Water Resources Research, 19(4):959–969.

Shi, Z., Suzuki, M., and Nakano, M. (2003). Numerical analysis of multiple discrete cracks in concrete dams using extended fictitious crack model. Journal of Structural Engineering, 129(3):324.

Slowik, V. and Saouma, V. E. (2000). Water pressure in propagating concrete cracks. Journal of Structural Engineering, (February):235–242.

Snow, D. T. (1969). Anisotropic permeability of fractured media. Water Resources Research, 5(6):1273–1289.

Strassburger, A. (1988). Uplift pressures in existing concrete dams: Preliminary report to the electric power research institute. Technical report, Electric Power Research Institute.

Stuart, W. (1963). Influence of geological conditions on uplift. Transactions, 128(I):765–780.

Sweetser, J. D. (2012). Fracture Model for Fluid Saturated Geomaterials Implemented Via a Poro-Elasto-Plastic Cohesive Surface Finite Element. M.s. thesis, University of Colorado at Boulder.

Terzaghi, K. (1929). Effect of minor geologic details on the safety of dams. AIME Technical Publication, 215:31–44.

U.S. Army Corps of Engineers (1994). Arch dam design. Technical report, Department of the Army, U.S. Army Corps of Engineers, Washington, D.C.

U.S. Army Corps of Engineers (1995). Gravity dam design. Technical Report June, Department of the Army, U.S. Army Corps of Engineers, Washington, D.C.

U.S. Army Corps of Engineers (2005). Stability analysis of concrete structures. Technical Report December, Department of the Army, U.S. Army Corps of Engineers, Washington, D.C.

Utili, S., Yin, Z., and Jiang, M. (2008). Influences of hydraulic uplift pressures on stability of gravity dam. Chinese Journal of Rock Mechanics and Engineering, 27(8):1554–1568.

Wang, C.-K., Salmon, C. G., and Pincheir, J. A. (2007). Reinforced Concrete Design. John Wiley & Sons, Hoboken, NJ, 7th edition.

Watermeyer, C. (2006). A review of the classical method of design of medium height gravity dams and aspects of base shortening with uplift. Journal of the South African Institution of Civil Engineering, 48(3):2–11.

Widmann, R. (1990). Fracture mechanics and its limits of application in the field of dam construction. Engineering Fracture Mechanics, 35(1/2/3):531–539.

Yu, S.-K. (2010). Two-Dimensional Cohesive Surface Elements for Quasi-static Elasto-plastic/ Rigid-plastic Pressure-sensitive Cohesive Surface Models. Notes, University of Colorado at Boulder, Boulder, CO.

Appendix A

Overview of the Classical Dam Design Method and Factor of Safety Analysis (Adapted from Watermeyer (2006))

The classical gravity dam design method is outlined in many documents including Bureau of Reclamation (1987) and U.S. Army Corps of Engineers (1995), but for the purposes of this research, Watermeyer (2006) was used as the primary source for information regarding the method. This appendix is intended to provide a more in depth overview of the factor of safety calculations performed throughout this report using the classical design method and also the finite element analysis results.

Based on rigid body statics, the classical dam design method relies on analyzing the forces and moments due to the self-weight of the dam, the upstream and downstream reservoirs, any backfill soil, and uplift pressures acting along the dam-foundation contact. By summing all the components of these forces, the resultant forces are then input into the factor of safety equations (Equations (A.1) and (A.2)) in order to analyze the stability of the system. This section will summarize the calculations required to calculate these factors of safety. Also, throughout this report, an example dam from Watermeyer (2006) was continually used to compare the classical design method and finite element results. The same geometry was used here simplifying the analysis. Watermeyer provides a more general set of equations in his paper in order to account for more complicated dam geometries and the application of other unspecified external loads.

$$FS_{sliding} = \frac{CA_b + T\tan(\phi)}{P} \tag{A.1}$$

$$FS_{overturning} = \frac{WE_w}{UE_u + PE_p} \tag{A.2}$$

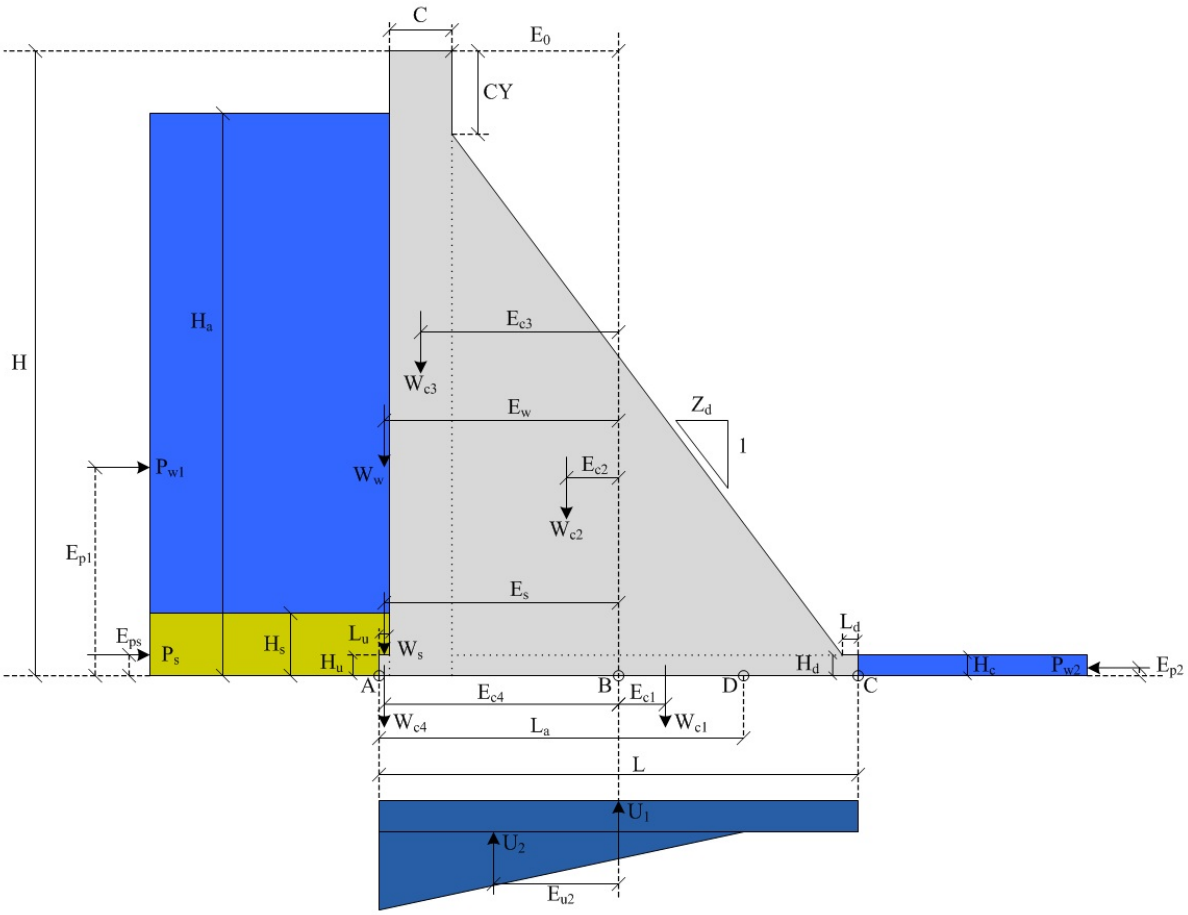

Figure A.1: Classical Dam Design Method Geometry and Variable Definitions (Watermeyer, 2006)

Figure A.1 contains definitions for all required dimensions and forces superimposed on the dam geometry. Also, a full list of the variables and their descriptions can be found in Table A.1. On the figure, point A is at the dam heel, point C is at the toe, and B is at the dam's centerline. Point D represents the location of a drainage system defined by L_a. The drain affects the uplift pressure profile, which is represented by the blue section under the dam. Any uplift pressure applied over the entire dam-foundation contact (the downstream reservoir pressure that acts between the dam's toe and drainage system) is called U_1. All "excess" uplift pressures are called U_2.

To calculate the total downward force W, the following set of equations are used.

Table A.1: Classical Dam Design Variables and Descriptions (Watermeyer, 2006)

Category	Variable	Description
Dam Dimensions	H (m)	Dam Height
	H_a (m)	Upstream water level
	H_c (m)	Downstream water level
	H_s (m)	Height of upstream soil
	L (m)	Dam length
	L_a (m)	Distance from dam heel to drainage system
	C (m)	Dam Crest Length
	CY (m)	Length of dam crest's vertical section
	Z_d (m)	Downstream face slope ($Z_d/1$)
	H_u (m)	Heel notch height
	L_u (m)	Heel notch length
	H_d (m)	Toe notch height
	L_d (m)	Toe notch length
Downward Force (W)	W_{c1} (kN)	Weight of concrete section 1
	W_{c2} (kN)	Weight of concrete section 2
	W_{c3} (kN)	Weight of concrete section 3
	W_{c4} (kN)	Weight of concrete section 4
	W_w (kN)	Weight of water
	W_s (kN)	Weight of soil
Horizontal Force (P)	P_{w1} (kN)	Upstream reservoir force
	P_{w2} (kN)	Downstream reservoir force
	P_s (kN)	Downstream soil force
Uplift Force (U)	U_1 (kN)	Uplift force due to downstream reservoir
	U_2 (kN)	Uplift due to upstream reservoir including drainage
Eccentricities	$E_\circ$ (m)	Distance from dam centerline to downstream face
	E_{c1} (m)	W_{c1} to dam centerline
	E_{c2} (m)	W_{c2} to dam centerline
	E_{c3} (m)	W_{c3} to dam centerline
	E_{c4} (m)	W_{c4} to dam centerline
	E_w (m)	W_w to dam centerline
	E_s (m)	W_s to dam centerline
	E_{p1} (m)	Dam base to P_{w1}
	E_{p2} (m)	Dam base to P_{w1}
	E_s (m)	Dam base to P_s
	E_{u2} (m)	U_2 to dam centerline
Other Parameters	γ_w (kN/m^3)	Unit weight of water
	γ_c (kN/m^3)	Unit weight of concrete
	γ_s' (kN/m^3)	buoyant unit weight of soil
	ϕ ($^\circ$)	Friction angle of the soil
	C (kPa)	Cohesion
	A_b (m^2)	Area of the base (assumes width = 1 m)

$$W_{c1} = \gamma_c H_d (H - CY) Z_d \tag{A.3}$$

$$W_{c2} = \frac{\gamma_c Z_d (H - CY - H_d)^2}{2} \tag{A.4}$$

$$W_{c3} = \gamma_c HC \tag{A.5}$$

$$W_{c4} = \gamma_c H_u \left(\frac{L}{2} - E_\circ - C \right) \tag{A.6}$$

$$W_w = \gamma_w L_u (H_a - H_u) \tag{A.7}$$

$$W_s = \gamma'_s L_u (H_s - H_u) \tag{A.8}$$

$$W = W_{c1} + W_{c2} + W_{c3} + W_{c4} + W_w + W_s \tag{A.9}$$

Similarly, the total horizontal force (P) is found using the following.

$$P_{w1} = \frac{\gamma_w H_a^2}{2} \tag{A.10}$$

$$P_{w2} = \frac{\gamma_w H_c^2}{2} \tag{A.11}$$

$$P_s = \frac{5 H_s^2}{3} \tag{A.12}$$

$$P = (P_{w1} - P_{w2}) + P_s \tag{A.13}$$

Equation (A.12) is derived from the horizontal pressure caused by submerged sediment equation, which relates the soil's friction angle (ϕ), buoyant unit weight (γ'_s), and depth to a horizontal pressure (S_p) (see Equation (A.14)). Given the soil is cohesionless, has a friction angle of 30°, and a buoyant unit weight of 10.0 kN/m^3, Equation (A.14) reduces to $\frac{10h}{3}$.

$$S_p = \frac{\gamma'_s h (1 - \sin\phi)}{1 + \sin\phi} = \frac{10h}{3} \tag{A.14}$$

Lastly, the total uplift force (U) is calculated as follows,

$$U_1 = \gamma_w L H_c \tag{A.15}$$

$$U_2 = \frac{\gamma_w L_a (H_a - H_c)}{2} \tag{A.16}$$

$$U = U_1 + U_2 \tag{A.17}$$

and the effective vertical force is calculated using the effective stress principle (Equation (A.18)).

$$T = W - U \tag{A.18}$$

The values of T and P are then input into Equation A.1 to calculate the factor of safety against sliding.

In order to evaluate the factor of safety against overturning, the eccentricities of each force are first calculated. To ease the calculations, $E_\circ$ is defined to be the distance between the centerline of the dam to the vertical section of the downstream face.

$$E_\circ = \frac{L}{2} - (L_u + C) \tag{A.19}$$

$$E_{c1} = \frac{L - HZ_d + CYZ_d}{2} \tag{A.20}$$

$$E_{c2} = \frac{(H - CY - H_d)Z_d}{3} - E_\circ \tag{A.21}$$

$$E_{c3} = E_\circ + \frac{C}{2} \tag{A.22}$$

$$E_{c4} = \frac{L - L_u}{2} \tag{A.23}$$

$$E_w = \frac{L - L_u}{2} \tag{A.24}$$

$$E_s = \frac{L - L_u}{2} \tag{A.25}$$

$$E_{p1} = \frac{H_a}{3} \tag{A.26}$$

$$E_{p2} = \frac{H_c}{3} \tag{A.27}$$

$$E_s = \frac{H_s}{3} \tag{A.28}$$

$$E_{u2} = \frac{L}{2} - \frac{L_a}{3} \tag{A.29}$$

With the eccentricities calculated, the righting (M_cO) and overturning moment (M_cR) about the toe of the dam, point C, are calculated. The righting moment is essentially the sum of each

component of the total downward force (W), and the overturning moment is the sum of all uplift (U) and horizontal forces (P). There is one exception in that the downstream reservoir force, P_{w2}, applies a righting moment about point C. Ultimately, the factor of safety against overturing is the ratio of the righting to overturning moment.

M_cO can be calculated directly by the following equation. For reference, all moments are defined to be positive rotating clockwise, except M_cR which is positive counter-clockwise.

$$M_cO = P_{w1}E_{p1} + P_sE_s + \frac{U_1L}{2} + U_2\left(E_{u2} + \frac{L}{2}\right) \tag{A.30}$$

In order to calculate M_cR, the moment about the midpoint of the dam-foundation contact (M_b) is first found. All the eccentricities are defined relative to the midpoint (point B).

$$\begin{aligned} M_b = {} & (W_{c1}E_{c1} + P_{w1}E_{p1} + P_sE_s + U_2E_{u2}) \\ & - (W_{c2}E_{c2} + W_{c3}E_{c3} + W_{c4}E_{c4} + W_wE_w + W_sE_s + P_{w2}E_{p2}) \end{aligned} \tag{A.31}$$

The moment about the toe of the dam (M_c) can then be found by shifting M_b to point C and accounting for the changing moment arms of all the downward and uplift forces. This can be done easily by recognizing that the effective downward force (T) represents the sum of all downward and uplift forces, resulting in the following equation.

$$M_c = M_b - \frac{TL}{2} \tag{A.32}$$

The righting moment is then calculated by subtracting the overturning moment from the total moment about point C, and because M_cR is defined to be positive counter-clockwise, it is multiplied by -1.

$$M_cR = M_cO - M_c \tag{A.33}$$

Finally, the factor of safety against overturning is the ratio between the righting to overturning moment about the toe of the dam.

$$FS_{overturning} = \frac{M_c R}{M_c O} \tag{A.34}$$

In order to compare the finite element modeling results to the classical factor of safety calculations, stress distributions along the dam-foundation contact were plotted and integrated over the total length of the dam using the trapezoidal rule, Equation (A.35), (assuming a unit width) to get forces, as seen on Figure A.2. For analyses without pore fluid flow, the total vertical compressive stress and shear stress distributions were used to find values of total downward vertical force (W) and horizontal force (P). The total uplift force (U) was still calculated using the classical method in these analyses, because the uplift pressure was applied as a boundary condition to the finite element models. In analyses including pore fluid flow, the effective vertical compressive stress, shear stress, and uplift pressure solutions were all solved for directly. When integrated, these stresses resulted in the effective downward force (T), horizontal force (P), and uplift force (U).

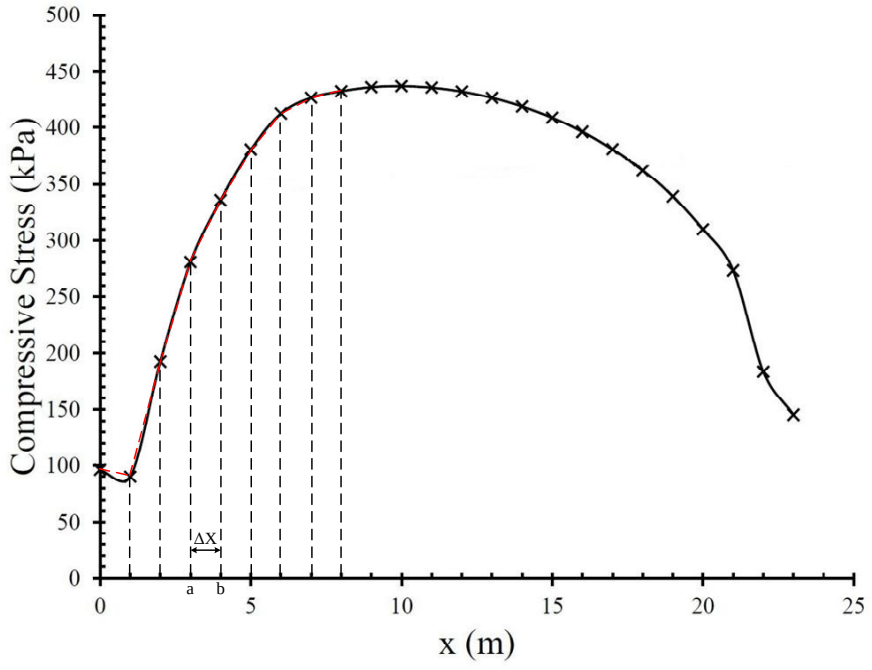

Figure A.2: Example Numerical Integration Using the Trapezoidal Rule

$$T = \int_a^b f(x)\,dx \approx (b-a)\frac{f(a)+f(b)}{2} \tag{A.35}$$

To calculate the factor of safety against sliding from the finite element modeling results, the calculated forces were directly input into Equation (A.1). In the cases without pore fluid flow, U was subtracted from W to calculate T prior to input into the equation. Also, because gravity and the horizontal loads were ramped up linearly and over two different time-steps, there were cases where the model failed to converge prior to the application of 100% of the horizontal loads. In these cases, the full shear stress distribution (i.e. the distribution under the full loads) was not generated. After integrating the shear stress solution, the calculated value for P was divided by the percent completion to estimate the total shear that would have been attained had the model ran to completion. As for the factor of safety against overturning, it was assumed that the deformations of the dam were small such that the eccentricities of the loads did not significantly change. Therefore, the value of T calculated using the finite element results was input into Equation (A.32), and the factor of safety calculation followed the subsequent steps outlined above.

Appendix B

Ultimate Failure Surface ABAQUS User Material (UMAT) Subroutine Code

The following fortran code (*umat_DP_cap.f*) implements a Drucker-Prager yield surface modified to include tension and compression caps in order to calculate the ultimate failure of concrete using the ABAQUS finite element software suite.

```
      SUBROUTINE UMAT(STRESS,STATEV,DDSDDE,SSE,SPD,SCD,
     1 RPL,DDSDDT,DRPLDE,DRPLDT,STRAN,DSTRAN,
     2 TIME,DTIME,TEMP,DTEMP,PREDEF,DPRED,MATERL,NDI,NSHR,NTENS,
     3 NSTATV,PROPS,NPROPS,COORDS,DROT,PNEWDT,CELENT,
     4 DFGRD0,DFGRD1,NOEL,NPT,KSLAY,KSPT,KSTEP,KINC)
C
      INCLUDE 'ABA_PARAM.INC'
C
      CHARACTER*80 MATERL
      DIMENSION STRESS(NTENS),STATEV(NSTATV),
     1 DDSDDE(NTENS,NTENS),DDSDDT(NTENS),DRPLDE(NTENS),
     2 STRAN(NTENS),DSTRAN(NTENS),TIME(2),PREDEF(1),DPRED(1),
     3 PROPS(NPROPS),COORDS(3),DROT(3,3),
     4 DFGRD0(3,3),DFGRD1(3,3)
C
      DIMENSION S_DEV(6),FLOW(6),FLOW_PHI(6),FLOW_PSI(6)
      PARAMETER (ONE=1.0D0,TWO=2.0D0,THREE=3.0D0,SIX=6.0D0,
     1 SMALL=1.D-12,ZERO=0.0D0)
C
C -------------------------------------------------------------
C     UMAT FOR ISOTROPIC BILINEAR ELASTO-PLASTICITY
C     DRUCKER-PRAGER
C     GENERAL 3D FORMULATION
C
C **THIS SUBROUTINE JUST CALCULATES THE YIELD FUNCTION AND DOES
C   NOT EVOLVE PLASTICITY
C -------------------------------------------------------------
C     PROPS(1) - E
```

```
C     PROPS(2) - NU
C     PROPS(3) - COHESION
C     PROPS(4) - PHI
C     PROPS(5) - BETA
C     PROPS(6) - KAPPA
C     PROPS(7) - RELLIP
C     PROPS(8) - CHI
C -----------------------------------------------------------
C
C     ELASTIC PARAMETERS
C
      EMOD=PROPS(1)
      ENU=PROPS(2)
      IF(ENU.GT.0.4999.AND.ENU.LT.0.5001) ENU=0.499
      EBULK3=EMOD/(ONE-TWO*ENU)
      EBULK=EBULK3/THREE
      EG2=EMOD/(ONE+ENU)
      EG=EG2/TWO
      EG3=THREE*EG
      ELAM=(EBULK3-EG2)/THREE
C
C     CALCULATE A^PHI, B^PHI
C
      COHESION=PROPS(3)
      PHI=PROPS(4)
      BETA=PROPS(5)
      CONST1=TWO*SQRT(SIX)/(THREE+BETA*SIN(PHI))
      ABARPHI=CONST1*COS(PHI)
      APHI=CONST1*COHESION*COS(PHI)
      BPHI=CONST1*SIN(PHI)
C
C     ELASTIC TANGENT MODULUS (IN MATRIX FORM)
C...INITIALIZE
      DO 20 K1=1,NTENS
        DO 10 K2=1,NTENS
           DDSDDE(K2,K1)=0.0D0
 10     CONTINUE
 20   CONTINUE
C...ASSIGN PARAMETERS
      DO 40 K1=1,NDI
        DO 30 K2=1,NDI
           DDSDDE(K2,K1)=ELAM
 30     CONTINUE
        DDSDDE(K1,K1)=EG2+ELAM
 40   CONTINUE
      DO 50 K1=NDI+1,NTENS
         DDSDDE(K1,K1)=EG
```

```
 50   CONTINUE
C
C    CALCULATE TRIAL STRESS USING INCREMENTAL TOTAL STRAIN
C
      DO 70 K1=1,NTENS
        DO 60 K2=1,NTENS
           STRESS(K2)=STRESS(K2)+DDSDDE(K2,K1)*DSTRAN(K1)
 60     CONTINUE
 70   CONTINUE
C
C    CALCULATE MEAN AND DEVIATORIC TRIAL STRESSES
C
      DO 80 K1=1,NTENS
         S_DEV(K1)=STRESS(K1)
 80   CONTINUE
      STRESS_MEAN=(STRESS(1)+STRESS(2)+STRESS(3))/THREE
      DO 85 K1=1,NDI
         S_DEV(K1)=S_DEV(K1)-STRESS_MEAN
 85   CONTINUE
C
C    CALCULATE L2 NORM OF DEVIATORIC STRESS
C
      D2J2=0.0D0
      DO 87 K1=1,NTENS
         D2J2=D2J2+S_DEV(K1)*S_DEV(K1)
 87   CONTINUE
      DO 88 K1=NDI+1,NTENS
         D2J2=D2J2+S_DEV(K1)*S_DEV(K1)
 88   CONTINUE
C      D2J2=S_DEV(1)*S_DEV(1)+S_DEV(2)*S_DEV(2)+
C     1     S_DEV(3)*S_DEV(3)+TWO*(S_DEV(4)*S_DEV(4)+
C     1     S_DEV(5)*S_DEV(5)+S_DEV(6)*S_DEV(6))
      SDEVNORM=SQRT(D2J2)
      Q=SQRT(3.0d0/2.0d0)*SDEVNORM
C
C    ADD TENSION CAP
C
      KAPPA=PROPS(6)
      RELLIP=PROPS(7)
      CHI=PROPS(8)
      DI1=THREE*STRESS_MEAN
      XPHI=KAPPA-RELLIP*(APHI-BPHI*KAPPA)
      IF (DI1.GT.KAPPA) THEN
       HEAVI=0.0D0
      ELSE
       HEAVI=ONE
      ENDIF
```

```
      FCAPPHI=ONE-HEAVI*((DI1-KAPPA)/(XPHI-KAPPA))**TWO
      IF (DABS(XPHI-KAPPA).GT.SMALL) THEN
       VAR1=XPHI-KAPPA
      ELSE
       VAR1=ONE
      ENDIF
      FCAPPHI=ONE-HEAVI*((DI1-KAPPA)/(XPHI-KAPPA))*
     1        ((DI1-KAPPA)/(XPHI-KAPPA))
      FCAPPHI=ONE-HEAVI*((DI1-KAPPA)/VAR1)*
     1        ((DI1-KAPPA)/VAR1)
      FUNCCAPPHI=(DABS(FCAPPHI)+FCAPPHI)/TWO
C
C     CALCULATE TRIAL YIELD FUNCTION
C
      FPHI=APHI-BPHI*STRESS_MEAN
      FCHI=APHI-BPHI*CHI
      FPHI2=FPHI*FPHI
      FCHI2=FCHI*FCHI
      VAR2=(DABS(FPHI2-FCHI2)+FPHI2-FCHI2)/TWO
      FTRIAL=SDEVNORM-(SQRT(FUNCCAPPHI)*SQRT(VAR2))
C
C     STORE VARIABLE IN STATE VARIABLE ARRAY
C
      STATEV(1)=FTRIAL
      STATEV(2)=Q
      STATEV(3)=STRESS_MEAN
C
      WRITE(*,*) 'FTRIAL = ',FTRIAL
C
      RETURN
      END
C
```